ABSTRACT

Title of Document: EXPERIMENTAL STUDY OF THE PARTITIONING OF Cu, Ag, Au, Mo, AND W AMONG PYRRHOTITE AND IMMISCIBLE Fe-S-O AND SILICATE MELTS

Michael J. Mengason, Master of Science, 2007

Directed By: Professor Philip A. Candela and Associate Research Scientist Philip M. Piccoli, Department of Geology

Partition coefficients have been determined for several transition metals amongst a rhyolitic silicate melt, pyrrhotite, and an immiscible Fe-S-O melt. Two sets of experiments were performed in sealed silica tubes at 1035°C-1045°C, FMQ-NNO fO_2, and $\log fS_2$ ~1 bar, and analyzed by EMPA and LA-ICP-MS. One set of experiments with Au, Ag, and Cu added yielded ($D_i^{a/b} \pm 1\sigma_{\overline{X}}$) $D_{Au}^{Fe-S-O/melt}$=300±100, $D_{Ag}^{Fe-S-O/melt}$=120±20, $D_{Cu}^{Fe-S-O/melt}$>200, and $D_{Au}^{po/melt}$=120±50, $D_{Ag}^{po/melt}$=58±8, $D_{Cu}^{po/melt}$>200. The other set of experiments with Mo and W added yielded $D_{Mo}^{Fe-S-O/melt}$=90±10, $D_W^{Fe-S-O/melt}$=9±3 and $D_{Mo}^{po/melt}$=35±3, $D_W^{po/melt}$=1.2±0.6x10^{-3}. Some preliminary data are also presented on the partitioning of Si, Ti, V, Co, Zn, Re, Th and U. Modeling predicts the loss to a daughter melt of up to 50% of the initial Au, >37% Cu, 24% Ag, 19% Mo, and 2% W when Fe-S-O melts are removed with other cumulate phases during fractionation. This would reduce the metal available to potential intrusion-related hydrothermal ore deposits.

EXPERIMENTAL STUDY OF THE PARTITIONING OF Cu, Ag, Au, Mo, AND W AMONG PYRRHOTITE AND IMMISCIBLE Fe-S-O AND SILICATE MELTS

By

Michael J. Mengason

Thesis submitted to the Faculty of the Graduate School of the
University of Maryland, College Park, in partial fulfillment
of the requirements for the degree of
Master of Science
2007

Advisory Committee:
Professor Philip A. Candela, Chair
Associate Research Scientist Philip M. Piccoli, Co-Chair
Assistant Professor Andrew Campbell, Committee Member

Dedication

To Suzanne Goucher, my wife,

and

to the memory of John B. Reid Jr., Hampshire College.

Acknowledgements

I would like to thank my committee members Phil Candela, Phil Piccoli, and Andrew Campbell for their help in reaching this point. I would like to thank Bill McDonough, Richard Ash, and Mario Luong for their assistance in planning and helping me perform the LA-ICP-MS analyses in this project. I would like to thank, again, Phil Piccoli for helping me with all of the EPMA work this project required. The other members of the LMDR group, Melissa Wilmot, Ryan Kerrigan, and Bryan Tattich, have all contributed conversations and support that made this much easier than it would have been. And lastly I'd like to thank all of the other graduate students who have made this a very good place to be.

This work was made possible by funding from the National Science Foundation. (EAR 0309967)

Table of Contents

List of Tables

List of Figures

1. Abstract

Partition coefficients have been determined for Au, Ag, Cu, W, and Mo amongst a rhyolitic silicate melt *(melt)*, pyrrhotite *(po)*, magnetite *(mt)*, and an immiscible Fe-S-O melt *(Fe-S-O)*. Two series of experiments were performed in sealed silica tubes at 1035°C-1045°C, fO_2 between the FMQ and NNO buffers, and log fS_2 ~1 bar for up to 2000 minutes. Run products were analyzed by EMPA and LA-ICP-MS. A series of experiments with Au, Ag, and Cu added to the system yielded ($D_i^{a/b} \pm 1\sigma_{\overline{X}}$ *standard deviation of the mean*) $D_{Au}^{Fe-S-O/melt}$=300±100, $D_{Ag}^{Fe-S-O/melt}$=120±20, $D_{Cu}^{Fe-S-O/melt}$>200, and $D_{Au}^{po/melt}$=120±50, $D_{Ag}^{po/melt}$=58±8, $D_{Cu}^{po/melt}$>200. A second series of experiments with Mo and W added yielded $D_{Mo}^{Fe-S-O/melt}$=90±10, $D_{W}^{Fe-S-O/melt}$=9±3 and $D_{Mo}^{po/melt}$=35±3, $D_{W}^{po/melt}$=1.2±0.6x10^{-3}. Analysis of both series for elements present in the starting materials yielded $D_{Zn}^{Fe-S-O/melt}$=10±1, $D_{Mn}^{Fe-S-O/melt}$ 1.9±0.3, $D_{V}^{Fe-S-O/melt}$ 3.1±0.9, $D_{Ti}^{Fe-S-O/melt}$ 0.28±0.05, $D_{Zn}^{po/melt}$=3.4±0.4, $D_{Mn}^{po/melt}$=1.1±0.1, $D_{Ti}^{po/melt}$=0.030±0.002, and preliminary data on the partitioning of Si, Co, Re, Th, and U. An additional preliminary experiment using sealed silica tubes at ~1kbar (100MPa) with a dacitic silicate melt and Au, Ag, and Cu added yielded similar results for these elements, suggesting pressure and silicate melt composition have a limited effect on these partition coefficients. Modeling suggests magnetite-series granitic magmas undergoing fractionation may have reductions in the total metal content of evolved melts produced by as much as 50% for Au, >37% Cu, 24% Ag, 19% Mo, and 2% W when Fe-S-O melts are removed with other cumulate phases. Modeling of granitic magmas that have assimilated

additional sulfide from sedimentary rock predicts they may undergo more severe depletion in metals. These metal depletions may help to explain the occurrence or absence of associated intrusion-related hydrothermal ore deposits and the relative abundances of metals within them.

2. Introduction

Arc magmas are probably derived from several distinct geochemcial reservoirs and represent a potential source for the economically valuable elements found in some hydrothermal deposits. In subduction zones, the subducting slab, mantle wedge, and overlying oceanic or continental crust are all potential sources of ore metals and associated volatile constituents. The complex and repeated partial melting and crystallization of magmas in these systems could allow for the mobilization and potential concentration of elements of economic interest.

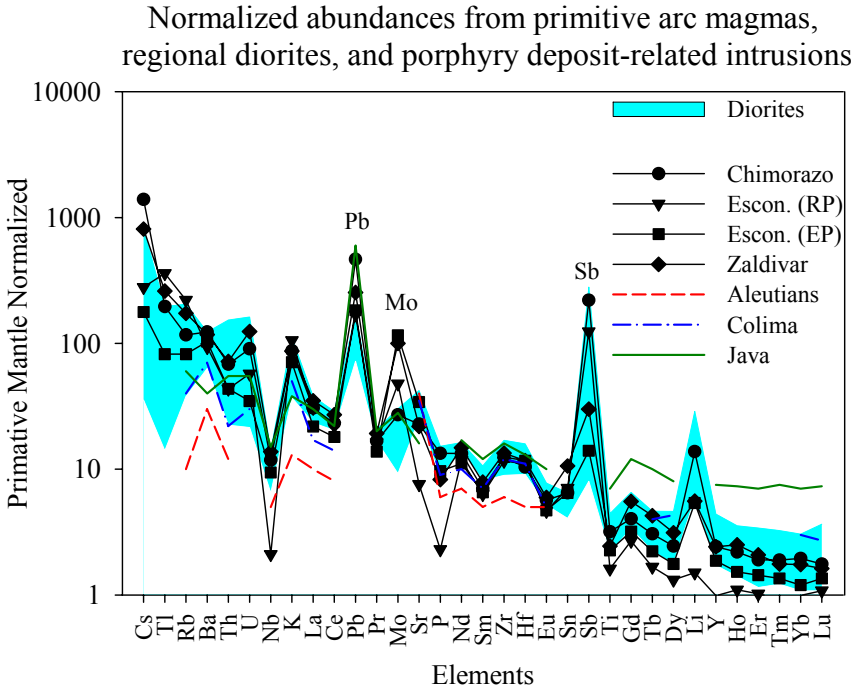

Figure 1 Porphyry ore deposits and regional abundance correlations

The usefulness of porphyry deposits as indicators of underlying geochemical trends in arc volcanic rocks can be seen in this diagram. (Figure after Richards 2003) The abundance of many elements less compatible in the mantle are higher in these porphyry-related intrusions compared to regional diorites, which are more enriched than more primitive arc volcanic rocks. Porphyry deposits can highlight elements which are being concentrated by processes in subduction zones. Data: DeBari and Sleep (1991), Luhr (1992), Richards et al. (2001), and Reubi et al. (2002); primitive mantle normalized values from Sun and McDonough (1989). EP=Escondida porphyry, RP = Rhyolitic porphyry.

Many chalcophile elements show enrichment in volcanic and igneous rocks produced at the volcanic front. Figure 1 (Richards, 2003) compares the concentrations of trace elements found in primitive arc magmas, a regional diorite from Chile, and the related intrusions associated Cu-(Mo and Au) porphyry deposits. All values are normalized to primitive mantle values in this spider diagram. A pattern of increasing enrichment in the elements to the left of Ti relative to primitive mantle can be seen in the selected arc magmas (colored lines), through the more evolved regional diorites (blue field), to each porphyry-related intrusions (symbols), with the rhyolite intrusion (RP) having generally the most extreme enrichment. The chalcophile elements Pb, Sb, and Mo all show notable enrichment. These deposits are an amplification of the geochemical anomaly inherent in the evolved arc magmas, which are in turn the result of crystallization and other phase separations. Investigation into processes operating during these separations may help predict the occurrence of specific beneficial anomalies or specific processes which are detrimental to their formation. In this study I examine the partitioning of Cu, Ag, Au, Mo and W, elements in varying abundance in hydrothermal ore deposits, during the separation of reduced sulfur-containing phases.

Hydrothermal ore deposits, whether porphyry-type or epithermal-vein deposits, may be formed by the transport of metals by a magmatic volatile phase(s) (MVP) to sites of ore deposition, concentrating metals to economically viable levels. These deposits are associated with shallow arc magmas which act as a source of metals. The amount of metal contained within the magma ultimately limits the potential of any derivative deposits. A portion of the metal resident in the magma

will be found in magmatic minerals. The ability of the MVP to transport metals has been studied experimentally (e.g. Candela and Holland 1984, 1986; Williams et al. 1995; Candela and Piccoli 1995; Frank et al. 2002; Simon et al. 2003). Holland (1972), Candela and Bouton (1990), and Lynton et al. (1993) have proposed that MVP is the first step in concentrating the metal from melt. This may be pre-empted, however, by the sequestering of important chalcophile elements in phases that are not accessible to the MVP. If this sequestering is taking place, it may be doing so at a shallow level near the ultimate plutonic consolidation, or it may take place earlier and deeper in the system.

Studies of igneous and volcanic rocks (e.g. Luhr et al. 1984, Rye et al. 1984, Metrich and Clocchiatti 1996, Hemming and Carmichael 1973, Stimac et al. 1996, Larocque et al. 1998, 2000) are consistent with sulfides being significant in these evolving magmas. Some of these sulfides are pyrrhotite ($Fe_{1-x}S$), intermediate sulfide solution (iss) (the high temperature form of $CuFeS_2$), and an iron sulfide-oxide melt (Fe-S-O) which is immiscible in the silicate melt. Evidence for the presence of sulfides and iron sulfide-oxide melts, in shallow-level magmas can be found in volcanic rocks. Select data for andesitic to rhyolitic systems are shown in figure 2.

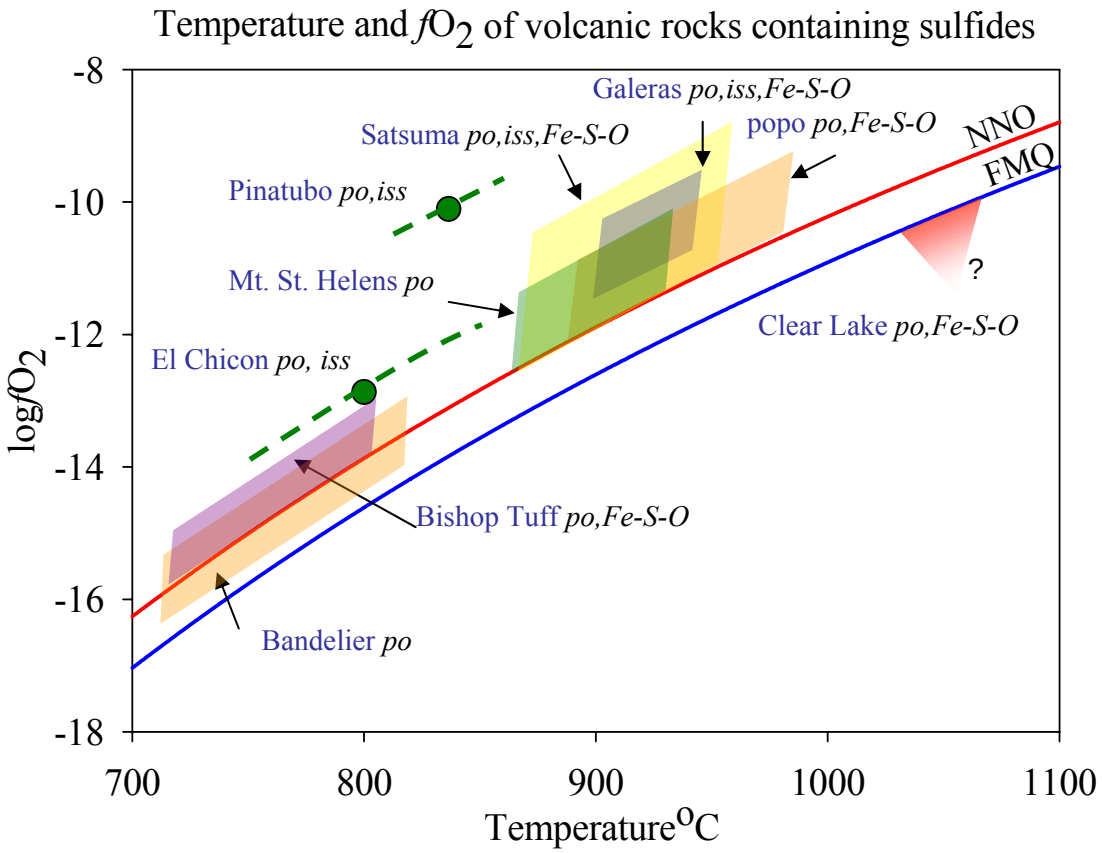

Figure 2 Sulfide-containing volcanic rock characteristics.

Plot of log fO_2 and eruption temperature for a variety of sulfide-bearing volcanic systems. The nickel-nickel oxide (NNO) and fayalite-magnetite-quartz buffers (FMQ) are plotted for comparison. Data from: Stimac et al. (1996), Larocque et al. (1998, 2000), Stimac and Hickmott (1994), Blundy et al. (2006), Ueda and Itaya (1981), Witter et al. (2005), Hildreth and Wilson (2007), Warshaw and Smith (1988), Luhr et al. (1984), Rutherford and Devine (1991), and Calvache and Williams (1997).

Eruption temperatures, mostly determined by magnetite-ilmenite geothermometry, range from ~700°C to over 1050°C. Fayalite-Magnetite-Quartz (FMQ) and Nickel-Nickel Oxide (NNO) oxygen fugacity buffer curves have been included in the figure to show the relatively high oxidation state of these systems. These systems are the natural models for the experiments profiled here.

Previous work on the partitioning of elements between sulfides and silicic melts indicate a strong preference for the sulfides. Nernst-type partition coefficients

are given in table 1 from Stimac and Hickmott (1994) working in rhyolites from Clear Lake, USA and Yang et al. (2006) in a study of po in granitoids from New Brunswick, Canada and a series of experimental studies: Lynton et al. (1993), partitioning between po and rhyolite glass at fO_2 (~NNO); Jugo et al. (1999), partitioning between po and a synthetic haplogranitic melt at 850°C and 100 MPa; Stuller (2001), po and a rhyolite glass at 850°C and 500bar (50MPa) at approximately the NNO fO_2 buffer; and Englander (2005), po and a rhyolite glass at 800°C and 140MPa, with fO_2 between the FMQ-NNO buffer.

Table 1 Partition coefficients ($D^{po/silicate\ melt}$) from previous studies

$D^{po/melt}$	Cu	Ag	Au	Mo	Co	Zn	Mn
Stimac and Hickmott (1994)	~499-502			161	~999		
Yang et al. (2006)			150±83				
Stuller (2001)					180±20	1.9±0.3	1.8±0.1
Lynton (1993)	500±200						
Jugo (1999)	2600±300		140±40				
Englander (2005)		~2000					

Limited data exist on the partitioning of trace elements with regard to the Fe-S-O phase. Analysis of quenched Fe-S-O melt blebs and host silicate glasses from volcanic rocks was performed by Stimac and Hickmott (1996). Partitioning between the blebs and quenched silicic melts of andesitic to rhyolitic composition for Cu, Zn and Mo was 23-67, 5-21, and 11, respectively. In an experimental study, Ripley et al. (2002) determined a partition coefficient for Cu between a liquid copper-iron sulfide containing oxygen and a basaltic melt. His results ranged from 755-1303 with fO_2 from FMQ-1 to FMQ-2.5 log units, decreasing with increasing fO_2. Partition coefficients between various compositions of (Fe,Cu,Ni)-S-O melts and various compositions of monosulfide solution (mss), of which pyrrhotite can be considered an iron and vacancy-rich end member, are shown in table 2. These studies, a

combination of experimental and natural systems, take place under conditions appropriate to a more mafic magma than the ones of interest here, but are included as the best available for comparison.

Table 2 Partition coefficients ($D^{(Fe,Cu,Ni)-S-O/mss}$) from previous studies

$D^{(Fe,Cu,Ni)-S-O/mss}$	Cu	Ag	Au	Co	Zn	Re
Fleet et al (1993)	3.7		11			
Li et al. (1996)	4-5					
Peregoedova et al. (2006)	3-5	2				
Ballhaus et al. (2001)	3.4-5.3					
Brenan et al. (2002)	3.6-3.8					0.4
Mungall et al. (2005)	5		100			
Barnes et al. (2006)		2.6		0.2-0.4	50	0.1-0.2

Despite the evidence from mafic systems that immiscible Fe-S-O melts may be more potent sequestering agents than crystalline sulfides, little study has been done on these melts in more evolved magmas. Because of this significant gap in our understanding of these systems, Fe-S-O melts in intermediate to felsic magmas are the particular focus of this study.

Samples of Fe-S-O blebs in volcanic rocks provide crucial evidence of their high temperature properties, since immiscible Fe-S-O melts only exist as a separate phase within magmas at high temperature. These melts may undergo extremely rapid cooling when magmas containing them are erupted causing them to be quenched to a solid form along with the silicic melt. This quenching can preserve the appearance and physical relationships that existed prior to eruption, as seen in figure 3 (Stimac and Hickmott 1996). These details could be altered or lost during phase changes associated with slow cooling and varying oxidation conditions of the magma.

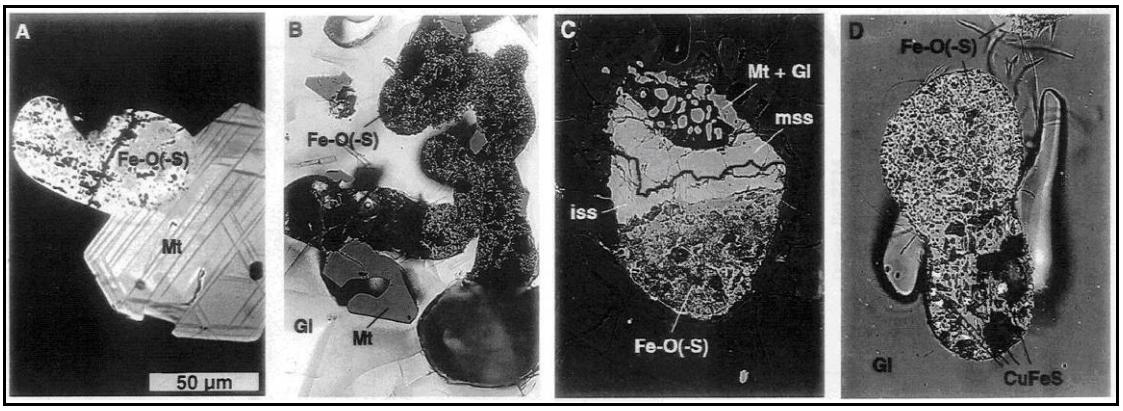

Figure 3 Fe-S-O melt blebs

From Stimac and Hickmott (1996). The authors used the following abbreviations: Mt – magnetite, Gl – glass, iss – intermediate solid solution, mss- mono-sulfide solution, and FeO(-S) – iron oxide also containing sulfide. 50µm scale applies to all four images. All four images show 'bleb' or 'globule' forms containing Fe, O, and S in unaltered glass from Satsuma Iwo-Jima rhyolite. The smooth outer boundary is indicative of a liquid-liquid interface. These globules are shown associated with magnetite in figure 3a-3c.

The boundaries between quenched blebs (referred to as globules in some texts) and quenched silicate melt (glass) in the images are smooth and curved. This is the boundary expected between two liquids prior to quench. These characteristics are apparent in the rapidly quenched samples of this study. Rapid quenching preserves the metal distribution at the equilibrium conditions of the run. To understand how these blebs would ultimately affect intrusive magmas during fractionation, it is also necessary to look at their behavior under those slow cooling conditions.

Slow cooling of an Fe-S-O melt in an intrusive system could result in isolated blebs behaving as minute fractionating sulfide magma chambers within crystalline sulfide and oxide cumulates separated from an enriched sulfide melt. A model for this fractionation can be drawn from work on massive sulfide deposits, such as that done at Sudbury by Naldrett and Kullerud (1969) and Li et al. (1992), where the

ability of sulfides to sequester Cu and related metals has been shown. Barnes et al. (2006), Prichard et al. (2004), Stavast et al (2006), and Imai (1994) apply this model of fractionation to explain the features of compositionally zoned sulfide melt blebs in dikes of basalt, basaltic andesite, latite, and quartz monzonite, respectively. In this model an initially homogenous immiscible sulfide melt of composition Fe-*i*-S-O, where *i* may be Ni, Cu, or other metal or combination of metals, will separate into one or more phases. The ultimate products of crystallization may include iron oxides such as magnetite, as well as iron and other sulfides, such as po, pyrite (py), chalcopyrite (cp), cubanite (cb), and pentalandite (pn). Prior to complete solidification, one or more liquid phases may still be present. For elements where $D^{\text{Fe-}i\text{-S-O/melt}}$ is greater than $D^{\text{sulfide-mineral/melt}}$ or $D^{\text{oxide/melt}}$, the sulfide liquid can become increasingly concentrated with respect to those elements. As changes in temperature and the fugacities of sulfur and oxygen occur, the system moves between the stability fields of these minerals causing deposition or dissolution of some phases. Late minerals crystallize at the interstices of existing minerals, within fractures in minerals, or as exsolution from minerals. These late phases may be small and are often difficult to detect, but may contain higher concentrations of metals than the silicate melt or the other sulfide and oxide phases present. Prichard et al. (2004) details the complex fractionation of Fe-*i*-S-O blebs into a cumulate structure bounded by mt and isolated by silicate minerals from the dike it is housed in. The final enriched sulfide fluid in this bleb yielded small fracture-filling argentopentalindite $(Fe_{5.37}Ni_{2.46}Ag_{0.97})_{8.8}S_8$ and silver telluride $(Ag_{1.95}Fe_{0.15})_{2.1}Te$. Ag was not detected in the other sulfides (po, pn, cp, cb, and py), and is not elevated in the surrounding

silicate melt. This illustrates two important features of immiscible sulfide melts. The first is that the total mass and average concentration of chalcophile metals within a sulfide bleb can be greater than the dominant assemblage of that bleb would predict. The second is that analysis of the major phases alone may underestimate the metal budget. Since analysis of the minor and trace phases individually may not be feasible, the ideal way to determine the affect of these blebs would be to sample the entire bleb without contamination from the surrounding silicate matrix. Since this is not possible, it raises the importance of experimental studies of Fe-*i*-S-O melts, where the rapidly quenched melt can be analyzed, and any exsolution occurs on a small enough scale that the sample volume is fully representative of the melt.

The magmas of intermediate to felsic composition this study deals with may originate as magmas of more primitive composition. Basalts and andesites may, through fractionation, evolve into dacites and rhyolites. Greene et al. (2006) document this evolution in a section of the Talkeetna Arc from a gabbronorite at the base, through mid-crustal dioritic and tonalitic rocks, to rhyolitic lavas and tuffs in the upper crust. During the rise of magma through the crust, there would be many opportunities for crystallization and enrichment of the silicate melt with respect to ore metals. Sulfides and other phases that are favorable hosts for ore metals would also become enriched. However, where iron oxides and sulfides are also crystallized and left behind; they would have the effect of sequestering these elements, and produce a depleted silicate melt. Evidence of these competing effects may be found in the metal content and element ratios in the final shallow magmas. A signature of this

may be present in hydrothermal ore deposits where they have scavenged such magmas.

Potential evidence for the link between sequestered Fe-S-O blebs and ore metal concentrations after crystallization can be seen in latite dikes associated with the Bingham and Tintic porphyry ore deposits. Stavast et al. (2006) have documented dikes rich in magmatic sulfides in the location of the intrusion responsible for these deposits. Transects taken across these horizontal dikes (sills) reveal chilled margins which are chemically distinct (figure 4A,B) from the center and contain a large number of Fe-S-O blebs of sizes ranging from 1-240μm.

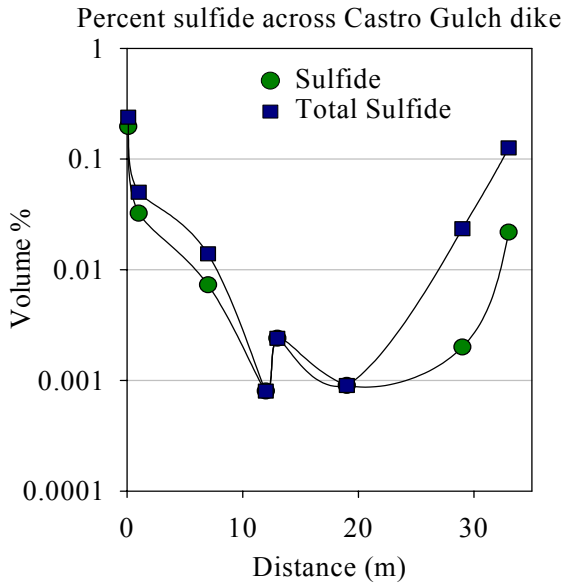

(A) Sulfide volume % across the Castro Gulch dike (after Stavast et al. 2006). Total sulfide includes partially degassed blebs containing a higher proportion of spongy FeO.

Concentrations across Castro Gulch dike

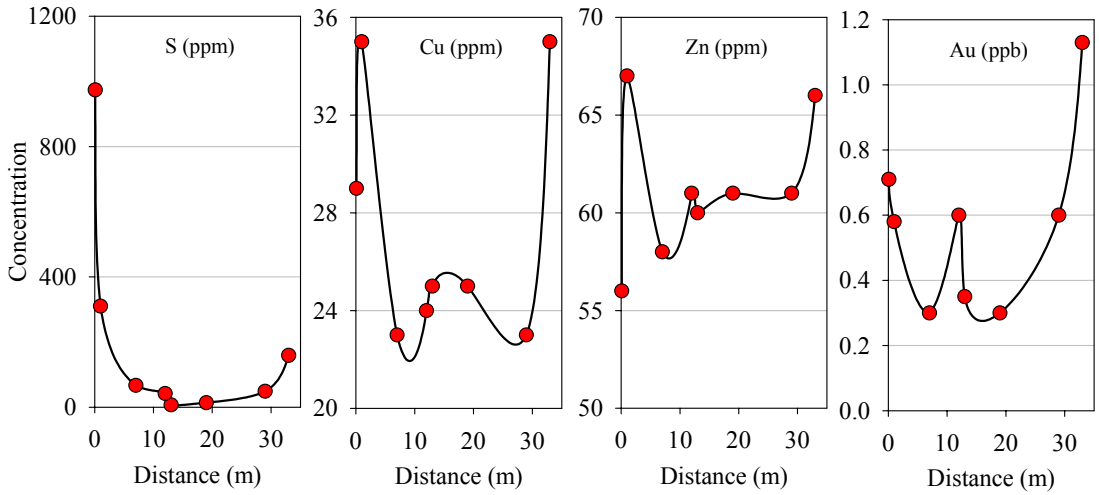

(B) Concentrations of S, Cu, Zn, and Au across the same transect showing a similar pattern (after Stavast et al. 2006).

Figure 4 Castro Gulch cross-section.

The transect in the Castro Gulch area contains 0.21 volume % sulfides in the margins, and only 0.0008 vol % sulfides in the center. The same samples have average SiO_2 < 59% in the margins, and >62% in the core. Some blebs showed evidence of partial degassing. These partially degassed Fe-S-O blebs with higher proportions of Fe and O containing spongy sections are also found in and near the margins and comprise 0.03 vol % of the rock. Those blebs which were in the core of the dike are assumed to have had the sulfur completely degassed, and during degassing to have released their load of ore metals back into the melt. If a greater fraction of the initial sulfide had been sequestered, due to a different cooling and crystallization history, there would have been less metal accessible to form a deposit.

In order to use Fe-S-O melts in an experimental system, it is necessary to understand the constituent phases and conditions of its formation. Phase relations in the Fe-S-O system have been determined experimentally by Vogel and Fülling

(1948), Hilty and Crafts (1952), Rosenqvist and Hynne (1953) and Naldrett (1969). A thermodynamic model the Fe-S-O system based on experimental data are presented in Kress (1997, 2000). The main phase fields in the polythermal projection shown in figure 5 (each field additionally containing melt and vapor) are po (solid solution), mt, wüstite (wu), and iron metal.

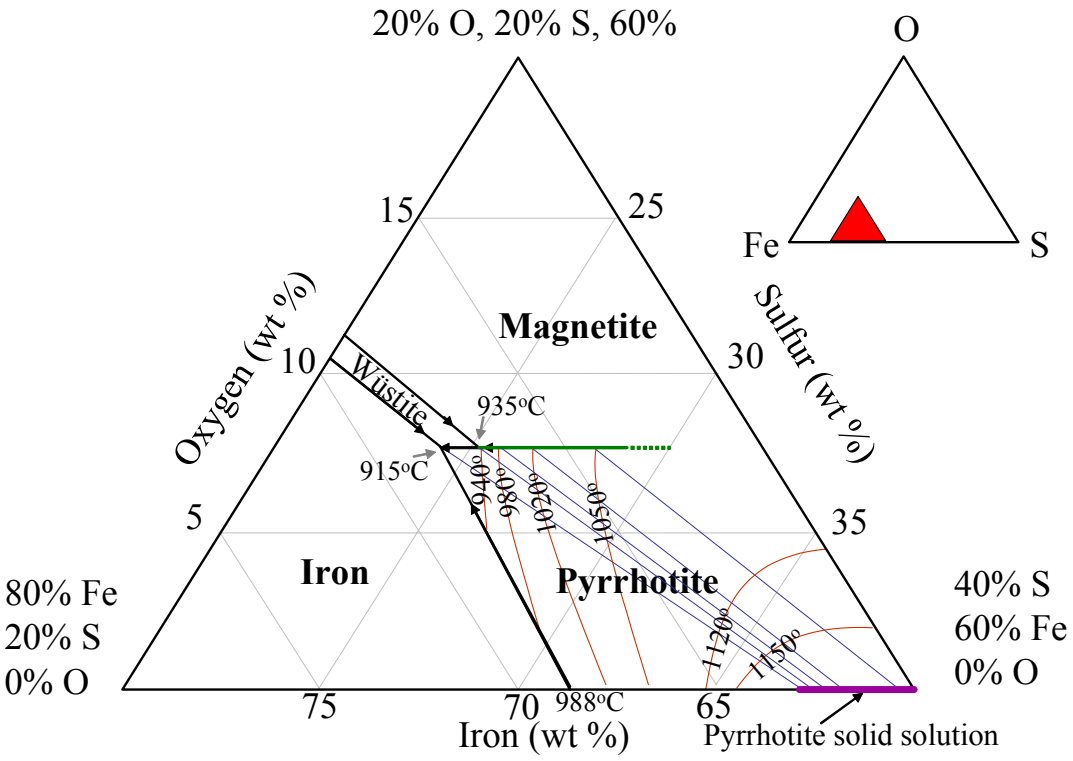

Figure 5 The system Fe-S-O.

Figure modified from Naldrett (1969). Diagram shows phase relations and isotherms *(red lines)* within a portion of the system Fe-S-O *(red triangle in guide)* at 1 bar. Cotectic melting occurs between mt and po solid solution *(green line)*. Experiments in this study were performed at 1036°C and 1042°C, with mt, po, Fe-S-O liquid, and vapor. Tie lines from po composition *(blue lines)* connect to cotectic melting temperature and liquid composition for a given po solid solution composition.

This study focuses on the mt and po cotectic, where these two minerals as well as an Fe-S-O melt and vapor phase are all stable. Wu and iron metal are not encountered at the oxygen and sulfur fugacities of these experiments. The minimum temperature at

which an Fe-S-O melt can form is dependent on the composition of the po. Elevated sulfur inhibits melting until a higher temperature in a sealed system where the vapor is in equilibrium with the po. Lower melting temperatures (e.g. the mt, po, Wüstite reaction point at 935°C) can only be achieved at lower sulfur and oxygen fugacities than the natural systems I am attempting to model, creating a lower temperature limit. An upper limit is imposed by the need to avoid exhausting one or the other mineral phases for the duration of the experiment. In practice, given a proportion of po:mt of 2.4:1 (approximating the bulk composition at the cotectic) and the specific compositions of the starting materials, the necessary temperature range is 1035-1045°C. The phase relationships within the more complex Fe-S-O-Si system have been determined by MacLean (1969) using pressed alumina crucibles sealed within evacuated quartz tubing. The components chosen by MacLean to represent this system are Fe_3O_4-FeO-FeS-SiO_2. My experiments are limited to the Fe_3O_4-FeS-SiO_2 ternary subsystem where mt, po, tridymite (td), silicate melt, immiscible Fe-S-O melt, and vapor coexist.

3. Experimental Methods

3.1 Equipment, Conditions, and Procedures

Experiments were performed using evacuated sealed silica tubes in horizontal tube-style furnaces followed by quenching in a water bath. Samples were run as groups of three replicates per experiment, in batches of up to six samples at one time. The silica tubes used were Haraeus HLQ-200 fused silica tubes with an interior diameter (ID) of 3mm, an outer diameter (OD) of 7mm, and approximate length of 30-40mm. Experimental charges were weighed using a Mettler Toledo AE240 balance before and after the run. The amount of material used is based on concerns for conservation of starting materials, restrictions imposed by the furnace used, and analytical requirements. Typical total charge masses were ~25mg. Temperature variations were kept to a minimum by selecting the portion of the furnace with the flattest temperature profile. All temperatures were determined using type-K thermocouples. The total temperature gradient in the furnace varied from 10°C/cm at the ends of the furnace to ~2°C/cm at the position 25cm from the front face of the furnace used for all experiments. Temperatures at points along the bottom, top, and sides at the sample position are within ~2°C of the central temperature. During the experiment, the thermocouple tip is located adjacent to the capsules. Based on their size, the charges occupied less than $1cm^3$ of the furnace, and would not have experienced a temperature gradient greater than 2°C when at the run temperature. Samples typically reached the desired run temperature in 10-15 minutes. After run times of 20, 200, or 2000 minutes at run temperature, samples were removed from the

furnace and quenched in a water bath. The elapsed time from furnace to water in most cases was estimated at 5-20 seconds. Pressure in the experiments is controlled by the internal assemblage. The maximum rated pressure of silica tubes of this aspect ratio can be used to estimate run pressures as less than approximately 40bar (4MPa). Estimates of the pressure based on the amount of water and sulfur in the starting materials, the internal volume of the capsule, and the temperature place the run pressure at approximately 1-10 bars (0.1-1MPa).

The experiments were conducted in two parallel series, one series of the group 11 elements Cu, Ag, and Au, and the other of the group 6 elements Mo, and W. Two series were performed in order to keep the total amount of additional metal entered into the system to a minimum as early experiments showed that inclusion of a few weight percent of the study elements in the Fe-S-O melt led to melting point depression, which would have proven experimentally difficult and made comparisons less meaningful, and the potential for multiple similar cations altering the activities involved also was to be avoided. Running and analyzing two series also allowed for the possibility of comparing the separate results for the same element, as was done for Mn. The three replicates were performed at three time intervals for each series, yielding a total of 18 experiments.

As a test of the applicability of partition coefficients determined here to higher pressure systems and to an alternate silicate melt, an experiment was designed and performed at pressures more appropriate to intrusive magmas. Although the effects of pressure and water on the formation and composition of the Fe-S-O melt are expected to be small (Naldrett 1969 and Naldrett and Richardson 1967), pressure may

affect the silicate phase and partitioning relative to it. An evacuated sealed silica tube was again employed, but one with an ID of 0.5mm and an OD of 5mm. Trials of this tube using only distilled water reached a calculated pressure of 1.2kbar (120MPa) based on ideal gas behavior. The restricted size of the ID required that dry sample components be added first, then a small portion of water was drawn into the tube under vacuum, and finally the tube was centrifuged to bring all of the components together at the base of the tube. Immediately following this, the sample was encased in crushed dry ice to freeze the liquid, then placed under vacuum and sealed. The sample was run for 200 minutes with all other aspects of the experiment the same as the other samples. This experiment was a scaled down replicate of the group 11 experiments.

3.2 Starting Materials

In an effort to make the results of this study as applicable as possible to natural systems, natural starting materials were used. The basic components of the Fe, S, O, and Si system are represented by mt, po and silicate glass. The mt is from Essex County, NY. The po, acquired from Wards Scientific, is from Dalnegorsk, Russia. A rhyolitic pumice (air fall) from the Bishop Tuff, CA was used in the two experimental series and a dacitic air fall from Mount Saint Helens, WA used in the high pressure experiment. The sample of Bishop Tuff used corresponds to field location B-72 in Hildreth (1977). While the composition of the Bishop Tuff rhyolite allows for nearly complete melting at the low pressure and water content of these experiments, the Mount Saint Helens sample would be a more complicated mixture of phases. This

lead to its use in only the high pressure and potential water content run where it was expected to result in a satisfactory melt (Blundy and Cashman 2001).

Prior to use in the experiments, the starting materials went through a series of preparation steps. Table 3 contains analyses performed on the starting materials as part of this study.

Table 3 Compositions of starting materials

	Bishop Tuff [#]	
Major Oxides (*wt. %* $1\sigma_{\bar{x}}$)		
SiO_2	75.4	*0.4*
Al_2O_3	12.18	*0.06*
FeO(t)	0.6	*0.1*
MnO	0.018	*0.002*
CaO	0.47	*0.02*
Na_2O	2.8	*0.1*
K_2O	5.5	*0.2*
TiO_2	0.105	*0.004*

	Bishop Tuff		**Pyrrhotite**		**Magnetite***	
Major and Trace Elements (*ppm* $1\sigma_{\bar{x}}$)						
S *(wt. %)*	0.003	*0.0003*	39.57	*0.01*		
Ti	630	*20*	4.43	*0.08*	2830	*40*
V	1.0	*0.2*	<0.2	-	93.7	*0.2*
Mn	140	*10*	10.8	*0.5*	810	*30*
Fe *(wt. %)*	0.5	*0.1*	59.59	*0.02*	71.5	*0.5*
Co	0.3	*0.1*	29.8	*0.1*	40	*1*
Cu	1.3	*0.6*	4	*2*	<1	-
Zn	20	*2*				
Mo	3.1	*0.1*	0.5	*0.2*	0.6	*0.1*
Ag	0.2	*0.1*	0.065	*0.008*	<0.07	-
W	1.27	*0.07*	<0.03	-	<0.04	-
Re	0.02	*0.01*	<0.017	-	<0.03	-
Au	0.09	*0.05*	<0.017	-	<0.03	-
Th	12.8	*0.5*				
U	3.2	*0.2*				

SiO_2, Al_2O_3, Na_2O, K_2O, S, and Fe determined by WDS. All others determined by LA-ICP-MS.
$\sigma_{\bar{x}}$ Standard deviation of the mean
* LA-ICP-MS calculated using Fe in stoichiometric mt (Fe=72wt %) as internal standard
[#] Sample corresponds to site B-72 described in Hildreth (1977)
< indicates below detection

Smaller minerals are more likely to equilibrate in the short timescales of laboratory experiments as the time required for equilibration increases with the distance of diffusion within the mineral. This factor favors the use of small grains. However, a portion of the mt and the po are consumed in the formation of the Fe-S-O melt, and

the final size of these grains must be large enough, ~10-30μm, to accommodate multiple analyses by EMPA and LA-ICP-MS. The mt and po were ground and sieved to 125-250μm as a compromise, with a small amount of powdered (<125μm) mt and po added to help quickly form the Fe-S-O melt. A magnet was used, following sieving of the mt and po, to remove unwanted contaminant phases. Visual and BSE inspection of these minerals did not reveal the presence of inclusions. The Bishop Tuff used in these experiments is from the Sherwin Grade air fall, and has been pulverized and powdered. The Mount Saint Helens ash was powdered and heated to 1250°C in a platinum sleeve within an evacuated sealed quartz tube and quenched to create a more uniform glass phase. Minor and trace elements of interest in this study enter the charges both as constituents of the basic starting materials and as components of additional phases. Additional phases (0.3-1.3mg per phase) used in this study include both pure metal and mineral grains (table 4).

Table 4 Additional metals, compounds, and minerals used in experiments.

Elements	*Phase*	*Origin*
Cu	Chalcopyrite *(cp)* $CuFeS_2$	Ellenville, NY
Ag	Ag_2S	Synthetic
Au	Gold foil 99.99%	Fisher Scientific
Zn	Sphalerite *(sp)* $(Zn, Fe^{2+})S$	Creede, CO
Mo	Molybdenite *(mb)* MoS_2	Pine Creek, CA
W	Wolframite *(wo)* $(Fe^{2+},Mn)WO_4$	Brazil

Mineral phases used in experiments. Ag_2S was synthesized for these experiments.

4. Analytical Methods

4.1 Sample Preparation

After quench, the capsules were inspected and prepared for analysis. The run products were removed from the silica tubes and mounted in epoxy in groups of 3 or 6 per mount, maintaining orientation from the furnace. If the charge could not be completely removed from the capsule without likely fragmentation, the smallest section of the capsule possible was included in the mount. The epoxy was held under vacuum and opened to atmospheric pressure twice to aid in penetration into the porous charges. Following curing, the run products were polished with 320 and 600 grit paper followed by diamond pastes to a minimum grit size of 1μm. This exposed an area of ~8-10mm^2 for analysis. Optical photomicrographs were taken of the samples for identification and as maps for analysis. Reflected light microscopy was used to identify opaque phases and to estimate the amount of Fe-S-O formation.

4.2 Electron Probe Microanalysis (EPMA)

Run products were analyzed using a JEOL JXA-8900 SuperProbe at the University of Maryland. Initial analysis consisted of documenting structures and phase relationships through the use of backscatter electron (BSE) imaging and energy dispersive spectrometry (EDS) to identify the phases present and create maps in composition mode highlighting areas of differing average atomic number. These maps were be used to identify suitable areas for wavelength dispersive spectrometry (WDS) and LA-ICP-MS. WDS was used for the quantification of major, minor, and

some trace elements in mt, po, Fe-S-O melt, and silicate glass. A table of standards used in these analyses is available in appendix A. Analytical conditions used in WDS analysis are detailed in table 5.

Table 5 WDS conditions used for each phase analyzed

	Fe-S-O, po	mt	Glass Major Elements	Glass Trace Elements
Voltage	20 kV	20 kV	15 kV	30 kV
Beam Current	250 nA	250 nA	10 nA	250 nA
Spot Size	15 μm	10 μm	20 μm	30 μm

All x-ray intensities corrected using a ZAF algorithm.

Some of the phases and elements studied required special precautions and procedures. Trace element analysis of glasses requires caution, as the high electron density needed to initiate sufficient x-ray flux during trace element analysis can damage the glass and cause diffusion of some of the elements being studied. Given the reduction of glass density over prolonged exposure to the beam, the analytical volume will increase (Goldstein 1992). To monitor and compensate for this effect, the glass analyses were performed as 18 ten-second iterations which were summed to produce the result. This allowed for collection of background levels throughout the beam exposure and avoided potential problems associated with changing backgrounds. Heavy elements (high Z) require the use of L lines instead of the more energetic K lines and often suffer from spectral interferences. In the case of Mo in high sulfur phases such as pyrrhotite and the Fe-S-O blebs, Mo Lα is too close to the S Kα peak to be discerned easily. For that reason, Mo Lβ was used for these phases. The intensity of the Lβ peak is approximately 48% that of the Lα peak, making it more

difficult to discriminate from the background at low concentrations. In phases without this overlap problem, such as magnetite and the silicate glass, Mo Lα is used to allow greater sensitivity. The oxygen content of the Fe-S-O melt was determined from the Fe and S content. EDS and in some cases WDS was used to confirm that oxygen was the only other major component of the melts. To test for a potential calculation error in trace element concentrations based on the 90 wt.% total of Fe and S, some samples were recalculated including oxygen as well. This was determined not to be a problem as the reported concentrations were not affected.

4.3 Laser Ablation Inductively Coupled Mass Spectrometry (LA-ICP-MS)

In order to determine low element concentrations, laser ablation inductively coupled plasma mass spectrometry (LA-ICP-MS) was performed at the University of Maryland plasma mass spectrometry laboratory. Information from the BSE images was used to determine sample locations, beam size, and whether spot or line analyses were used. Sample ablation was performed by using a NewWave solid state Nd:YAG laser (λ=213 nm), using He carrier gas. Each sample consisted of a 20-30 second background collection, followed by ablation for up to 100 seconds of which 10-40 seconds was used, and 120-150 seconds of subsequent flushing. Analysis of the ablated material was performed using an Element 2 single collector magnetic sector ICP-MS. Internal standards were provided by WDS analysis. Ablation of glass (quenched silicate melt) was performed as either stationary spot analyses, 55μm spot size at 8 hertz, or as line analyses with 25-30μm spot sizes at 5-7 hertz. NIST 610 or NIST 612 standards were used with ^{27}Al as the internal standard. Isotopes of

elements analyzed for in the glass include ^{27}Al, ^{49}Ti, ^{51}V, ^{55}Mn, ^{57}Fe, ^{59}Co, ^{63}Cu, ^{66}Zn, ^{95}Mo, ^{107}Ag, ^{182}W, ^{185}Re, ^{197}Au, ^{232}Th, and ^{238}U. Since po and the Fe-S-O blebs in the run products were generally less than 100μm in diameter, spot analyses with sizes of 30-40μm were used at 7 hertz. Line analyses were performed at 8μm and 5hz for some samples where the quenched Fe-S-O phase occurred as thin bands around other minerals. Analysis of the iron sulfide phases utilized two standards of differing matrix composition to minimize bias due to matrix effects. Po and the quenched Fe-S-O melt produced greater ejected material (present now as debris) than glass which had been similarly ablated, highlighting the difference in the physical response of differing materials to the ablation procedure. Analysis of these phases was performed using ^{57}Fe as the internal standard with a sample of nickel-iron meteorite (Hoba) for Co, Mo, and W, and using ^{55}Mn with NIST standard glasses 610 and 612 for Ti, V, Zn, Re, Th, and U. For each element a most appropriate standard was chosen. Comparisons of those elements which were available in multiple standards revealed that while the choice of standard did effect the concentration reported, this effect was small, and not likely to be a major factor in the final uncertainty or accuracy.

The inclusion of only short ablation periods was found to be important in the analysis of W in the sulfide phases. In scrutinizing the signals it was apparent that the length of ablation time could also vary the reported concentration. The length of ablation time increases the depth of the ablation pit. General principles of laser ablation favor the use of shallow ablation pits, to avoid complications related to the focus of the laser, the effect of the cloud of ablated material on the beam, the efficiency of the entrainment of ejected material in the carrier gas stream, and the

potential for this material to be deposited on the sides of the pit. Beyond ~20-30 seconds of beam time, the W signal (as measured in counts per second *cps*) decreased more rapidly that either Mn or Fe. If the signal of interest is decaying more rapidly than the internal standard, an incorrect concentration may result. Accepting the integrated signal from only the first ten to twenty seconds when the pit was shallow, estimated to be less than one half the pit width, limited this effect. A small number of samples were analyzed using a line pattern, and limiting this to a small number of passes had the same effect. These two methodologies, spot vs. line, yielded similar concentrations in experiments of the same duration.

LA-ICP-MS analysis of the quenched melt from experiments containing Au, Ag, and Cu required careful inspection of the ablation signal excluding regions of contamination due to other phases. Examples of several small particles imbedded in the run product glass are shown in figure 6.

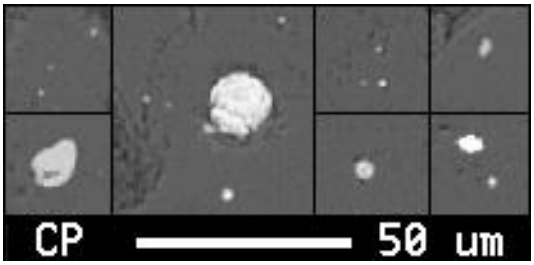

(A) Run # 20c

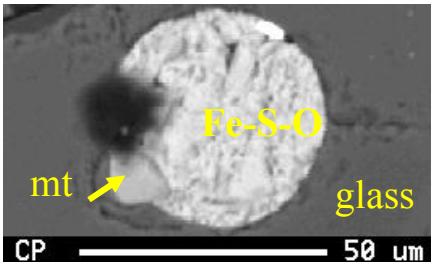

(B) Run # 20b

Figure 6 BSE images of run product glass.

(A) Small particles in the glass. Other phases present in the glass can include mt, po, Fe-S-O melt, electrum and Ag_2S. Close consideration of the LA-ICP-MS analyses was required to filter out signal spikes that are interpreted to be these extra phases. The scale bar is approximately the diameter of the spot analyzed. (B) Fe-S-O bleb (in glass) including mt and a small particle of Au or electrum. Although this bleb is larger than the signal spikes encountered, this may indicate that smaller blebs may have multiple phases present.

The size of particles shown ranges from sub-micron to ~20μm. Phases identified in the run product assemblage that may be present in the glass include mt and po grains, Fe-S-O blebs, Ag_2S, and electrum blebs. Electrum, as well as pure gold nuggets, may also be present as a quench product created during the short cooling interval between run temperature and the glass transition temperature. In addition, a spike in the signal may be produced by a composite of several phases (figure 6B).

Previous experiments on Au solubility and partitioning (Simon et al. 2005, 2007) revealed the presence of gold nuggets resident in the glass interpreted as quench products rather than separate phases present during the experiment. This possibility must be explored in my experiments. Exclusion of Au which was present in the glass at equilibrium, but which was subsequently exsolved, would cause underreporting of the Au concentration, and over-reporting of $D^{po/melt}$ and $D^{Fe\text{-}S\text{-}O/melt}$. Alternatively, inclusion of Au which was present during the run as a separate phase would result in over reporting the Au concentration in the glass.

Arguments in favor of inclusion revolve around the change in gold solubility between run temperature ~1035°C, and the glass transition temperature, which may be on the order of 500-600°C lower. During this cooling time the gold from a volume of glass may be scavenged by a growing nugget. The extent of gold that may be scavenged in the available time, approximately 10 seconds but possibly as long as 20 seconds, may be estimated. The characteristic length scale $(\mathcal{D}*t)^{0.5}$ of this system, where $\mathcal{D}$ is the diffusion coefficient and t is time, limits the radius and therefore volume of glass scavenged. Approximate diffusion coefficients for Na and Cs in a nearly dry granitic melt at this temperature can be estimated from Watson (1995) as

10^{-9} and 10^{-12} m^2/s, respectively. Using a value of 10^{-11} m^2/s for Au (a crude estimation), the volume of glass scavenged ($4 \times 10^3 - 1 \times 10^4$ μm^3) could account for the creation of a sphere of gold 0.2-0.25μm in diameter. This nugget would raise the Au concentration from the glass background of 1.5ppm to 2-2.5ppm in an ideal sampling event with a 55μm diameter beam lasting 30 seconds and ablating at a rate of 1μm/s. A cluster of such nuggets would have a greater effect. These brief spikes in the signal could be consistent with gold micro nuggets.

An argument against inclusion of Au and Au+Ag spikes is based on the high background of Fe in the glass, the appearance of very small nuggets in the signal, and the possibility that Au would be incorporated into Fe-S-O instead of nucleating as separate grains. It is possible that the increase of Fe due to a small bleb may be too small to discern in very small Fe-S-O blebs or po grains given its relatively high background (1-2 wt. %) in the glass, while the high concentration of Au (500-700ppm) in the bleb would markedly effect the concentration of the glass (1-2ppm). The inclusion of an electrum bead on or within the bleb would increase this effect. Based on the nugget described above, there would need to be several such nuggets in a small space to describe a sharp spike in the signal, while significantly raising the concentration. Finally, the presence of Au nuggets requires that the Au coming out of solution in the melt will favor nucleation, rather than enter into or onto one of the many other particle species. These cast doubt on the spikes being micro-nuggets.

The method used here for determining Au concentration involved the removal of the Fe containing spikes while retaining those spikes containing just Au or electrum. The presence of an elevated Fe signal (cps) in addition to a spike in Au or

Au+Ag was interpreted to represent the presence of either po or Fe-S-O melt in the glass. This portion of a sample's signal was not used to prevent reporting erroneously high concentrations in the glass, as in figure 7.

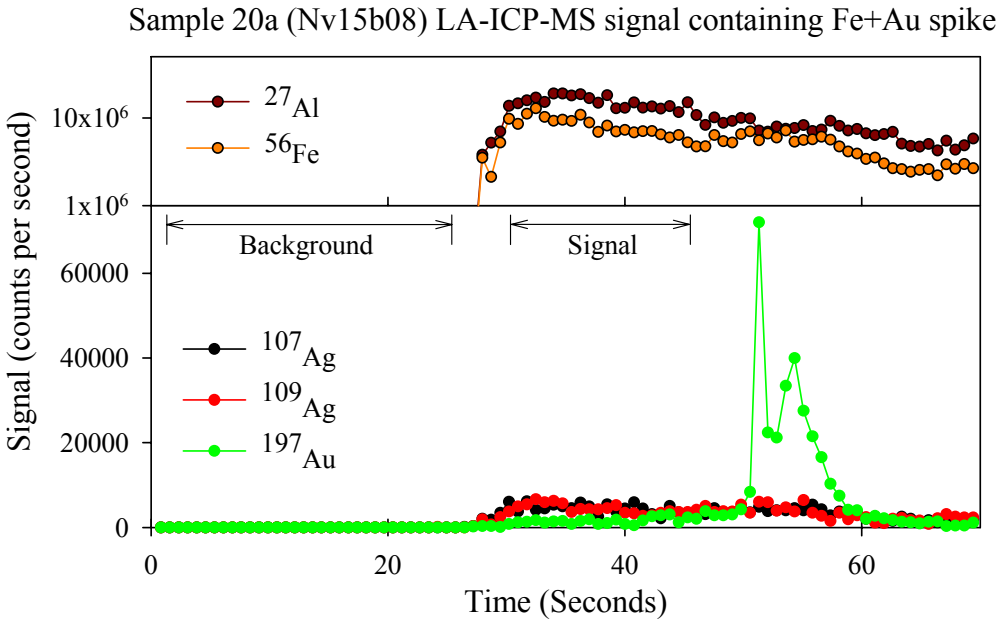

Figure 7 LA-ICP-MS signal showing an Fe+Au spike.

These spikes in this analysis of the quenched melt in run 20a were excluded due to the rise in Fe relative to Al, the internal standard, in the same time period as the Au spike. Fe signal length correlates to a Fe-S-O bleb of ~10µm.

The majority of spikes encountered were filtered out based on that criterion. Spikes of Ag that were not accompanied by either a rise in Au or Fe were not detected. Spikes where rises in Au, or Au and Ag were not accompanied by rises in Fe were considered individually, as in figure 8.

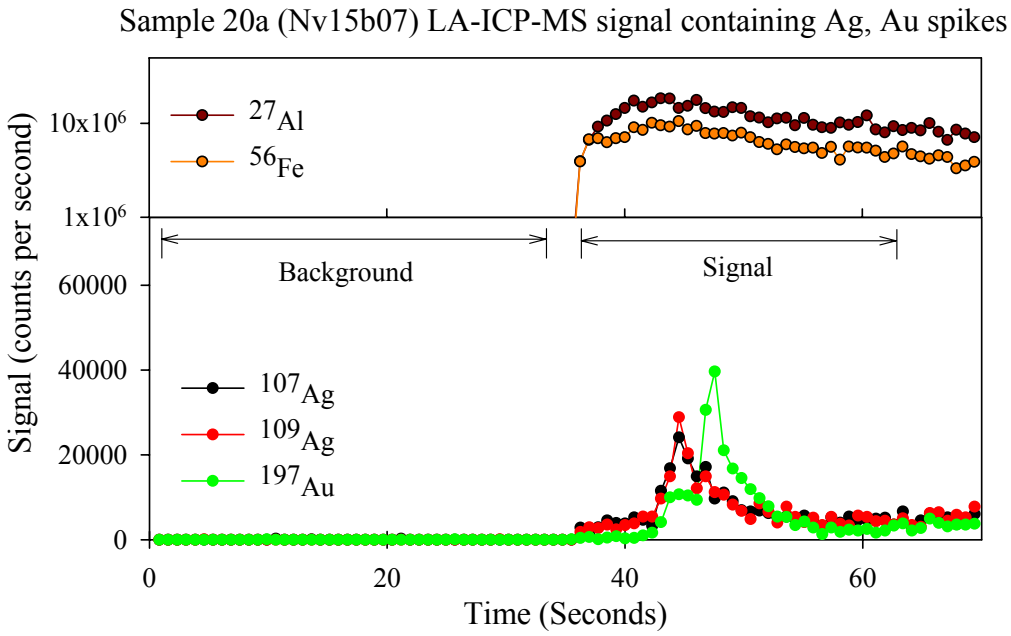

Figure 8 LA-ICP-MS signal showing Ag+Au and Au spikes without Fe.

These spikes in this analysis of the quenched melt in run 20a are not accompanied by an apparent change in Fe and were included in the signal as possible electrum and Au nuggets. The magnitude of these spikes is lower than in figure 8.

These spikes have been left in due to insufficient evidence that the spikes could be attributed to some other phenomenon than micro-nuggeting, which would have required their removal.

5. Results

The 4 types of experiments I have performed; 1) reconnaissance experiments with the starting assemblage *mt* + *po* and *mt* + *po* + *rhyolite*, 2) group 6 elements Mo and W, 3) group 11 elements Cu, Ag, and Au, and 4) high pressure group 11, have been completed and analyzed. Microstructural features as well as the major element chemistry of the Fe-S-O melt are consistent with the experimental and natural instances of Fe-S-O melts documented in literature. Nernst-type partition coefficients have been determined for some or all the sulfide and quenched melt relationships, and include the study elements Mo, W, Au, Ag, and Cu as well as Mn, Ti, V, Co, Re, Th, and U introduced within the natural starting materials. These additional elements allow for generalizations about partitioning in this system to be made on the basis of charge and ionic size.

5.1 Observations on Run Products

The experiments show the development of Fe-S-O melt coexisting with po, mt, and silicate melt, where the Fe-S-O melts exhibit fine grained quench textures, boundaries indicative of a liquid-liquid contact, and consistent spatial relationships with the po and mt. Figure 9 shows a run product that has been mounted in epoxy and polished.

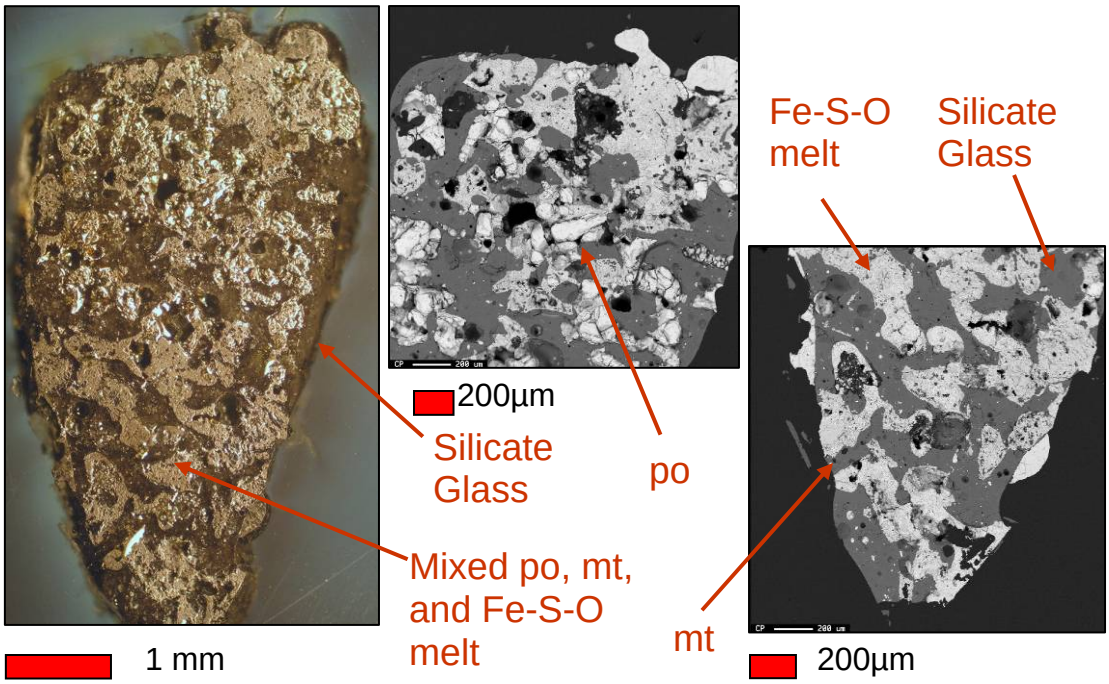

Figure 9 Images of a polished run product.

Reflected light and backscatter electron images of a polished run product (run 16d). Metallic and glass phases are easily identified in both images. Immiscible Fe-S-O melt and silicate melt are also easily discernable. Mt and po identification is difficult in reflected light and accomplished by using BSE imaging with the aid of EDS.

Phases are identified by reflected light microscopy, BSE images, and energy dispersive spectrometry (EDS). The tapered shape of the sample reflects the interior form of the quartz capsule, where the tip represents the down direction during the run. Patches of connected silicate melt and immiscible Fe-S-O melt can be clearly seen. Po and mt are found within or in contact with the Fe-S-O melt and are rarely seen on their own. Small blebs (1-100µm) of Fe-S-O melt are suspended in the silicate melt, and small blebs of silicate melt can be found suspended in the Fe-S-O melt. Figure 10 shows details of the mineral and melt relationships within a large connected patch of Fe-S-O melt. In this sample, the exsolution pattern is on the scale of <1–2µm.

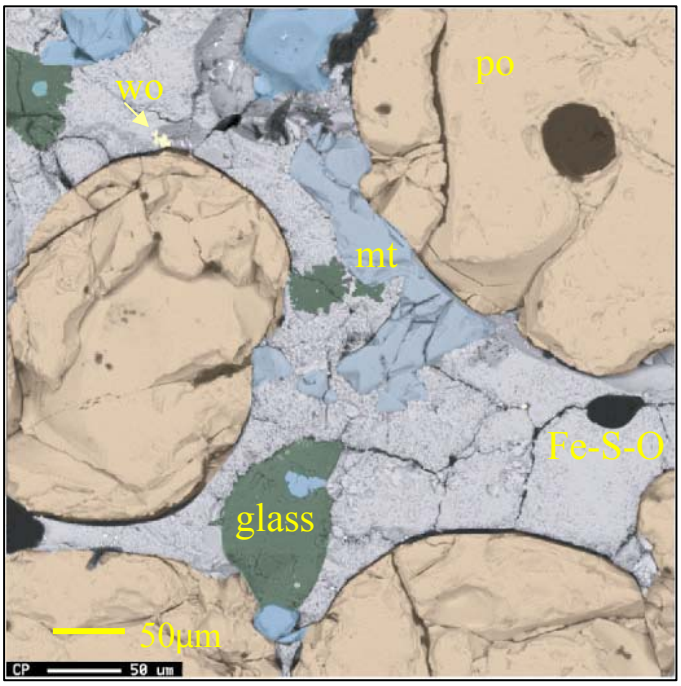

This false-color backscatter electron (BSE) image of a run product (18a) has colors added for clarity. This sample exhibited a well developed Fe-S-O melt with fine-grained quench textures (grey). The po grains (tan) are markedly rounded after 2000 min at ~1040°C, with the mt are reduced to small remnants (blue). Blebs of the silicate melt (green) are entrained in the Fe-S-O melt along with small, 1-5µm patches (yellow), patches of relict wolframite (wo).

Figure 10 BSE image showing po, mt, Fe-S-O melt and silicate melt

Growth of the Fe-S-O melt at the expense of the po and mt is clear in the rounded forms and reduced sizes of both. Liquid-liquid boundaries are evident between the two melt types. These features are comparable to what has been documented in natural samples. Figure 11 shows images from Stimac and Hickmott (1996) *left*, and this study, *right*. In figure 11A, mt, silicate glass, and quenched Fe-S-O melt are shown. In figure 11b, mt and po are shown with quenched Fe-O-S melt at the boundary.

(A)

(B)

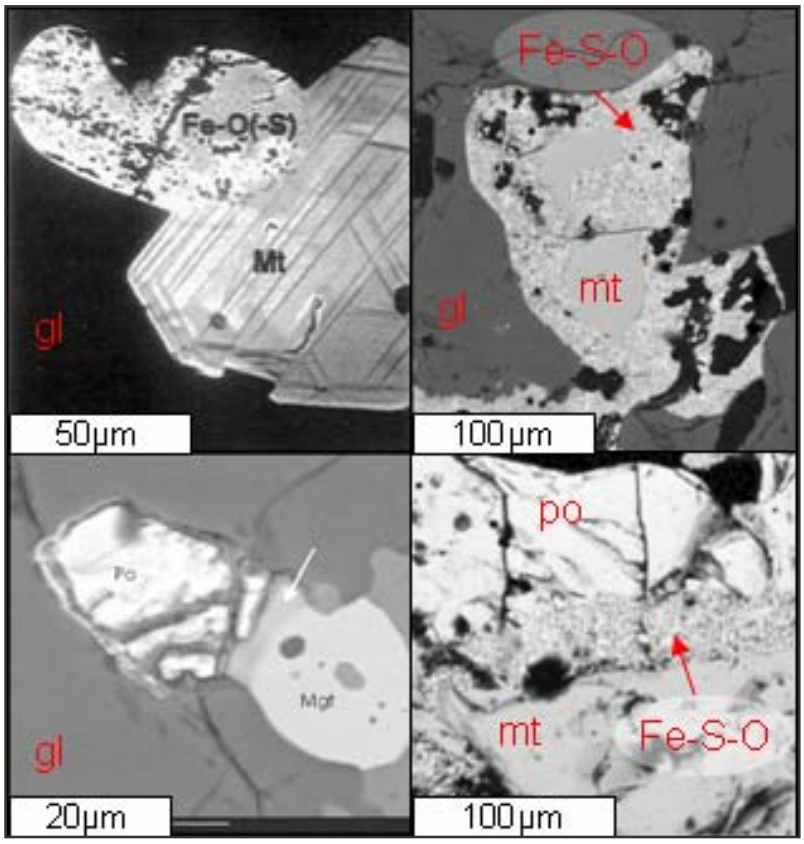

Figure 11 BSE images of Fe-S-O melts

Images from Stimac & Hickmott (1996) *left*, and this study, *right (top run 7c, bottom run 5)*. (A) (same as fig. 3a) shows an Fe-O(-S) (iron oxide also containing sulfur) globule attached to a mt in a rhyolite glass *(gl)*. (B) Shows po and mt with Fe-S-O liquid at the boundary.

As is evident from figures 9, 10 and 11, mt, po, and small blebs containing Au+Ag and Ag+S, prefer to be on the surface of or within the Fe-S-O melt relative to the silicate melt. Although small isolated grains have been found in the quenched melt, these are the exception. Conversely, where the proportions are reversed, a small amount of Fe-S-O melt will be found surrounding mt or po grains (figure 12). Since the Fe-S-O is derived from these grains, it is unclear where this is replacement and where this is due to attraction.

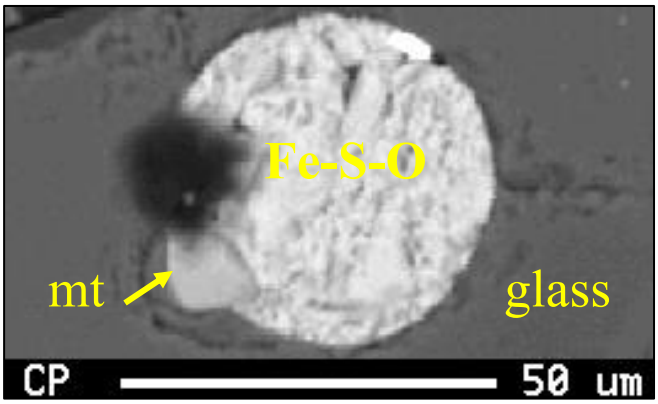

(A) A small quenched Fe-S-O bleb having a mt grain and a small Au+Ag bleb (white) at the surface. (run 20a)

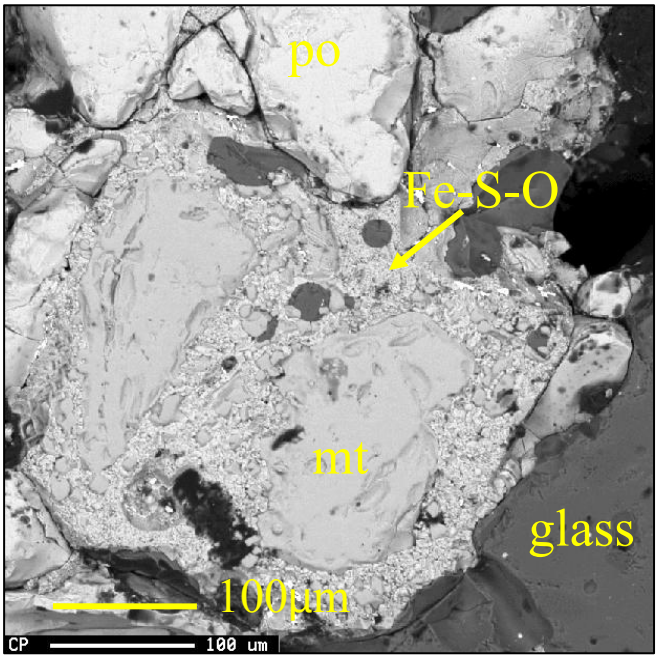

(B) Large mt grains surrounded by quenched Fe-S-O melt. (run 17a)

Figure 12 BSE images of Fe-S-O melt associations

Figure 12A (same as figure 6B) shows Au+Ag and mt and at the surface of a 25µm bleb of Fe-S-O. This behavior of tending to occur together, synneusis, is important in the study of these melts for two reasons. First, given the fact that Fe-S-O tends to reside on the surface of po and mt, it is likely to remain in place should these minerals become fixed to wall or within a crystal mush. As is evident from chilled dike margins, it is possible for Fe-S-O blebs to be caught in a cooling matrix and sequestered from the silicate melt. The second reason is the effect on the metal

budget of other phases, like Ag_2S, that may be carried along and sequestered with the Fe-S-O blebs increasing the amount of Ag removed from the melt. Although the presence of silicate mineral phases was avoided in these experiments, future study of how they physically interact with the Fe-S-O melt would help determine under what circumstances the melt can be sequestered.

5.2 Concentrations

Major, minor, and trace element chemistry has been determined on both series of experiments. Concentrations from the group 11 series, experiments in po and the quenched Fe-S-O melt are listed in table 6. Concentrations from the group 6 series experiments in po and the quenched Fe-S-O melt are listed in table 7. Analysis of the major element chemistry of all the glasses is presented in table 8. Data on more elements were collected from the group 6 runs than from the group 11 runs since the po & Fe-S-O melts were analyzed using LA-ICP-MS in addition to WDS. These additional elements are included in part to look for general trends in partition coefficients, and in part to provide some preliminary data and direction for future studies. Due to this second purpose, data are included that are below the detection limit, and are listed as less-than (<) a given value in ppm, which is the average detection limit for that sample.

Table 6 Concentrations from (Cu, Ag, Au) experiments

		20 Minutes						200 Minutes						2000 Minutes					
		22a	$1\sigma_{\bar{x}}$	**22b**	$1\sigma_{\bar{x}}$	**22c**	$1\sigma_{\bar{x}}$	**21a**	$1\sigma_{\bar{x}}$	**21b**	$1\sigma_{\bar{x}}$	**21c**	$1\sigma_{\bar{x}}$	**20a**	$1\sigma_{\bar{x}}$	**20b**	$1\sigma_{\bar{x}}$	**20c**	$1\sigma_{\bar{x}}$
Pyrrhotite																			
Si	ppm	<30	-	<30	-	<30	-	<30	-	<30	-	-	-	<30	-	<30	-	<30	-
S	%	36.8	*0.1*	38.1	*0.1*	37.9	*0.1*	38.0	*0.4*	37.5	*0.2*	37.8	*0.2*	37.8	*0.2*	37.6	*0.1*	37.7	*0.2*
Mn	ppm	93	*3*	25	*6*	94	*6*	57	*5*	80	*10*	121	*5*	60	*10*	70	*20*	140	*7*
Fe	%	62.6	*0.1*	61.5	*0.1*	61.0	*0.1*	61.4	*0.1*	61.5	*0.1*	61.1	*0.1*	61.2	*0.3*	61.1	*0.3*	60.7	*0.4*
Cu	ppm	480	*20*	990	*60*	1600	*100*	700	*50*	660	*40*	1000	*100*	700	*60*	430	*20*	1300	*60*
Ag	ppm	350	*30*	1500	*70*	1300	*100*	680	*80*	1000	*100*	890	*90*	600	*100*	700	*200*	700	*100*
Au	ppm	340	*40*	300	*100*	520	*60*	800	*100*	800	*100*	690	*60*	150	*40*	400	*100*	520	*30*
Fe-S-O																			
Si	ppm	2600	*700*	2400	*400*	2500	*300*	2500	*200*	2600	*200*	-	-	2230	*60*	2300	*200*	-	-
S	%	27	*2*	28	*1*	28.6	*0.5*	27.2	*0.4*	27.7	*0.3*	27	*1*	27.9	*0.3*	27.9	*0.6*	27.6	*0.2*
Mn	ppm	260	*30*	130	*30*	160	*20*	180	*20*	200	*30*	340	*50*	240	*20*	160	*10*	250	*10*
Fe	%	62.9	*0.3*	61.2	*0.3*	61.5	*0.2*	61.7	*0.3*	62.1	*0.3*	60.5	*0.8*	62.7	*0.1*	62.6	*0.2*	61.9	*0.1*
Cu	ppm	1300	*200*	1170	*40*	700	*80*	810	*50*	700	*100*	900	*30*	1350	*20*	600	*20*	940	*40*
Ag	ppm	5000	*3000*	1700	*100*	2000	*400*	1200	*100*	1300	*100*	4000	*2000*	1300	*200*	1100	*100*	1300	*100*
Au	ppm	3000	*2000*	400	*100*	300	*100*	650	*90*	900	*100*	7000	*4000*	700	*300*	600	*100*	770	*70*

% = Weight %, < indicates below detection

Table 7 Concentrations from (Mo, W) experiments

		20 Minutes						200 Minutes								2000 Minutes			
		17a	$1\sigma_{\bar{x}}$	**17b**	$1\sigma_{\bar{x}}$	**17c**	$1\sigma_{\bar{x}}$	**16d**	$1\sigma_{\bar{x}}$	**16e**	$1\sigma_{\bar{x}}$	**16f**	$1\sigma_{\bar{x}}$	**18a**	$1\sigma_{\bar{x}}$	**18b**	$1\sigma_{\bar{x}}$	**18c**	$1\sigma_{\bar{x}}$
Pyrrhotite																			
Si	ppm	<35	-	<35	-	-	-	<35	-	<35	-	-	-	<35	-	<35	-	-	-
S	%	38.5	*0.1*	38.7	*0.1*	38.2	*0.1*	38.0	*0.2*	38.0	*0.4*	37.2	*0.3*	37.9	*0.1*	38.2	*0.2*	37.3	*0.1*
Ti	ppm	7	*2*	7	*1*	10	*1*	8	*1*	13	*2*	22	*3*	14	*2*	16	*1*	20	*1*
V	ppm	<0.5	-	<1	-	<1	-	<1	-	<0.5	-	<0.4	-	<0.3	-	<0.5	-	<1	-
Mn	ppm	370	*20*	340	*2*	500	*30*	307	*9*	340	*10*	520	*40*	303	*7*	396	*6*	472	*8*
Fe	%	60.9	*0.1*	60.6	*0.1*	62.0	*0.1*	60.7	*0.1*	60.2	*0.1*	60.8	*0.3*	61.2	*0.1*	60.7	*0.1*	62.0	*0.1*
Co	ppm	37	*2*	60	*10*	37	*1*	33	*1*	50	*1*	37	*3*	109	*2*	49	*1*	37	*1*
Zn	ppm	36	*1*	18	*1*	33	*2*	38	*2*	33	*4*	48	*2*	19.2	*0.2*	26	*1*	39.1	*0.3*
Mo	ppm	800	*200*	200	*90*	500	*200*	1470	*40*	1200	*100*	1800	*200*	1140	*20*	1400	*30*	1470	*40*
W	ppm	0.16	*0.03*	0.4	*0.3*	0.09	*0.04*	4	*2*	10	*7*	0.28	*0.06*	0.18	*0.06*	0.3	*0.1*	0.14	*0.05*
Re	ppm	-	-	-	-	-	-	0.3	*0.1*	0.11	*0.01*	0.23	*0.01*	0.34	*0.02*	0.18	*0.02*	0.32	*0.01*
Th	ppm	-	-	-	-	-	-	<0.1	-	<0.07	-	<0.08	-	<0.04	-	<0.04	-	<0.06	-
U	ppm	-	-	-	-	-	-	<0.03	-	<0.03	-	<0.01	-	<0.01	-	<0.02	-	<0.02	-
Fe-S-O																			
Si	ppm	3100	*300*	2700	*200*	-	-	2800	*300*	3000	*1000*	-	-	3000	*100*	2800	*200*	-	-
S	%	27.0	*0.6*	27.0	*0.6*	34	*2*	25.8	*0.7*	26.9	*0.7*	25	*1*	26.7	*0.3*	27.1	*0.3*	25.0	*0.4*
Ti	ppm	600	*200*	450	*50*	1500	*200*	500	*400*	1400	*700*	2300	*900*	150	*40*	100	*20*	180	*60*
V	ppm	27	*7*	17.4	*0.2*	60	*9*	11	*9*	30	*10*	50	*20*	3.5	*0.9*	2.6	*0.6*	4.0	*0.4*
Mn	ppm	740	*40*	860	*20*	740	*90*	660	*50*	840	*80*	1160	*80*	600	*30*	770	*20*	1400	*300*
Fe	%	60.8	*0.1*	60.4	*0.1*	57	*1*	62.0	*0.2*	61.3	*0.2*	59.5	*0.3*	62.2	*0.2*	62.2	*0.1*	62.0	*0.5*
Co	ppm	21	*1*	27	*4*	18	*3*	16	*1*	16	*1*	13	*3*	55	*7*	30	*5*	17	*2*
Zn	ppm	41	*3*	33	*6*	60	*2*	100	*7*	100	*10*	130	*10*	47	*4*	60	*6*	165	*9*
Mo	ppm	5500	*600*	4900	*900*	3800	*500*	3600	*300*	2140	*60*	4700	*300*	3400	*200*	3400	*600*	4000	*300*
W	ppm	1900	*700*	2000	*1000*	2100	*700*	1800	*700*	1000	*300*	4000	*1000*	1400	*200*	2700	*900*	1500	*700*
Re	ppm	-	-	-	-	-	-	<0.2	-	<0.2	-	<0.3	-	<0.2	-	<0.3	-	<0.5	-
Th	ppm	-	-	-	-	-	-	0.4	*0.2*	1.5	*0.8*	1.7	*0.7*	0.17	*0.05*	0.7	*0.3*	0.9	*0.8*
U	ppm	-	-	-	-	-	-	0.15	*0.5*	0.9	*0.7*	0.6	*0.2*	0.07	*0.03*	0.16	*0.08*	0.2	*0.1*

% = Weight %, < indicates below detection

Table 8 Major oxides and trace elements from glasses

		20 Minutes						200 Minutes								2000 Minutes			
(Cu,Ag,Au)		**22a**	$1\sigma_{\bar{x}}$	**22b**	$1\sigma_{\bar{x}}$	**22c**	$1\sigma_{\bar{x}}$	**21a**	$1\sigma_{\bar{x}}$	**21b**	$1\sigma_{\bar{x}}$	**21c**	$1\sigma_{\bar{x}}$	**20a**	$1\sigma_{\bar{x}}$	**20b**	$1\sigma_{\bar{x}}$	**20c**	$1\sigma_{\bar{x}}$
SiO_2	%	76	*1*	74.7	*0.4*	74.7	*0.4*	73.6	*0.5*	74.4	*0.5*	76.4	*0.3*	73.7	*0.4*	73.2	*0.3*	75.3	*0.2*
Al_2O_3	%	12.5	*0.1*	12.2	*0.1*	12.4	*0.1*	12.4	*0.2*	12.4	*0.2*	12.58	*0.05*	12.8	*0.2*	12.6	*0.2*	12.5	*0.1*
FeO(t)	%	2.2	*0.7*	1.7	*0.4*	1.8	*0.2*	2.3	*0.3*	2.4	*0.2*	2.1	*0.4*	3.1	*0.1*	3.3	*0.2*	2.9	*0.2*
MnO	%	0.021	*0.004*	0.03	*0.01*	0.02	*0.01*	0.02	*0.01*	0.02	*0.01*	0.009	*0.003*	0.02	*0.01*	0.007	*0.004*	0.011	*0.003*
CaO	%	0.37	*0.03*	0.42	*0.02*	0.50	*0.07*	0.45	*0.02*	0.44	*0.03*	0.36	*0.01*	0.53	*0.03*	0.72	*0.02*	0.44	*0.02*
Na_2O	%	2.40	*0.04*	2.27	*0.04*	2.29	*0.04*	2.31	*0.04*	2.33	*0.04*	2.46	*0.02*	1.7	*0.2*	2.06	*0.03*	2.40	*0.03*
K_2O	%	6.0	*0.1*	5.93	*0.05*	5.86	*0.07*	6.13	*0.06*	6.11	*0.03*	6.13	*0.05*	5.90	*0.05*	5.77	*0.06*	6.00	*0.06*
SO_3	%	0.3	*0.2*	0.2	*0.1*	0.12	*0.05*	0.2	*0.1*	0.2	*0.1*	0.3	*0.2*	0.05	*0.01*	0.2	*0.1*	0.039	*0.009*
ASI	*	1.1		1.1		1.1		1.3		1.2		1.1		1.3		1.2		1.1	
Cu	ppm	18	*7*	<5	-	20	*10*	10	*10*	<5	-	6	*1*	<6	-	<3	-	2.6	*0.5*
Ag	ppm	13	*2*	22	*1*	28	*9*	16	*3*	10.8	*0.4*	19	*2*	10.1	*0.7*	14	*4*	17	*2*
Au	ppm	<0.2	-	<0.2	-	0.4	*0.1*	1.3	*0.4*	1.3	*0.5*	1.3	*0.4*	2.2	*0.3*	6	*3*	2.3	*0.6*
(Mo,W)		**17a**	$1\sigma_{\bar{x}}$	**17b**	$1\sigma_{\bar{x}}$	**17c**	$1\sigma_{\bar{x}}$	**16d**	$1\sigma_{\bar{x}}$	**16e**	$1\sigma_{\bar{x}}$	**16f**	$1\sigma_{\bar{x}}$	**18a**	$1\sigma_{\bar{x}}$	**18b**	$1\sigma_{\bar{x}}$	**18c**	$1\sigma_{\bar{x}}$
SiO_2	%	76.1	*0.3*	75.1	*0.6*	76.6	*0.3*	75.0	*0.2*	75.0	*0.3*	75.6	*0.2*	74.0	*0.2*	74.2	*0.3*	75.2	*0.7*
Al_2O_3	%	12.66	*0.05*	12.8	*0.2*	13.0	*0.2*	12.58	*0.07*	12.65	*0.09*	12.5	*0.1*	12.57	*0.08*	12.75	*0.09*	12.6	*0.3*
FeO(t)	%	0.9	*0.2*	1.8	*0.8*	1.1	*0.1*	2.2	*0.2*	2.1	*0.2*	1.7	*0.1*	3.3	*0.1*	2.3	*0.4*	2.7	*0.4*
MnO	%	0.04	*0.01*	0.04	*0.01*	0.02	*0.01*	0.06	*0.01*	0.05	*0.02*	0.05	*0.01*	0.04	*0.01*	0.04	*0.01*	0.04	*0.01*
CaO	%	0.40	*0.02*	0.47	*0.03*	0.44	*0.04*	0.46	*0.02*	0.41	*0.02*	0.38	*0.02*	0.51	*0.01*	0.50	*0.04*	0.47	*0.05*
Na_2O	%	2.26	*0.02*	2.25	*0.02*	2.47	*0.03*	2.1	*0.1*	2.26	*0.02*	2.29	*0.03*	2.12	*0.03*	2.28	*0.05*	2.41	*0.05*
K_2O	%	5.82	*0.04*	5.8	*0.1*	5.86	*0.07*	6.01	*0.05*	6.05	*0.04*	6.01	*0.04*	5.79	*0.03*	6.02	*0.05*	6.08	*0.09*
SO_3	%	0.03	*0.01*	0.6	*0.5*	0.09	*0.05*	0.16	*0.07*	0.10	*0.04*	0.03	*0.01*	0.16	*0.08*	0.06	*0.01*	0.12	*0.07*
ASI	*	1.2		1.2		1.2		1.2		1.2		1.1		1.2		1.1		1.1	
Ti	ppm	600	*100*	530	*40*	300	*100*	530	*20*	520	*40*	460	*20*	450	*30*	540	*20*	590	*30*
V	ppm	1.4	*0.4*	0.8	*0.1*	<2	-	1.3	*0.3*	0.9	*0.1*	2.3	*0.5*	0.71	*0.02*	1.2	*0.2*	1.9	*0.3*
Co	ppm	<1	-	<1	-	<0.8	-	<0.9	-	<0.8	-	0.5	*0.1*	<1	-	<2	-	0.5	*0.1*
Zn	ppm	18	*6*	14	*2*	7	*5*	7.6	*0.5*	6	*1*	25	*5*	<14	-	11	*1*	18	*2*
Mo	ppm	29	*2*	30	*2*	39	*6*	46	*7*	39	*5*	39	*2*	40	*3*	31	*8*	49	*7*
W	ppm	220	*60*	160	*20*	500	*100*	280	*20*	350	*40*	289	*30*	237	*30*	140	*50*	350	*30*
Re	ppm	<0.10	-	<0.08	-	-	-	<0.08	-	<0.04	-	-	-	<0.04	-	<0.05	-	-	-
Th	ppm	12	*2*	13	*0.8*	-	-	14	*1*	13.7	*0.6*	-	-	15	*2*	13.5	*0.6*	-	-
U	ppm	2.2	*0.3*	2.5	*0.2*	-	-	2.6	*0.4*	2.6	*0.2*	-	-	2.4	*0.4*	2.7	*0.1*	-	-

% = Weight %, FeO(t) = Total Fe as FeO, * = $Al_2O_3/(Na_2O+ K_2O+CaO)$ Molar, < indicates below detection

5.3 Partition Coefficients

The concentrations of 14 elements determined from analysis of the run products in this study have yielded Nernst-type partition coefficients for $D^{Fe\text{-}S\text{-}O/melt}$, $D^{po/melt}$, and $D^{Fe\text{-}S\text{-}O/po}$ ranging from 0.0012 to 9000. $D^{sulfide/melt}$ from the group 11 series experiments are listed in table 9. $D^{sulfide/melt}$ for the group 6 experiments are listed in table 10. $D^{Fe\text{-}S\text{-}O/po}$ for both series are listed in table 11. Several partition coefficients involve one concentration that was below the detection limit and are presented as < or > the value listed. These are included as a general indication of the behavior of these elements in the system, and give at least an indication of whether the element is compatible or incompatible between the phases described. This information is also important for future experimental work on these elements, as it is a starting point in the difficult task of finding a balance of concentrations where an element is abundant enough to be detectable in the less favored phase, while at the same time not in such a high concentration as to move out of the Henry's law region, where the activity coefficient is constant, in the more favored phase. Only those experiments that are near or at equilibrium can be averaged together to reach the final D.

Table 9 $D^{sulfide/melt}$ from (Cu,Ag,Au) experiments

	20 Minutes						200 Minutes						2000 Minutes					
$D^{po/melt}$	**22a**	$1\sigma_{\bar{x}}$	**22b**	$1\sigma_{\bar{x}}$	**22c**	$1\sigma_{\bar{x}}$	**21a**	$1\sigma_{\bar{x}}$	**21b**	$1\sigma_{\bar{x}}$	**21c**	$1\sigma_{\bar{x}}$	**20a**	$1\sigma_{\bar{x}}$	**20b**	$1\sigma_{\bar{x}}$	**20c**	$1\sigma_{\bar{x}}$
Mn	0.69	*0.07*	0.27	*0.07*	0.9	*0.1*	0.6	*0.1*	1.3	*0.1*	1.4	*0.3*	1.0	*0.2*	1.3	*0.3*	1.9	*0.1*
Cu	30	*10*	>200	-	100	*60*	50	*40*	>130	-	160	*40*	>120	-	>130	-	500	*100*
Ag	28	*5*	68	*5*	50	*20*	40	*10*	100	*10*	47	*7*	60	*10*	50	*20*	40	*10*
Au	2000	*1000*	1400	*700*	1300	*500*	600	*200*	700	*300*	500	*100*	70	*20*	>70	-	220	*60*
$D^{Fe-S-O/melt}$																		
Mn	1.9	*0.3*	1.4	*0.3*	1.5	*0.2*	2.0	*0.4*	3.4	*0.6*	4.1	*0.9*	4.2	*0.4*	2.8	*0.3*	3.5	*0.2*
Cu	70	*30*	>250	-	40	*30*	60	*40*	>140	-	130	*30*	>240	-	>170	-	370	*80*
Ag	400	*200*	77	*7*	70	*30*	80	*20*	120	*10*	200	*100*	130	*20*	80	*30*	80	*10*
Au	$2x10^4$	*$1x10^4$*	1700	*800*	700	*300*	500	*200*	700	*300*	5000	*4000*	300	*100*	>100	-	300	*90*

> indicates that the value is known in the sulfide phase, but is below detection in glass.

Table 10 $D^{sulfide/melt}$ from (Mo,W) experiments

		20 Minutes						200 Minutes						2000 Minutes					
		17a	$1\sigma_{\bar{x}}$	**17b**	$1\sigma_{\bar{x}}$	**17c**	$1\sigma_{\bar{x}}$	**16d**	$1\sigma_{\bar{x}}$	**16e**	$1\sigma_{\bar{x}}$	**16f**	$1\sigma_{\bar{x}}$	**18a**	$1\sigma_{\bar{x}}$	**18b**	$1\sigma_{\bar{x}}$	**18c**	$1\sigma_{\bar{x}}$
$D^{po/melt}$																			
Ti		0.011	*0.005*	0.013	*0.002*	0.03	*0.01*	0.02	*0.01*	0.02	*0.01*	0.05	*0.02*	0.032	*0.008*	0.030	*0.006*	0.03	*0.01*
V		<0.4	-	<0.7	-	-	-	<0.5	-	<0.5	-	<0.2	-	<0.5	-	<0.4	-	<0.3	-
Mn		1.2	*0.2*	1.2	*0.2*	3	*1*	0.7	*0.1*	0.8	*0.3*	1.1	*0.3*	0.8	*0.1*	1.2	*0.2*	1.6	*0.4*
Co		>40	-	>50	-	>50	-	>40	-	>60	-	80	*20*	>100	-	>30	-	80	*20*
Zn		2.0	*0.7*	1.3	*0.3*	4	*3*	4.9	*0.5*	6	*1*	1.9	*0.4*	>1	-	2.2	*0.3*	2.2	*0.3*
Mo		29	*4*	6	*1*	14	*3*	32	*6*	30	*4*	45	*4*	28	*3*	50	*10*	30	*5*
W	$x10^{-3}$	0.7	*0.1*	3	*1*	0.2	*0.1*	13	*5*	27	*8*	1.0	*0.4*	0.8	*0.1*	2	*1*	0.4	*0.2*
Re		-	-	-	-	-	-	>4	-	>3	-	-	-	>9	-	>4	-	-	-
Th	$x10^{-3}$	-	-	-	-	-	-	<10	-	<55	-	-	-	<3	-	<3	-	-	-
U	$x10^{-3}$	-	-	-	-	-	-	<10	-	<11	-	-	-	<4	-	<8	-	-	-
$D^{Fe-S-O/melt}$																			
Ti		1.0	*0.4*	0.9	*0.1*	5	*2*	1.0	*0.8*	3	*1*	5	*2*	0.34	*0.09*	0.19	*0.04*	0.3	*0.1*
V		20	*7*	22	*3*	>40	-	9	*7*	30	*20*	20	*10*	5	*1*	2.2	*0.7*	2.1	*0.4*
Mn		2.8	*0.4*	3.1	*0.6*	4	*1*	1.5	*0.3*	2.0	*0.6*	2.4	*0.6*	1.5	*0.2*	2.3	*0.4*	5	*1*
Co		>20	-	>20	-	>20	-	>20	-	>20	-	27	*7*	>60	-	>20	-	37	*8*
Zn		2.3	*0.8*	2.4	*0.5*	8	*6*	13	*1*	18	*4*	5	*1*	>3	-	5.1	*0.7*	9	*1*
Mo		190	*20*	160	*30*	100	*20*	80	*10*	55	*7*	120	*10*	84	*8*	110	*30*	80	*10*
W		9	*4*	15	*7*	5	*2*	6	*2*	3.0	*0.9*	15	*5*	6	*1*	20	*10*	4	*2*
Re		-	-	-	-	-	-	-	-	-	-	-	-	-	-	-	-	-	-
Th		-	-	-	-	-	-	0.03	*0.01*	0.11	*0.06*	-	-	0.012	*0.004*	0.05	*0.02*	-	-
U		-	-	-	-	-	-	0.06	*0.02*	0.3	*0.3*	-	-	0.03	*0.01*	0.06	*0.03*	-	-

$x10^{-3}$ = Actual value equals listed value times 10^{-3}

< and > indicate that the value is known in one phase, but is below detection in the other.

Table 11 $D^{Fe\text{-}S\text{-}O/po}$ from both series of experiments

	20 Minutes						200 Minutes						2000 Minutes					
(Cu,Ag,Au)	**22a**	$1\sigma_{\bar{x}}$	**22b**	$1\sigma_{\bar{x}}$	**22c**	$1\sigma_{\bar{x}}$	**21a**	$1\sigma_{\bar{x}}$	**21b**	$1\sigma_{\bar{x}}$	**21c**	$1\sigma_{\bar{x}}$	**20a**	$1\sigma_{\bar{x}}$	**20b**	$1\sigma_{\bar{x}}$	**20c**	$1\sigma_{\bar{x}}$
Si	>90	-	>80	-	>80	-	>80	-	>90	-	-	-	>70	-	>80	-	-	-
Mn	2.8	*0.3*	5	*2*	1.7	*0.2*	3.2	*0.5*	2.5	*0.5*	2.8	*0.4*	4.3	*0.9*	2.2	*0.6*	1.8	*0.1*
Cu	2.7	*0.4*	1.19	*0.08*	0.45	*0.06*	1.2	*0.1*	1.1	*0.2*	0.8	*0.1*	2.0	*0.2*	1.32	*0.07*	0.71	*0.04*
Ag	14	*7*	1.1	*0.1*	1.6	*0.4*	1.8	*0.3*	1.3	*0.2*	5	*2*	2.0	*0.5*	1.5	*0.5*	1.8	*0.4*
Au	8	*6*	1.2	*0.6*	0.6	*0.2*	0.9	*0.2*	1.1	*0.2*	10	*6*	5	*2*	1.6	*0.6*	1.5	*0.2*
(Mo,W)	**17a**	$1\sigma_{\bar{x}}$	**17b**	$1\sigma_{\bar{x}}$	**17c**	$1\sigma_{\bar{x}}$	**16d**	$1\sigma_{\bar{x}}$	**16e**	$1\sigma_{\bar{x}}$	**16f**	$1\sigma_{\bar{x}}$	**18a**	$1\sigma_{\bar{x}}$	**18b**	$1\sigma_{\bar{x}}$	**18c**	$1\sigma_{\bar{x}}$
Si	>90	-	>80	-	-	-	>80	-	>90	-	-	-	>90	-	>80	-	-	-
Ti	90	*40*	70	*10*	150	*30*	60	*50*	110	*60*	110	*40*	11	*3*	6	*1*	9	*2*
V	>50	-	>30	-	>60	-	>20	-	>60	-	>120	-	>10	-	5	*1*	6.9	*0.7*
Mn	2.0	*0.2*	2.5	*0.1*	1.5	*0.2*	2.1	*0.2*	2.5	*0.2*	2.2	*0.2*	2.0	*0.1*	2.0	*0.1*	2.9	*0.6*
Co	0.55	*0.04*	0.5	*0.1*	0.49	*0.08*	0.48	*0.4*	0.32	*0.02*	0.36	*0.08*	0.50	*0.06*	0.6	*0.1*	0.45	*0.05*
Zn	1.15	*0.08*	1.8	*0.3*	1.8	*0.1*	2.6	*0.3*	3.1	*0.5*	2.7	*0.3*	2.5	*0.2*	2.3	*0.2*	4.2	*0.2*
Mo	6	*2*	25	*12*	7	*2*	2.5	*0.2*	1.8	*0.2*	2.6	*0.3*	3.0	*0.2*	2.4	*0.4*	2.8	*0.3*
W x10^{+3}	12	*7*	6	*5*	20	*10*	0.5	*0.3*	0.10	*0.08*	15	*6*	8	*3*	8	*4*	11	*6*
Re	-	-	-	-	-	-	<0.6	-	<1	-	<1	-	<0.6	-	<1	-	<2	-
Th	-	-	-	-	-	-	>3	-	>20	-	>20	-	>4	-	>20	-	>20	-
U	-	-	-	-	-	-	>6	-	>30	-	>40	-	>7	-	>7	-	>10	-

x10^{+3} = Actual value equals listed value times 10^{+3}

< and > indicate that the value is known in one phase, but is below detection in the other.

Partition coefficients for Au, Ag, and Cu are plotted in figure 13 against the run time of the experiments, allowing for equilibrium to be evaluated through change over time. In some cases the actual value is not known and is indicated with a triangle indicating less than or greater than the value shown.

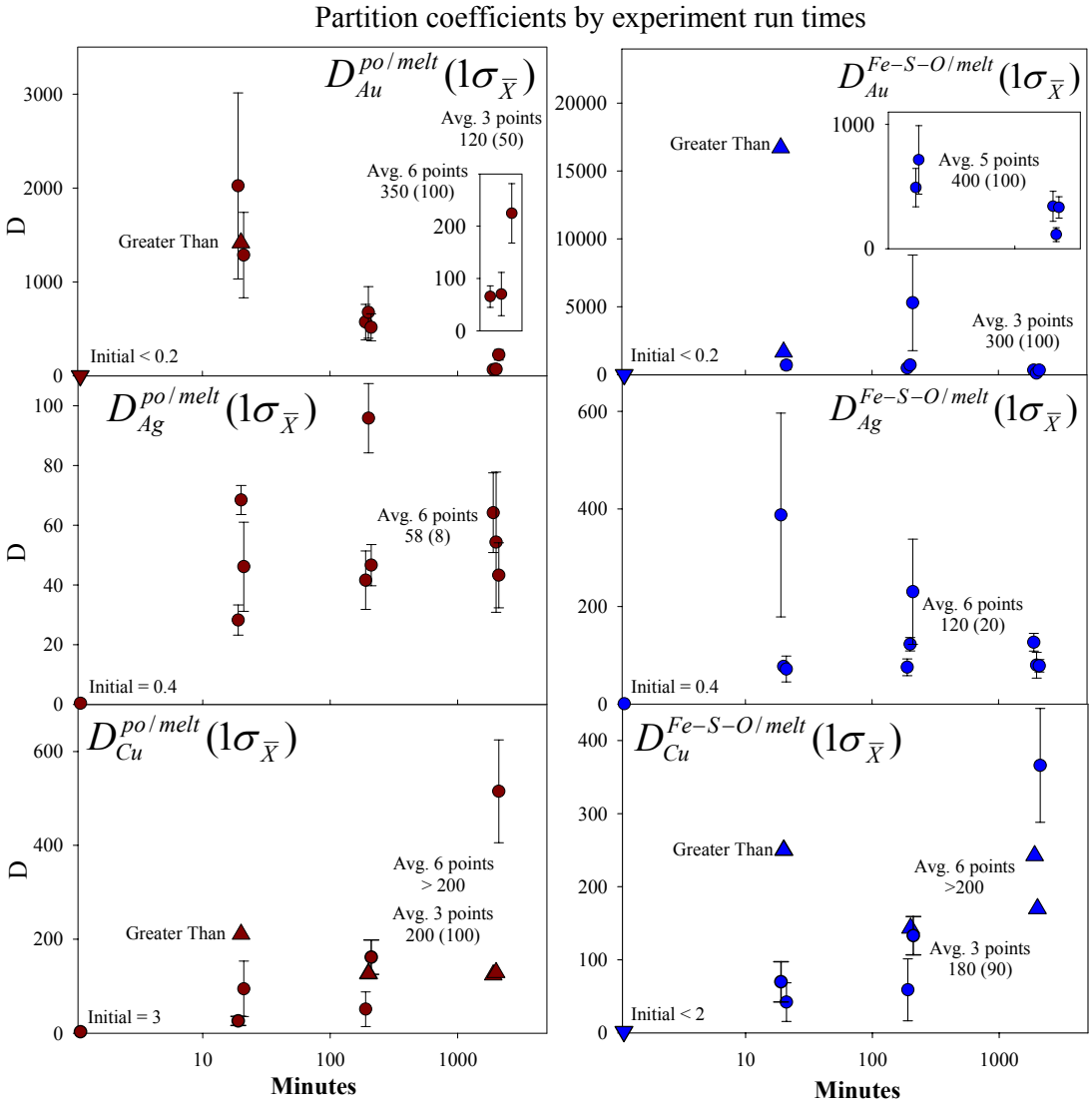

Figure 13 Plots of $D^{po/melt}$ and $D^{Fe\text{-}S\text{-}O/melt}$ for Cu, Ag, and Au vs. time.

Comparisons of $D^{po/melt}$ and $D^{Fe\text{-}S\text{-}O/melt}$ reveal similar trends. Tighter clusters of data in longer run-time experiments are taken as a sign of equilibrium along with decreasing rate of change between time periods. In this plot, triangles indicate that the actual value is unknown, but it is known to be greater-than (point-up triangle) the value given.

The initial ratios of an element between starting materials do not represent partition coefficients since these materials were not formed together or equilibrated, but does indicate the initial distribution of elements within the experiment. The starting concentration of Fe-S-O is calculated based on the contribution of the mt and po from which it is formed. The 20 minute run replicates are typically non-overlapping or only with slightly overlapping uncertainties. A trend of tighter grouping of the data points and consistent or slowly changing average D's are taken together as evidence of equilibrium in the experiment. In the case of Ag and Au, equilibrium has been reached at some time between 200 and 2000 minutes. It is likely that the 200 minute samples are near equilibrium. This can be seen in the rate of change of partition coefficients between different time intervals. From 20-200 minutes both $D_{Au}^{Fe-S-O/melt}$ and $D_{Au}^{po/melt}$ changed by an average of greater than 20% per hour, while from 200-2000 minutes, they changed by less than 3% per hour. Cu concentrations in the silicate melt were below detection by EMPA and LA-ICP-MS for many of the sample analyses (triangles). This was a function of the high background on both ^{63}Cu and ^{65}Cu. Later analyses focusing on Cu were able to provide statistically significant values. $D_{Cu}^{Fe-S-O/melt}$ was determined from WDS data to be 1.2±0.2 (>200 minute runs).

Mo and W show similar trends in partition coefficients with time in figure 14, with the exception of W which behaved incompatibly in po. Mo appears to reach equilibrium between 20 and 200 minutes. Although there is scatter in the data at $1\sigma_{\bar{X}}$, this is a fairly tight spread and these uncertainties would overlap at $2\sigma_{\bar{X}}$.

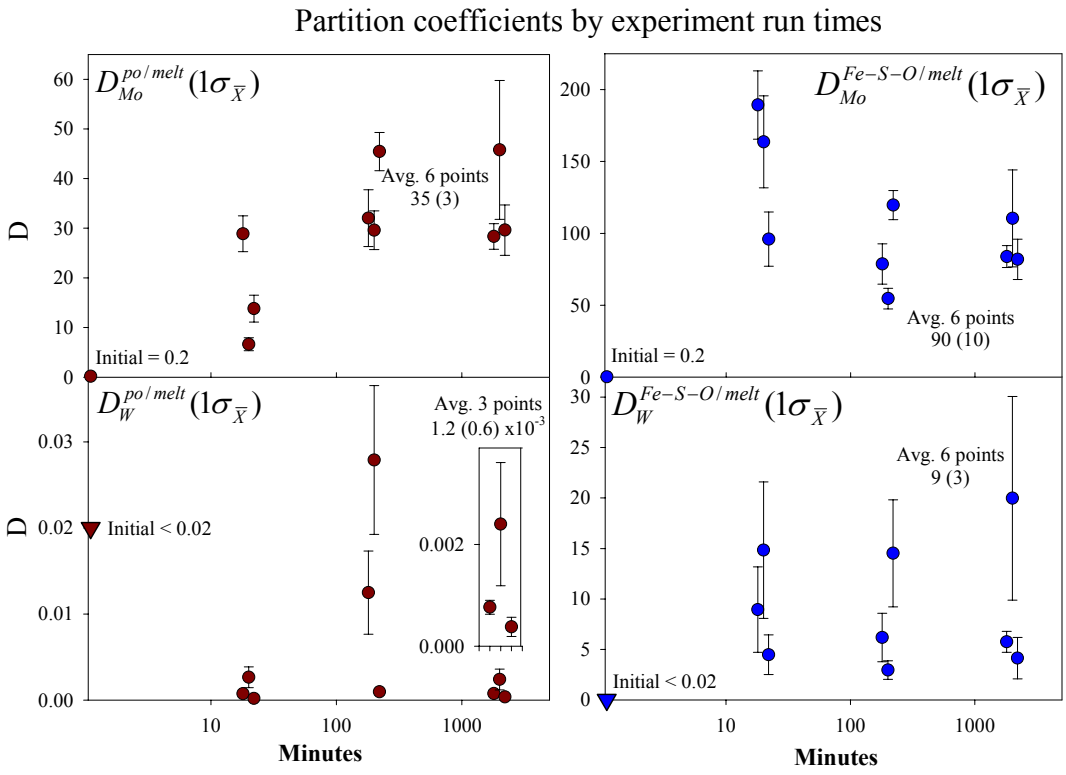

Figure 14 Plots of $D^{po/melt}$ and $D^{Fe\text{-}S\text{-}O/melt}$ for Mo and W vs. time.

$D_{Mo}^{po/melt}$ increases and $D_{Mo}^{Fe-S-O/melt}$ decreases over time, possibly indicating that Fe-S-O quickly incorporated the Mo and later lost it to other phases. The estimated starting ratio (Fe-S-O/melt) for W is <0.02. $D_{W}^{Fe-S-O/melt}$ has risen from this during the experiments, but remains roughly constant between time periods.

On review of the data on W, it is clear that a small number of analyses of po in the 200 minute experiments have a disproportionately high concentration that may be due to the inclusion of a very small amount of Fe-S-O or wo in the analyzed volume. Corroborating evidence for this identification was not apparent in other elements, preventing the removal of these points. Barring these two points, $D_{W}^{po/melt}$ and $D_{W}^{Fe-S-O/melt}$ remain nearly constant from 20 to 2000 minutes. The calculated starting ratio for both Fe-S-O/melt and po/melt is <0.02, clearly rising in the case

of $D_W^{Fe-S-O/melt}$. The concentration of W in the silicate melt rises from 1.27±0.07ppm in the staring material to an average of ~ 300ppm in the 20 minute run-time samples, and remains roughly constant in longer experiments. This is in contrast to the majority of the elements studied which take longer to reach a stable concentration in the melt. Based on this early change in concentration followed by a stable values in longer runs, $D_W^{po/melt}$ is considered to have reached equilibrium in the 2000 minute sample despite the flat profile of the D plot.

Some elements enter the system with the mt, po, and glass. See Appendix C for plots for Ti, V, Zn, Co, Re, Th, and U determined in this way. Some are also included in the added 'doping' phases cp, sp, mb, and wo. These dual modes of delivering elements into the system allow for evaluation of their differences (figure 15).

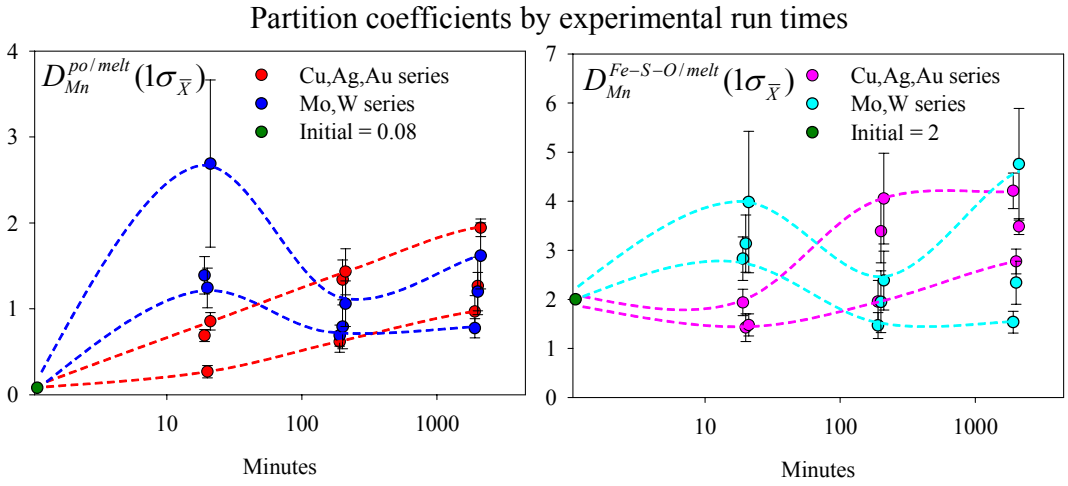

Figure 15 Plots of Mn partitioning vs. time in all experiments.

Rising $D_{Mn}^{po/melt}$ and $D_{Mn}^{Fe-S-O/melt}$ in the group 11 (red or pink) experiments is due to Mn coming from the glass while group 6 (blue and light blue) experiments have additional Mn from the wolframite which must diffuse into the glass, yielding dropping D's. Colored lines highlight the range of average values.

The group 6 series experiments have additional Mn added as a component of wo. In the first example, Mn must diffuse out of the glass phase. In the second example, the additional Mn must diffuse into the glass phase. Graphs of $D_{Mn}^{po/melt}$ and $D_{Mn}^{Fe-S-O/melt}$ converge over time. This indicates that either method yields the same result once equilibrium has been reached.

Partition coefficients determined in this study are summarized in table 12.

Table 12 Summary of equilibrium partition coefficients

	$D^{po/melt}$	$1\sigma_{\bar{x}}$	*n*	$D^{Fe\text{-}S\text{-}O/melt}$	$1\sigma_{\bar{x}}$	*n*	$D^{Fe\text{-}S\text{-}O/po}$	$1\sigma_{\bar{x}}$	*n*
Si	-	-	-	-	-	-	>80	-	*8*
Ti	0.030	*0.002*	*6*	0.28	*0.05*	*3*	9	*1*	*3*
V	<0.4	-	*6*	3.1	*0.9*	*3*	>8	-	*3*
Mn	1.1	*0.1*	*12*	2.9	*0.3*	*12*	2.5	*0.2*	*12*
Co	>70	-	*6*	>30	-	*6*	0.52	*0.05*	*6*
Cu	>200	-	*6*	>200	-	*6*	1.2	*0.2*	*6*
Zn	3.4	*0.4*	*5*	10	*1*	*5*	2.9	*0.3*	*6*
Mo	35	*3*	*6*	90	*10*	*6*	2.5	*0.3*	*6*
Ag	58	*8*	*6*	120	*20*	*6*	2.2	*0.6*	*6*
W	0.0012	*0.0006*	*3*	9	*3*	*6*	9000	*1000*	*3*
Re	>4	-	*4*	-	-	-	<1	-	*6*
Au	120	*50*	*3*	300	*100*	*3*	3	*1*	*3*
Th	<0.005	-	*4*	0.05	*0.02*	*4*	>10	-	*2*
U	<0.008	-	*4*	0.12	*0.07*	*4*	>7	-	*2*

n = number of samples in the average, > and < indicate that one phase is below detection

The list includes elements with likely valences from +1 to +6, and partition coefficients that span 3 to 5 orders of magnitude. Graphs of the data in figures 16 and 17 show how similar the two sulfide phases behave. Exceptions to the general trend are Co and Re, with $D^{Fe\text{-}S\text{-}O/melt} < 1$, and W with $D^{Fe\text{-}S\text{-}O/melt} = 9000$. The lithophile elements behave similarly as a group. In figure 16 the siderophile and chalcophile elements overlap. In figure 17, the chalcophile elements all behave similarly, and Mo and Mn behave more like these than the other siderophile element, Co. Based on this similarity, Mo is likely present in the Fe-S-O melt as MoS_2, as opposed to MoO_2. W

is most similar to Si in behavior, and is likely present as WO_2. Published values are included from section 1, which are summarized in table 13.

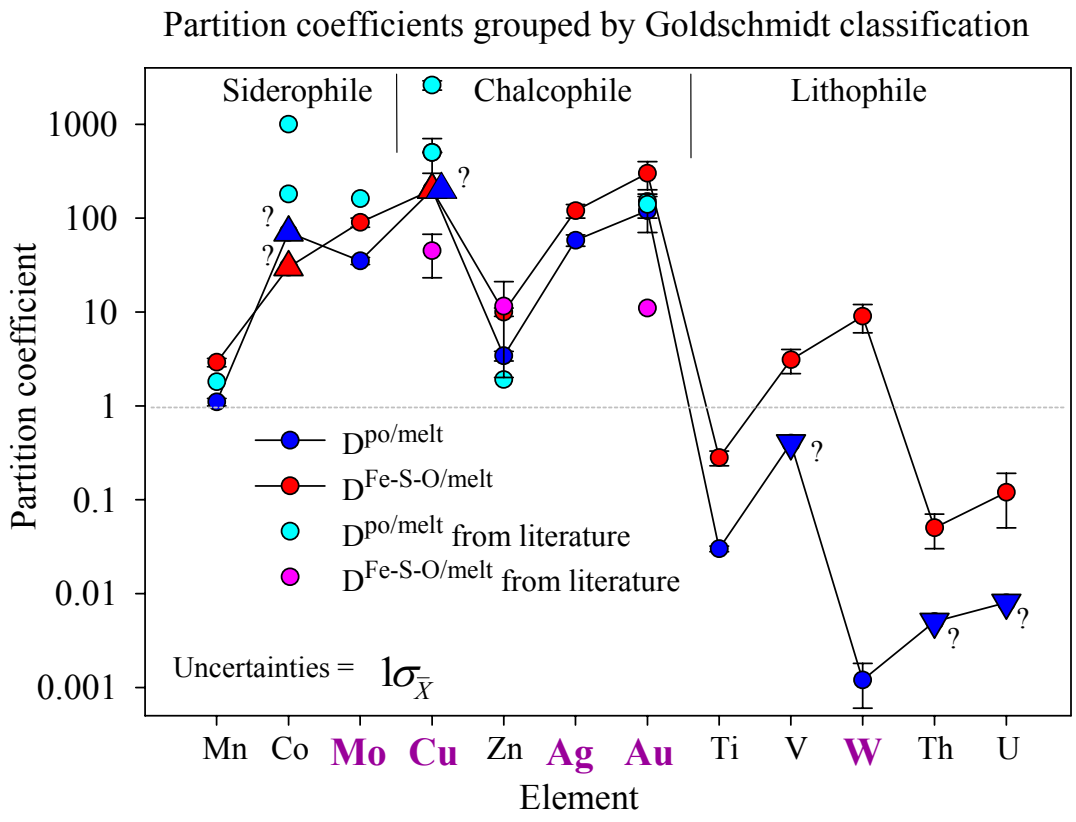

Figure 16 Comparison of $D^{sulfide/melt}$ among elements

$D^{Fe\text{-}S\text{-}O/melt}$ follows $D^{po/melt}$ but at higher values, except for Co. D's grouped by Goldschmidt classification highlight that lithophile elements behave incompatibly in po as expected. V and W are compatible in Fe-S-O. Published values are from table 13. Upward or downward pointing triangles with question marks indicate greater-than or less-than the value shown.

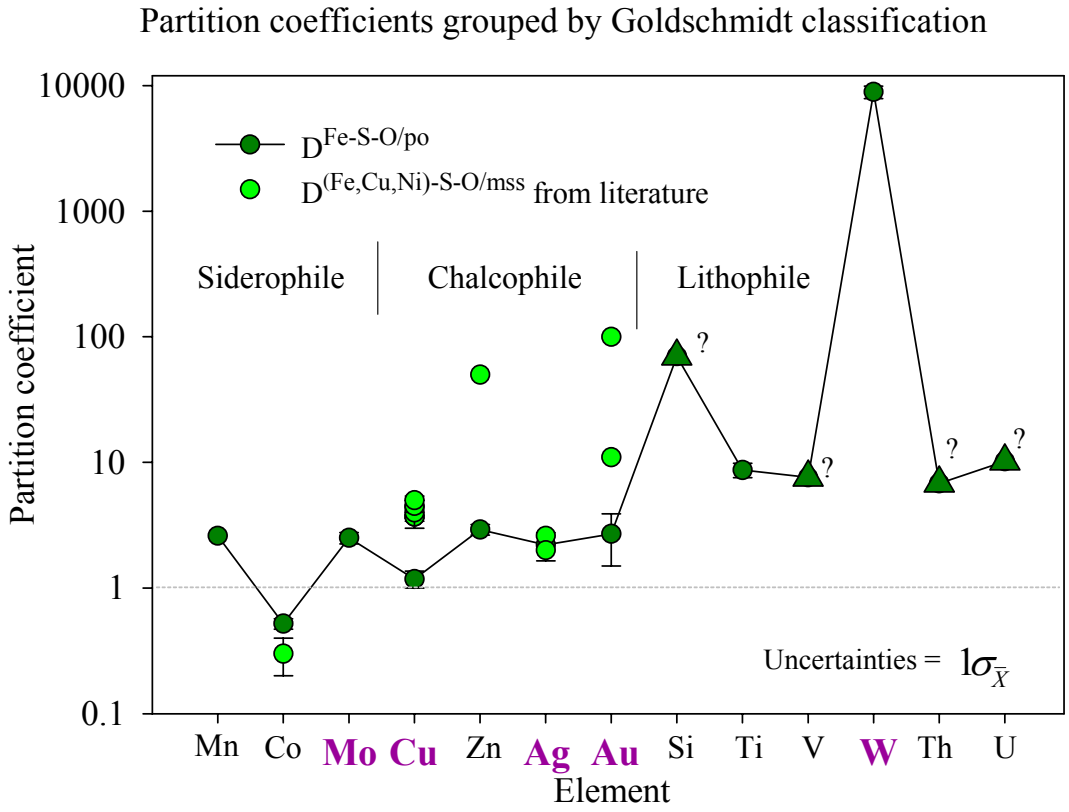

Figure 17 Comparison of $D^{Fe\text{-}S\text{-}O/po}$ among elements

Lithophile elements all plot higher than siderophile and chalcophile elements, as expected. Mn and Mo behave more similarly to the chalcophile elements than to the other siderophile elements Co. W is most similar in behavior to Si. Published values are from table 13. Upward pointing triangles with question marks indicate greater-than the value shown.

In addition to the concentrations in po, Fe-S-O, and silicate melt presented, some additional concentrations were determined by WDS in mt. Mn & Ti in mt appear to have reached equilibrium on a time scale similar to the other phases in the experiment with $D_{Mn}^{mt/melt} = 2.0\pm0.3$, $D_{Ti}^{mt/melt} = 16\pm4$, $D_{Mn}^{Fe-S-O/mt} = 0.9\pm0.1$, and $D_{Ti}^{Fe-S-O/mt} = 0.09\pm0.06$. W and Mo have a jump in concentration from below the detection limit (less than ~50ppm) at 20 and 200 minutes to ~ 100ppm (W) and greater than 1000ppm (Mo) at 2000 minutes. This is taken as an indication that Mo

and W have much slower diffusion rates within mt, and that equilibrium may or may not have been achieved. As such, the following partition coefficients should be interpreted only as guides for future research directions: $D_W^{mt/melt} = 0.7\pm0.3$, $D_{Mo}^{mt/melt} = 60\pm10$, $D_W^{Fe-S-O/mt} = 17\pm3$, and $D_{Mo}^{Fe-S-O/mt} = 1.7\pm0.1$.

Comparisons of the partition coefficients determined in this study and published values can be made for some elements. Table 13 includes select $D^{po/melt}$, $D^{Fe\text{-}S\text{-}O/melt}$, and $D^{Fe\text{-}S\text{-}O/po}$ (a subset of $D^{(Fe,Cu,Ni)\text{-}S\text{-}O/mss}$) from this study, as well as studies listed in section 1. Differences in partition coefficients may be due to differences in temperature, pressure, silicate melt composition, Fe-S-O melt composition, fS_2, or fO_2. $D_{Cu}^{po/melt}$ varies greatly (~10x) between these sources. $D^{po/melt}$ Co, Ag, and Cu display a large range of partition coefficients. The large discrepancy between this study and Englander (2005) may be due to the very large differences between the compositions of the glass between the two experimental systems.

Table 13 Comparison of partition coefficients with published values

$D^{po/melt}$	Cu	Ag	Au	Mo	Co	Zn	Mn
This Study	>200	58±8	120±50	35±35	> 70	3.4±3.4	1.1±0.1
Stimac and Hickmott (1994)	~499-502			161	~999		
Yang et al. (2006)			150±83				
Stuller (2001)					180±20	1.9±0.3	1.8±0.1
Lynton (1993)	500±200						
Jugo (1999)	2600±300		140±40				
Englander (2005)		~2000					

$D^{Fe\text{-}S\text{-}O/melt}$	Cu	Ag	Au	Mo	Co	Zn	Mn
This Study	>200			90±10		10±1	
Stimac and Hickmott (1996)	23-67			11		2-21	

$D^{(Fe,Cu,Ni)\text{-}S\text{-}O/mss}$	Cu	Ag	Au	Co	Zn	Re
This Study ($D^{Fe\text{-}S\text{-}O/po}$)	1.2±0.2	2.2±0.6	3±1	0.52±0.05	2.9±0.3	<1
Fleet et al (1993)	3.7		11			
Li et al. (1996)	4-5					
Peregoedova et al. (2006)	3-5	2				
Ballhaus et al. (2001)	3.4-5.3					
Brenan et al. (2002)	3.6-3.8					0.4
Mungall et al. (2005)	5		100			
Barnes et al. (2006)		2.6		0.2-0.4	50	0.1-0.2

Partition coefficients from this study and those listed in section 1. Although it is generally true that elements determined to be compatible in other studies are compatible in this one, the magnitude of the partition coefficients can vary greatly. This may be due to differences in temperature, pressure, silicate melt composition, Fe-S-O melt composition, fS_2, or fO_2.

Partition coefficients are expected to vary between Fe-S-O melts of different compositions which can contain other major elements such as Cu or Ni and varying proportions of S and O. Despite this, the experimental values from this study are not greatly different from those determined by Stimac and Hickmott (1996). Data available from studies of other immiscible sulfide-oxide melts that also indicate that Co and Re prefer a solid iron sulfide phase.

With the range of elements and partition coefficients determined here, it is possible to look for some trends in the behavior of the elements. Figure 18A is a plot of $D^{po/melt}$ against the likely valence state of each element divided by its ionic size in the octahedrally coordinated sites of pyrrhotite. There is a general trend of increasing compatibility with decreasing charge to size ratio. Several of the points plotted are

only known to be less-than or greater-than the values listed, and may actually be at a position much lower or higher than that indicated.

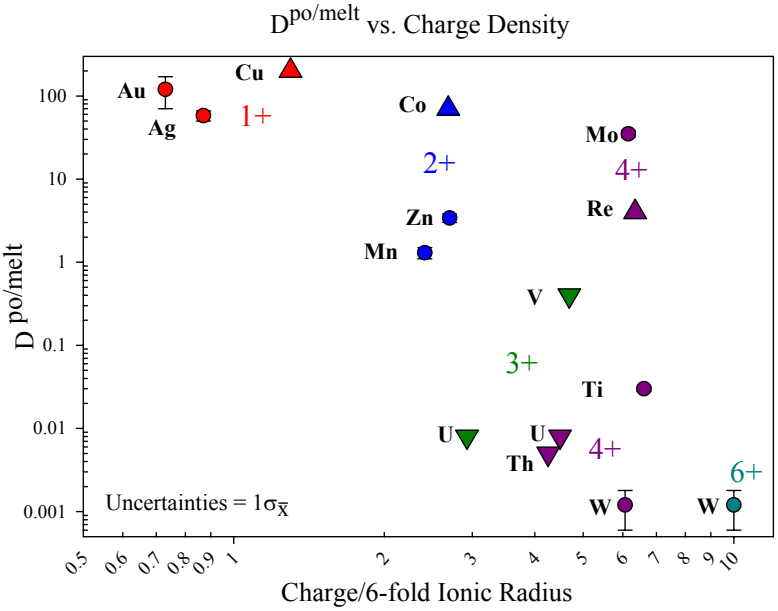

(A) $D^{po/melt}$ vs. the ratio of ionic charge to ionic radius in 6-fold coordination for each element studied. Common valences are plotted for each element. Cu, Ag, and Au plot away from the majority of the elements, and there is a general trend of increasing compatibility in po with decreasing charge:size ratio.

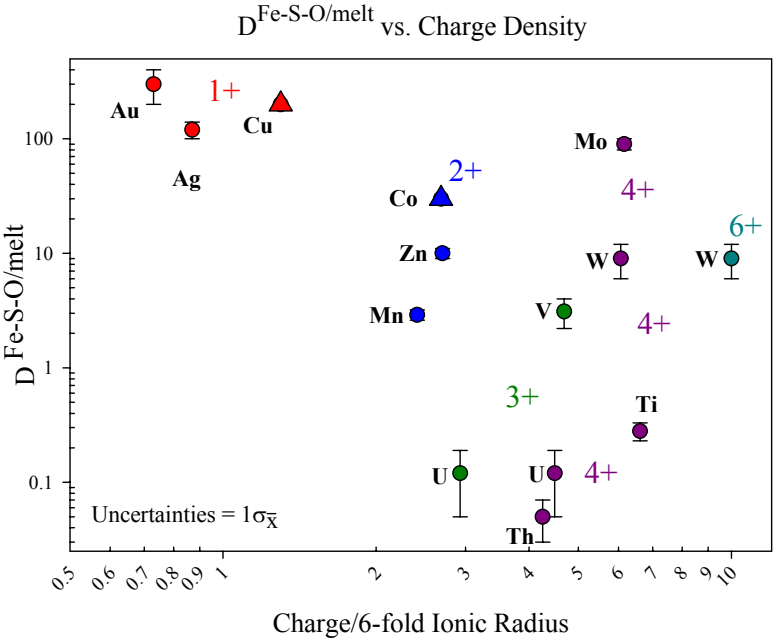

(B) This plot using $D^{Fe-S-O/melt}$ is very similar to the plot above despite the lack of crystal structure. Note the change in W position.

Figure 18 Plots of partition coefficient vs. charge:radius ratio

Figure 18 shows that $D^{Fe-S-O/melt}$ is very similar, which is surprising since there are no crystal sites in the Fe-S-O melt. There may be some other charge/size relationship at

work in this case. Based on the general trend displayed here, future studies might find large partition coefficients for elements with a possible charge/radius ratio of less than 1, such as: Na, K, Rb, Cs, and Hg. Since the silicate glass contains ~2 wt. % Na_2O and ~6 wt. % K_2O, a large partition coefficient would have resulted in several weight percent Na and K in the po and Fe-S-O melt, which would have been easily detected in the totals if they were present. It is likely that this apparent trend is not applicable to non transition metals; however Hg may still be a possible candidate for investigation.

Since partitioning behavior can be strongly affected by differences in experimental conditions, a preliminary experiment has been performed to test three of these conditions: melt major element composition, melt hydration, and pressure (figure 19).

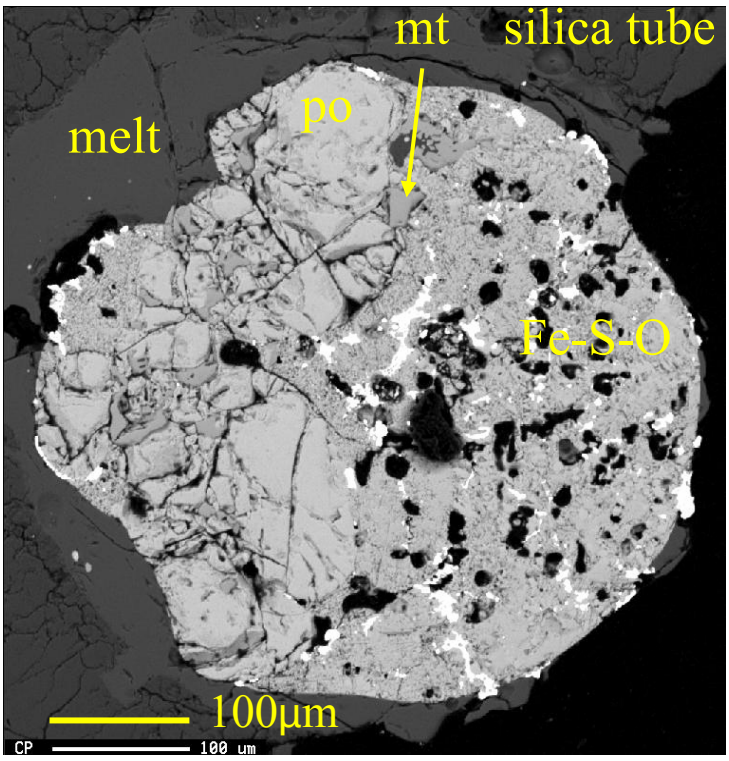

BSE image of a cross section of run 30, a high pressure (50-100MPa) experiment containing a dacite melt from Mt. St. Helens. Phases shown include a portion of the silica tube, quenched melt, po, mt, Fe-S-O melt, and high atomic weight blebs (white), consisting of Au+Ag and Ag+S (by EDS). Partition coefficients are similar to those determined in the main experiments of the study.

Figure 19 BSE image of high pressure run product

This experiment was run for 200 minutes in an evacuated sealed silica tube at the same temperature, and with the same starting po, mt, and sources of Au, Ag, and Cu as the other experiments in this study. The starting glass added to the experiment was a Mt. St. Helens dacite. Additional distilled water was added to a silica tube to establish greater total pressure at run temperature, and to establish higher water content in the melt. Based on ideal gas law calculations, the estimated pressure at 1038°C was ~100MPa, although it may have been as low as ~50MPa when calculating the incorporation of some water into the melt. Fluid inclusions containing a vapor and liquid phase at room temperature were present in the quenched melt glass, indicating they were formed from a single supercritical fluid. Given the large difference between the run temperature and the glass transition temperature, these inclusions cannot be used to give an accurate estimate of pressure. Analysis of the Fe-S-O melt and po in this experiment yielded $D_{Cu}^{Fe-S-O/po} = 1.5\pm0.1$, $D_{Ag}^{Fe-S-O/po} = 1.4\pm0.4$, $D_{Au}^{Fe-S-O/po} = 2.5\pm0.6$, and $D_{Mn}^{Fe-S-O/po} = 2.3\pm0.2$, where the uncertainty is the propagated standard deviation of the mean of the concentrations. Analysis of the glass in this experiment yielded one result for glass in obvious contact with the sulfide phases and another value for a more distal portion of the experimental charge. This experiment has a larger length to width ratio that the other experiments and this linearity may have been an additional hurdle for equilibration in the time available. Partition coefficients can be determined for this proximal glass; however it should be noted that the system as a whole may be in a state of disequilibrium. Given that only one glass analysis is being used, meaningful uncertainty is difficult to estimate, but

approximate values have been determined as: $D_{Cu}^{po/melt}$ ~200, $D_{Ag}^{po/melt}$ ~60, $D_{Au}^{po/melt}$ ~400, $D_{Mn}^{po/melt}$ ~1, $D_{Cu}^{Fe-S-O/melt}$ ~300, $D_{Ag}^{Fe-S-O/melt}$ ~80, $D_{Au}^{Fe-S-O/melt}$ ~900, $D_{Mn}^{Fe-S-O/melt}$ ~2. These values are similar to those for the low pressure, dry, rhyolitic melts with the exception of Au. The Au results may indicate a genuinely higher partition coefficient, or they may have been affected by the tendency of Au to be somewhat heterogeneous in saturated quenched melts, and by the large amount of high atomic weight blebs visible in the Fe-S-O melt (figure 4.20), which makes it more difficult to analyze a spot clear of additional phases. If these partition coefficients are confirmed by future studies, then the values determined in the main series of experiments are appropriate and applicable to modeling element partitioning in arc magmas of dacitic to rhyolitic composition and pressures up to 50MPa-100MPa.

5.4 Oxygen and Sulfur Fugacity

The concentration of Fe and S in the run product po allows for the determination of fS_2 and fO_2. Sulfur fugacity is determined from the composition of po by using the method of Toulmin and Barton (1964). By using equation 1, the mole fraction (X) of FeS within po in the system FeS-S_2 can be used to determine fS_2 for a given temperature (T) in Kelvin.

Equation 1 $$\log fS_2 = (70.03 - 85.83X)\left(1000/T - 1\right) + 39.30\sqrt{1 - 0.9981X} - 11.91$$

In a system at equilibrium containing mt and po, fO_2 can be determined following the method of Whitney (1984).

Equation 2

$$\log fO_2 = \left[-28.777 - 64.37\left(2\ln X - X + 1\right)\right]\left(1000/T - 1\right) + 29.42\left(2\tanh^{-1}\sqrt{1-0.9981X} - \frac{\sqrt{1-0.9981X}}{0.9981}\right) - 21.99$$

The fS_2 and fO_2 that correspond to a range of po compositions for different temperatures T are plotted in figure 21. This plot is contoured for temperature in degrees Celsius, po composition in weight percent Fe, as well as the NNO and QFM fO_2 buffers.

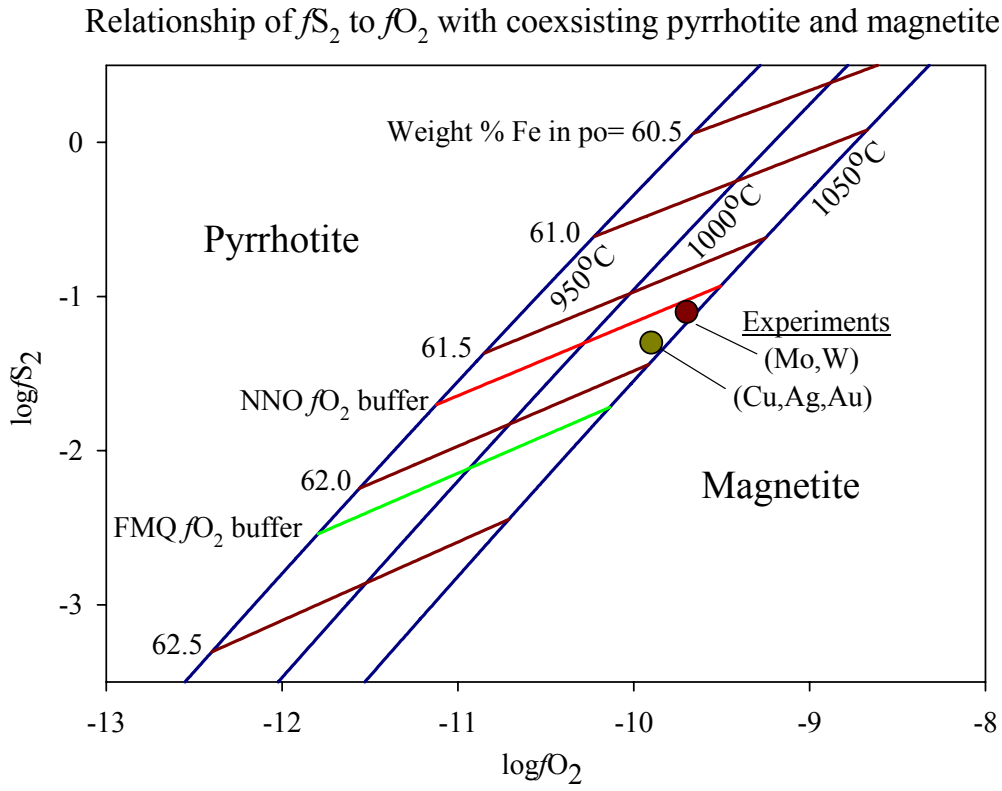

Figure 20 fS_2 and fO_2 of experiments

This is a plot of log fO_2 vs. log fS_2 for a system at equilibrium containing both po and mt determined using equations from Toulmin and Barton (1964) and Whitney (1984). Contours are temperature (blue), Fe content of po (brown), NNO fO_2 buffer (red), QFM fO_2 buffer (green). The average equilibrium conditions of the group 6 (Mo,W) experiments are shown as the tan circle, and the group 11 (Cu,Ag,Au) as the dark red circle. Uncertainties in the equations yield uncertainties on this graph of > 0.35 log unit fS_2 and fO_2. Both sets of experiments lie in the NNO-QFM range.

The average fugacity (200 and 2000 min runs) are plotted for the Group 11 (brown) and the Group 6 (tan) series of experiments. Toulmin and Barton report an estimated uncertainty on the equation relating log fS_2 to X_{FeS} of ±0.003 X_{FeS}, which results in a minimum uncertainty of log fS_2 ±0.35. It is clear from the graph that both experiments lie in the range of the NNO and FMQ buffers, which is in keeping with the range of oxygen fugacity reported in the natural iron sulfide bearing systems described in section 1 (figure 2).

5.5 Statements of Equilibrium and Equilibrium Constants

Whereas Nernst-style partition coefficients are useful for modeling, a more fundamental measure of the behavior of trace elements in the system are equilibrium constants, which allow the concentrations as well as the effects of sulfur and oxygen fugacity to be investigated. Working models are presented here as statements of equilibrium, hypothetical frameworks useful for understanding the reactions taking place that control partitioning. Models for Ag are presented which are also considered appropriate for Cu, and Au. In Jugo et al (1998) Cu present in the melt is assumed to be in the form of $CuO_{0.5}$. In keeping with that paper, the group 11 metals Cu, Ag, and Au in the silicate melt are evaluated as oxides in (1).

$$\tfrac{1}{2}\,\mu S_2^{sys} + \mu FeS^{po} + \mu AgO_{0.5}^{melt} = \mu AgFeS_2^{po} + \tfrac{1}{4}\,\mu O_2^{sys} \qquad (1)$$

From this statement of equilibrium, an equilibrium constant (K^o) can be formulated.

$$K^o_{(T,P)} = \frac{a^{po}_{AgFeS_2} \cdot \left(f^{sys}_{O_2}\right)^{0.25}}{\left(f^{sys}_{S_2}\right)^{0.25} \cdot a^{po}_{FeS} \cdot a^{melt}_{AgO_{0.5}}} \qquad (2)$$

$$K^{o}_{(T,P)} = \frac{\left(f^{sys}_{O_2}\right)^{0.25}}{\left(f^{sys}_{S_2}\right)^{0.25}} \cdot \frac{X^{po}_{AgFeS_2}}{a^{po}_{FeS} \cdot X^{melt}_{AgO_{0.5}}} \cdot \frac{\gamma^{po}_{AgFeS_2}}{\gamma^{melt}_{AgO_{0.5}}} \quad (3)$$

Assuming the ratio of activity coefficients *(γ)* is constant at low concentrations, K^o can be replaced by the effective equilibrium constant K which varies only with fugacity, activity, and mol fraction:

$$K_{(T,P)} = \frac{\left(f^{sys}_{O_2}\right)^{0.25}}{\left(f^{sys}_{S_2}\right)^{0.25}} \cdot \frac{X^{po}_{AgFeS_2}}{a^{po}_{FeS} \cdot X^{melt}_{AgO_{0.5}}} \quad (4)$$

$$K_{(T,P)} = \frac{\left(f^{sys}_{O_2}\right)^{0.25}}{\left(f^{sys}_{S_2}\right)^{0.25}} \cdot \frac{X^{po}_{Ag}}{a^{po}_{FeS} \cdot X^{melt}_{Ag}} \quad (5)$$

$$\frac{X^{po}_{Ag}}{X^{melt}_{Ag}} \approx \frac{C^{po}_{Ag}}{C^{melt}_{Ag}} = D^{po/melt}_{Ag} \quad (6)$$

$$K_{(T,P)} = \frac{\left(f^{sys}_{O_2}\right)^{0.25}}{\left(f^{sys}_{S_2}\right)^{0.25}} \cdot \frac{D^{po/melt}_{Ag}}{a^{po}_{FeS}} \quad (7)$$

In a system containing both po and mt, fS_2 and fO_2 can be determined from the composition of the po. Referring again to Toulmin and Barton (1964), equation 3 allows the composition of po as the mole fraction FeS in po (X) in the system FeS-S_2 to be used to determine the activity (a) of FeS in po, where T is in Kelvin.

Equation 3

$$\log a_{FeS} = 85.83\left(1000/T - 1\right)\left(1 - X + \ln X\right) + 39.30\sqrt{1 - 0.9981X} - 39.23\tanh^{-1}\sqrt{1 - 0.9981X} - 0.002$$

Therefore fS_2, fO_2, and the activity (a) of FeS in po can all be determined from the composition of the po. In the terms used in equation 3, for these experiments X = 0.96 (system FeS-S_2) and T = 1313K. Therefore a^{po}_{FeS} = 0.82. For (7) that yields K_{Au}=1.0, K_{Ag}=0.5, and K_{Cu}>1.7. The relationship among these three variables at the temperature, pressure, and fO_2 of interest can be seen in figure 21.

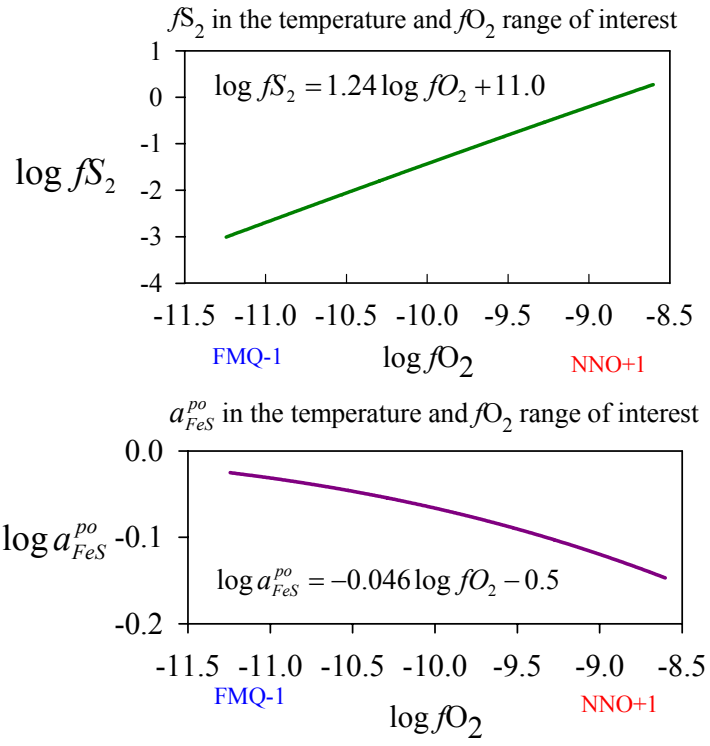

Figure 21 Simplified equations for log fS_2 and log a_{FeS}

Considering only the temperature and pressure of the experiments and a restricted range of fO_2, simple equations for fS_2 and a^{po}_{FeS} can be determined from regressions of points plotted using the equations of Toulmin and Barton (1964) and Whitney (1984). In environments where po and mt are in equilibrium, as fO_2 increases, fS_2 increases faster, and a^{po}_{FeS} decreases.

These simplified equations make it easier to see the relationships among fS_2, fO_2, and a^{po}_{FeS}. Using them, (7) can be re-written in terms of just fO_2 as (8).

$$K_{(T,P)} = \frac{D^{po/melt}_{Ag}}{160\left(f^{sys}_{O_2}\right)^{0.01}} \qquad (8)$$

In considering $D^{Fe\text{-}S\text{-}O/melt}$, it should be noted that Mungall (2007) describes a relationship between the Cu content of (Fe,Cu,Ni)-S-O melts and the oxygen content where increased Cu occurs with decreased O, which would be consistent with Cu (or

Ag, Au) preferring to associate with S in this phase as in equilibria (9).

$$\tfrac{1}{4}\,\mu S_2^{sys} + \mu AgO_{0.5}^{melt} = \mu AgS_{0.5}^{Fe-S-O} + \tfrac{1}{4}\,\mu O_2^{sys} \qquad (9)$$

Rearranging this in terms of K yields (10) with $K_{Au} = 2.1$, $K_{Ag} = 0.83$, and $K_{Cu} > 1.38$. Simplifying to just fO_2 yields (11).

$$K_{(T,P)} = \frac{\left(f_{O_2}^{sys}\right)^{0.25}}{\left(f_{S_2}^{sys}\right)^{0.25}} \cdot D_{Ag}^{Fe-S-O/melt} \qquad (10)$$

$$K_{(T,P)} = \frac{D_{Ag}^{Fe-S-O/melt}}{550\left(f_{O_2}^{sys}\right)^{0.06}} \qquad (11)$$

Mo and W equilibrium constants can be determined in the same manner as Cu, Ag and Au, assuming Mo and W are present as 4+ ions in the sulfide phases, and that MoO_2 or MoO_3 is the dominant form of molybdenum and WO_2 or WO_3 is the dominant form of tungsten in the silicate melts. In the following equilibria, WO_3 or MoO_3 in the silicate melt would require increasing the chemical potential of the O_2 product by $^3/_2$. The melt-po equilibrium makes use of a vacancy [v] in the exchange vector. Equilibria 12-15 apply to both Mo and W.

$$\mu S_2^{sys} + \mu MoO_2^{melt} = \mu 2FeS^{po} + \mu[v]Mo^{4+}Fe_{-2}^{2+\,po} + \mu O_2^{sys} \qquad (12)$$

$$K_{(T,P)}^{o} = \frac{\left(a_{FeS}^{po}\right)^2 \cdot a_{\mu[v]Mo^{4+}Fe_{-2}^{2+}}^{po} \cdot f_{O_2}^{sys}}{f_{S_2}^{sys} \cdot a_{MoO_2}^{melt}} \qquad (13)$$

$$K_{(T,P)} = \frac{f_{O_2}^{sys}}{f_{S_2}^{sys}} \cdot \left(a_{FeS}^{po}\right)^2 \cdot D_{Mo}^{po/melt} \qquad (14)$$

$$K_{(T,P)} = \frac{D_{Mo}^{po/melt}}{1.09\times10^{12} \cdot \left(f_{O_2}^{sys}\right)^{0.33}} \qquad (15)$$

The effective equilibrium constants for (14) are $K_{Mo} = 5.9\text{x}10^{-8}$ and $K_W = 1.8\text{x}10^{-12}$. The statement of equilibrium for Mo in the Fe-S-O melt (16, 17, and 18) is similar to

that for Cu, Ag, and Au, with $K_{Mo} = 2.3x10^{-7}$. This is in contrast to W (19) where $K_W \sim D_W$.

$$\mu S_2^{sys} + \mu MoO_2^{melt} = \mu MoS_2^{Fe-S-O} + \mu O_2^{sys} \quad (16)$$

$$K_{(T,P)} = \frac{f_{O_2}^{sys}}{f_{S_2}^{sys}} \cdot D_{Mo}^{Fe-S-O/melt} \quad (17)$$

$$K_{(T,P)} = \frac{D_{Mo}^{po/melt}}{9.16 \times 10^{10} \cdot \left(f_{O_2}^{sys}\right)^{0.24}} \quad (18)$$

$$\mu WO_2^{melt} = \mu WO_2^{Fe-S-O} \quad (19)$$

Using the equilibria determined here, experiments or natural systems at the same temperature and pressure as these experiments can be compared, and predictions can be made regarding changes in activities and fugacities. The effects of changes in fO_2 on $D_{Ag}^{po/melt}$ are plotted in figure 22.

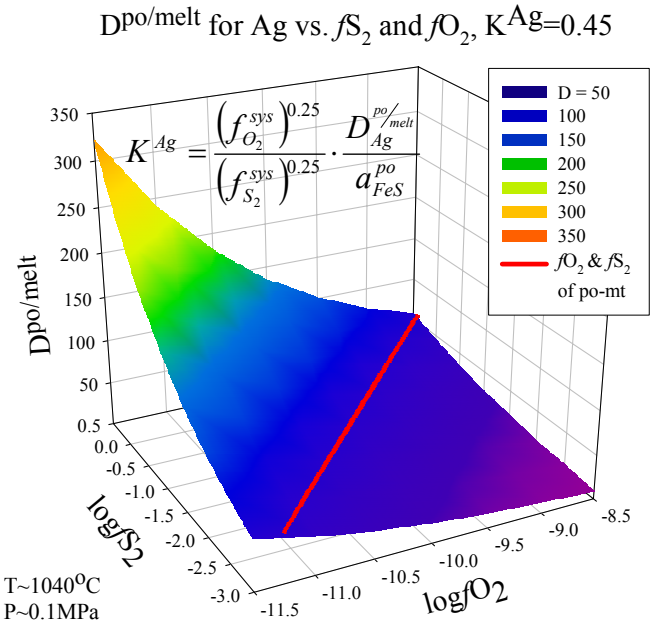

Figure 22 Predicted $D^{po/melt}$ for Ag with varying fS_2 and fO_2

Decreasing fO_2 and increasing fS_2 are expected to increase $D_{Ag}^{po/melt}$. In systems with po and mt in equilibrium (red line), the relationship between fO_2 and fS_2 is fixed and $D_{Ag}^{po/melt}$ cannot vary significantly.

The surface plotted here has increasing $D_{Ag}^{po/melt}$ at lower fO_2 and higher fS_2 than in these experiments. In order to reach the higher D's these must be allowed to vary independently, which cannot happen with po and mt in equilibrium. If the statement of equilibria is correct, this presents a useful relationship in that po and mt behave as a 'buffer' for $D_{Ag}^{po/melt}$. At a given pressure and temperature, when both minerals are present, the approximate partition coefficient can be determined without knowledge of fO_2 or fS_2. The same relationship can be seen in Figure 23 for $D_{Ag}^{Fe-S-O/melt}$.

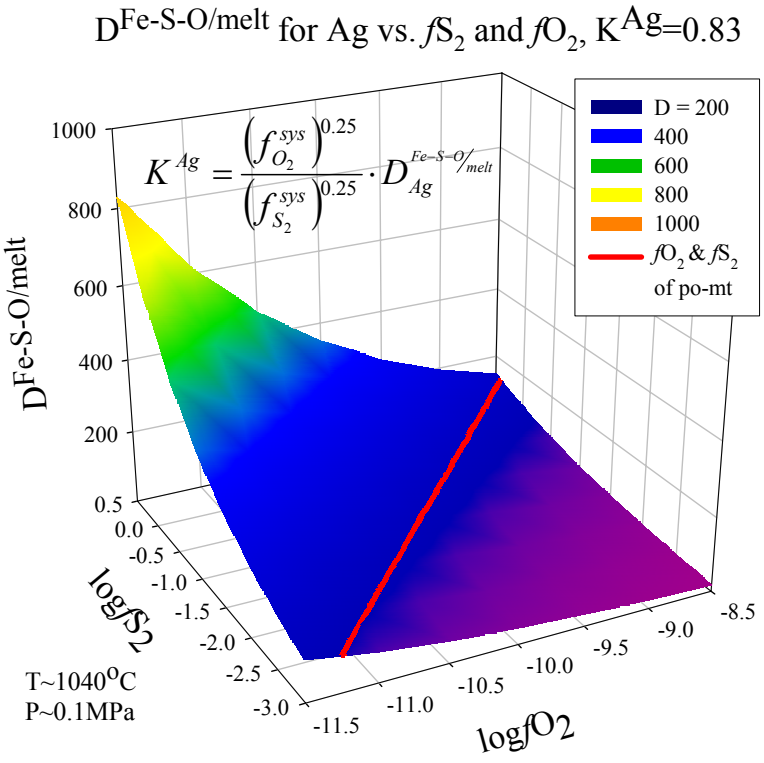

Figure 23 Predicted $D^{Fe-S-O/melt}$ for Ag with varying fS_2 and fO_2

As in the preceding figure (23), in systems with po and mt in equilibrium, the relationship between fO_2 and fS_2 is fixed and $D_{Ag}^{po/melt}$ cannot vary significantly.

The same relationships should hold true for Cu and Au, as they are modeled on the same equilibria. The degree to which D will change for each of the elements and phases modeled here is plotted against varying fO_2 in Figure 24.

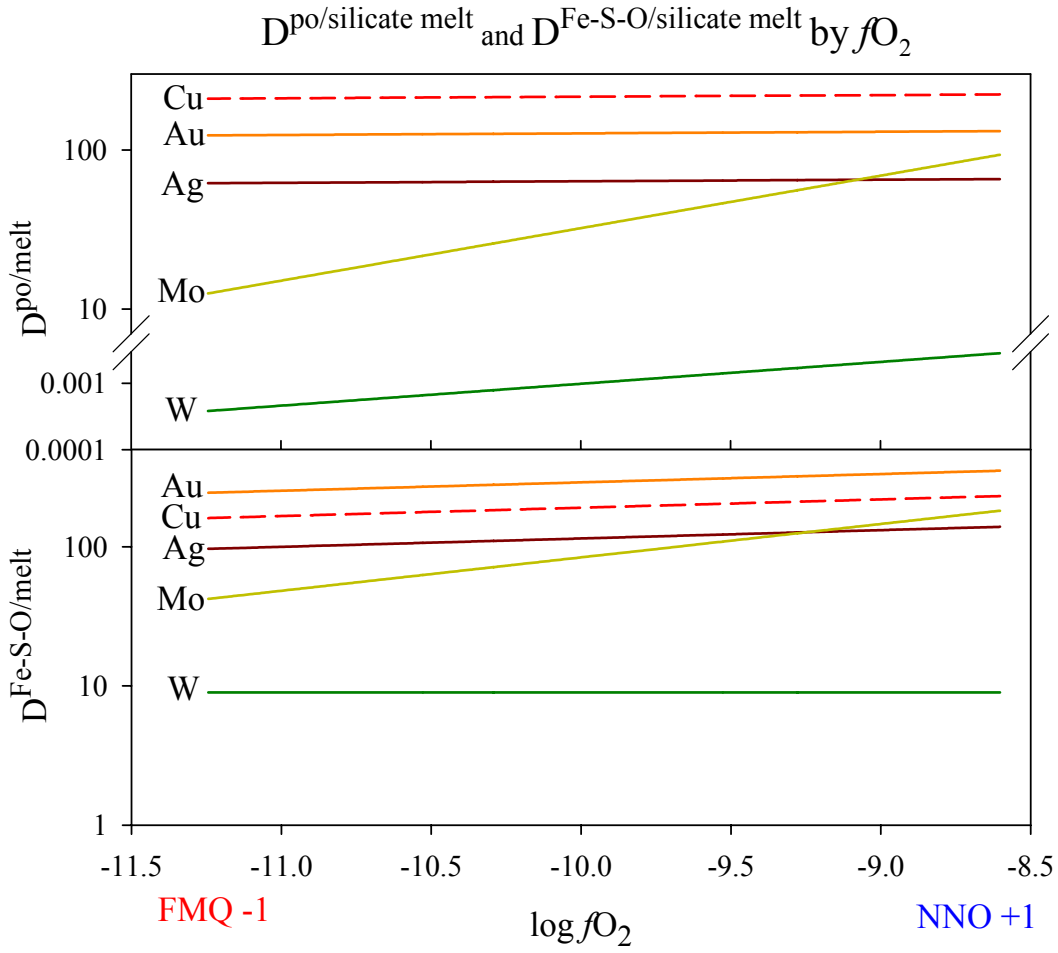

Figure 24 Predicted changes in $D^{sulfide/melt}$ for Ag, Au, Mo, and W.

Based on the statements of equilibria and equilibrium constants presented, the predicted change in partition coefficient with increasing or decreasing fO_2 is plotted here for Cu, Ag, Au, Mo and W in systems containing both po and mt under equilibrium conditions. $D_{Cu}^{po/melt}$ and $D_{Cu}^{Fe-S-O/melt}$ are predicted to be greater than the line (dashed red) shown.

6 Discussion

The partition coefficients determined in this study can be used to model the effect of removing Fe-S-O liquids on the metal budget of intermediate to felsic arc magmas. The results of the high pressure experiment and the predicted stability of partition coefficients with changes in oxygen fugacity provide justification in modeling broader systems. The presence and partitioning of the accessory phases studied here may prove to have an effect on models of the transport of elements throughout subduction arc systems. Since it is known that some of these magmas concentrate enough ore metal that later scavenging by volatile phases can create economically exploitable geochemical anomalies, understanding the extent to which Fe-S-O blebs may hinder this process may prove to be an aid in exploration. In modeling the magmas with which these ore deposits are associated, the assumption is made that less felsic melt undergoes crystal fractionation to produce the final rhyolite or dacite, and that the loss of the other phases separating into the cumulate have a minimal effect on the metals studied. Fe-S-O blebs are assumed to have multiple potential histories, some portion of the blebs will be trapped and isolated in the cooling crystal mush, and others will continue on with the melt and be lost with changes in temperature, and sulfur and oxygen fugacity. The total budget of the sequestered sulfur is assumed to consist of only magmatic po and Fe-S-O blebs. The standard form of rayleigh fractionation based on concentration (equation 4) can be reformulated to one based on mass (equation 5) where (M_i) is mass of the element of interest, (F) is the amount of crystallization expressed as the degree of fractionation (0 = complete crystallization), and $(\overline{D})$ is the bulk distribution coefficient. This

equation is used to determine the fraction of the original mass of the element of interest that is sequestered and the fraction that continues on with the melt and can be accessed by later processes.

Equation 4 $$C_i = C_i^0 F^{\overline{D}-1}$$

Equation 5 $$M_i = M_i^0 F^{\overline{D}}$$

A starting sulfide content of 0.1% (eg. Luhr et al. 1990) and a large degree of fractionation, F=0.1, can be used to determine an upper boundary on sequestration. Figure 25 illustrates the effect of sequestration on the metal budget.

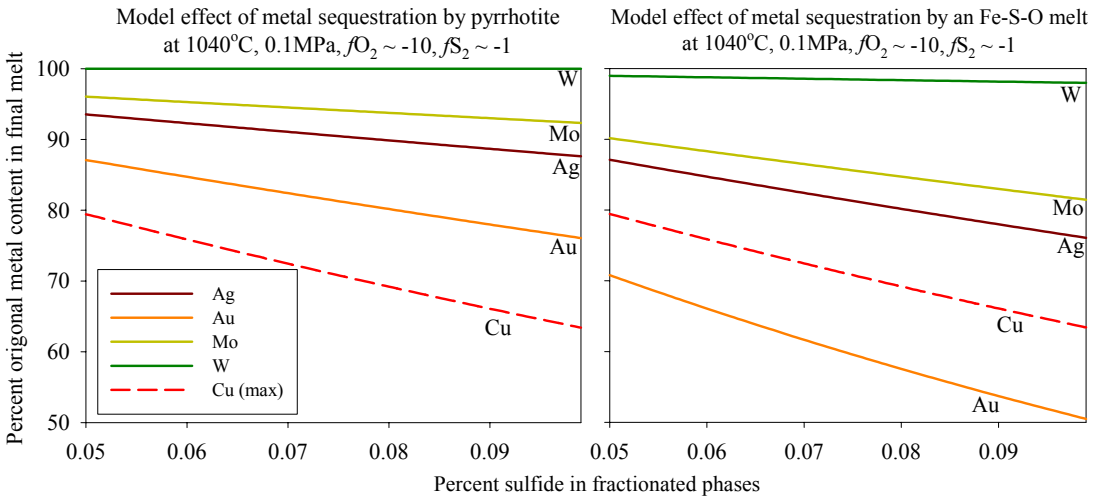

Figure 25 Effect of sequestration on metal budgets

These plots show the depletion caused by sequestering po (left) and Fe-S-O melt blebs (right). Copper content would be less-than the dashed line. In magmas devoid of sulfide, or where not of it has crystallized, none of the metals are lost. With increasing sulfide content and crystallization, less metal continues to the shallow evolved intrusions that are the potential source of metals for related porphyry, epithermal, or other hydrothermal deposits.

Sequestration of by Fe-S-O blebs would remove 50% Au, >37% Cu, 24% Ag, 19% Mo, and 2% W. Sequestration would also remove 2% Zn and >7% Co, while the

other elements in this study would not change. With the addition of mt to the calculation, where mt makes up 1% of the crystals, Mo sequestering rises to ~80%. In general, removal of a large amount of Fe-S-O blebs and po may deplete a magma and possibly prevent the formation of large Cu, Ag, Au, and Mo deposits.

Given the effect of sulfide crystallization on metal budgets is proposed to be strongly controlled by oxygen and sulfur fugacity, moving away from po-mt 'buffer' could lead to more substantial sequestration. The fO_2 range modeled thus far is based on the volcanic rocks described in section 1. However, these rocks are a sample of a specific time period in the protracted history of magmatic evolution. The magma may have undergone periods of higher or lower oxidation. Highly oxidized granites can be characterized by the presence of the opaque minerals mt as well as ilmentite (ilm), hematite (hm), and pyrite (py) or po, and reduced granites characterized by the presence of only ilmenite (ilm) and possibly po (Ishihara, 1977). These are both I-type granites of dominantly igneous origin. However, analysis of the sulfur isotopes implies that these rocks have non-mantle derived sulfur contributions. Figure 26 is a plot of the total sulfur content verses the $\delta\ ^{34}S$ (parts per thousand ‰) of mt and ilm series granitoids from Japan (Sasaki and Ishihara 1979).

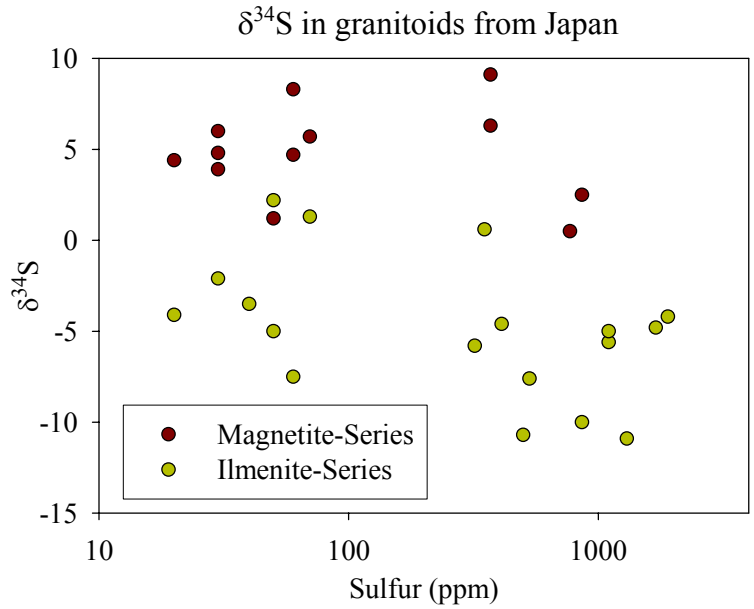

Figure 26 $\delta^{34}S$ vs. Sulfur (ppm) for granitoids from Japan

From Sasaki and Ishihara (1979). $\delta^{34}S$ ‰ for mt and ilm series granitoids are plotted against total sulfur content. The mt series plot above and the ilm series plot below Canyon Diablo troilite. Positive values indicate assimilation of heavy sulfur, possibly from pelagic trench sediments. Negative values indicate the assimilation of light sulfur is likely biogenic in origin.

The $\delta^{34}S$ of the mt series are positive and the ilm series negative, relative to Canyon Diablo troilite, which is representative of the S in the mantle. Raising the isotopic signature requires the addition of heavy sulfur, a likely source of which is sea-water, readily available from the subduction of water-laden pelagic sediments. Lowering the isotopic signature requires the addition of light sulfur which is generally associated with biogenic reduced sulfur. Selective assimilation of rock from an environment rich in sulfur-reducing bacteria which could lower the $\delta^{34}S$ would also increase the sulfide fraction of the melt and result in a lower level of oxidation in the immediate area. In a generalized diagram of $D^{sulfide/melt}$ for Cu, Ag, and Au (figure 27) decreasing fO_2 and increasing fS_2 equates to higher D's.

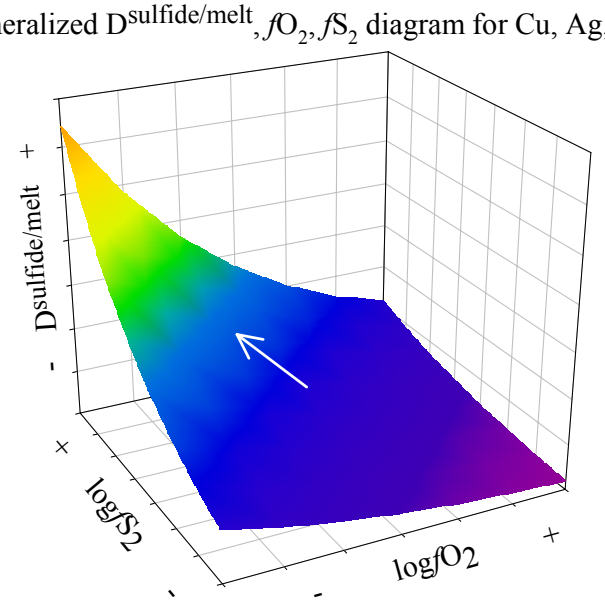

Figure 27 Generalized plot of $D^{sulfide/melt}$, fS_2, and fO_2.

Generalized form of the equilibria presented for $D^{sulfide/melt}$ for Cu, Ag, Au, and Mo. Moving the system in the direction of increasing fS_2 and decreasing fO_2 results in potentially higher D's.

Increased sulfide in the melt would also support a high fraction of sulfide minerals or immiscible melts. This period of high production at a time of more effective partitioning could lead to substantially greater sequestration of metals in pockets of cumulate sulfides. $D^{sulfide/melt}$ for each element can be calculated based on the equilibrium constants and equilibria in this study for conditions one log unit lower fO_2 and higher fS_2 (table 14) than the experimental conditions.

Table 14 Calculated $D^{po/melt}$ and $D^{Fe\text{-}S\text{-}O/melt}$ at higher fS_2 and lower fO_2

	$\log fS_2$~ -1, $\log fO_2$~ -10 bar		$\log fS_2$= 0, $\log fO_2$= -11 bar	
	$D^{po/melt}$	$D^{Fe\text{-}S\text{-}O/melt}$	$D^{po/melt}$	$D^{Fe\text{-}S\text{-}O/melt}$
Cu	>200	>200	>500	>600
Ag	58	120	150	350
Au	120	300	300	900
Mo	35	90	70	150
W	0.0012	9	0.1	9*

* Expected to remain unchanged based on statement of equilibrium
Calculations based on 1040°C, and 0.1MPa

The results of modeling of an ilmenite series granitic magma containing po or Fe-S-O melt with up to 0.2 wt. % additional sulfide can be seen in figure 28.

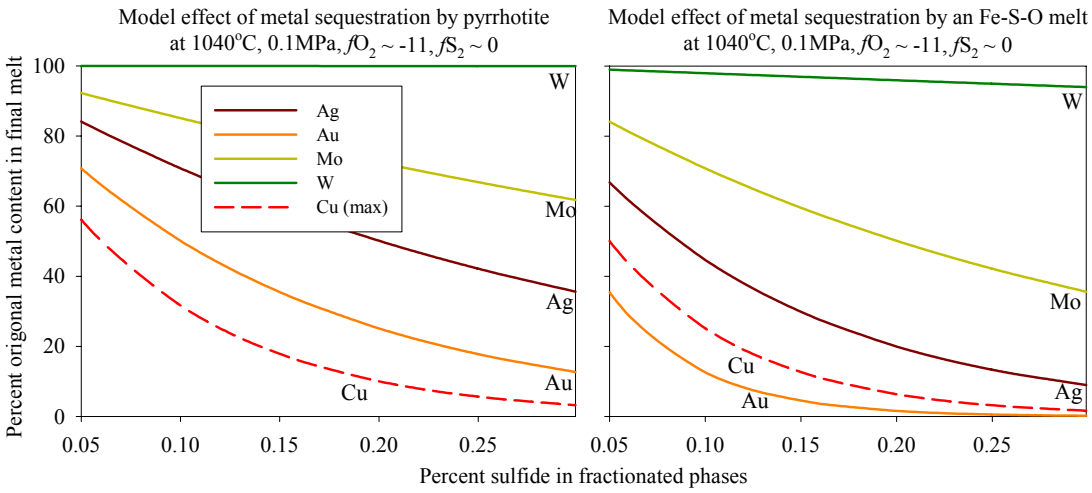

Figure 28 Effect of sequestration on metal budgets in ilmenite-series granites

Magmas that have assimilated reduced sulfur and reached a lower level of oxidation, as ilmentite-series granites are thought to, may have higher partition coefficients (Table 14) and a greater fraction of sulfur. Melt fraction equals 0.1. Under these conditions, a larger percentage of the starting metal would be sequestered and a more depleted melt would result. This may be the effect responsible for the low yields of reduced porphyry-copper deposits.

This additional sequestration of metals in ilmenite-series granites should result in unusually depleted magmas. These magmas may undergo the MVP scavenging and separation leading to hydrothermal deposits, they may contain less metal. Rowins (2000) reports on the association of reduced porphyry Cu (Au) deposits with reduced I-type granitic, mainly ilm-bearing source intrusions. These deposits are typified by lower Cu (Au) yields and are produced from volatile fluids below the FMQ fO_2 buffer. On a large scale, the division between dominantly Ilm series granites in the NW Pacific Rim and mt series in the NE pacific rim correlates to largely Sn-W deposits and sulfide-forming metals respectively (Ishihara 1998). This is consistent

with figure 28, where W abundance would not be adversely affected by the removal of even relatively large amounts of sulfides.

Although modeling single elements may help to rule out areas for exploration, the ability to explain differences in the amounts of ore metal in a single area may be of greater value. While the costs of exploration and mining of metal may slowly decrease over time, the price of each metal is in constant flux. This means profitability of a site may depend on which metal is in the highest proportion, and that this will change through time. Once the ore is mined, the cost has been incurred, so it is important to have accurate predictions of potential yields that can be based on field data and analyses. This is why studying multiple metals can reveal differential sequestering which may shed light on why deposits contain economically viable amounts of one metal, but only small amounts of another. Modeling just the effect of the iron sulfides, fractional crystallization of Mo and Cu would allow ~80% of the Mo progress to shallower magmas while as little as ~60% of the Cu could. Models of differential fractionation built on the partition coefficients determined in this study could help in predicting the relative amounts of metals in a given area.

7 Conclusions

The experimental and analytical methods in the study have been shown to be capable of supporting the goals of this project which included the creation of immiscible sulfide melts under known temperature and oxygen and sulfur fugacities, the determination of partition and equilibrium coefficients, and modeling the effects of sequestration of Fe-S-O melts on ore metals. Sealed silica tube experiments can be used at high temperatures to create and study immiscible iron sulfide melts successfully, and the potential has been shown for extending this to high water partial pressure and total pressure systems. The partition coefficients determined were in many cases in line with published values. In the limited system studied here, with the restrictions the coexistence of mt and po place on oxygen and sulfur fugacity, as they would in a magnetite-series granite, the effect of fO_2 on partition coefficients is expected to be small in the range QFM-1to NNO+1 for most of the elements studied. Sulfide separation, and in particular Fe-S-O melt separation is predicted to have a large effect on the total metal budget of crystallizing magmas and on the relative proportions of individual elements. The data suggest that this effect could be greater in ilmenite-series granites. Logical extensions of this study into different pressure and temperature regimes, as well as different compositions of silicate melt and Fe-S-O melt will improve the ability to predict of the role sulfides and sulfide melts play in arc magma metal budgets.

Appendices

Appendix A Standards used in WDS

Table 15 Appendix A Standards used in WDS

Element	WDS Standards: Pyrrhotite & Fe-S-O Melt	Glass Trace	Glass Majors
Ag	Ag (Metal)	NBS-610	
Al		*	Yellowstone Rhyolite
Au	Au (Metal)		
Ca			Hornblende
Cl		Scapolite	Scapolite
Cu	Chalcopyrite	NBS-610	
Fe	Santa Eulalia Pyrrhotite	Magnetite	Kakanui Hornblende
K			Yellowstone Rhyolite
Mn	Mn (Metal)	NBS-610	Rhodonite
Na		*	Yellowstone Rhyolite
S	Santa Eulalia Pyrrhotite	Scapolite	Scapolite
Si	Rhodonite	*	Yellowstone Rhyolite
Zn	Zn (Metal)	NBS-610	

* Elements were monitored to evaluate the presence of common inclusions (silicates, sulfides, etc.) within the analytical volume

Appendix B Concentrations from the high-pressure experiment

Table 16 Appendix B Concentrations from the high-pressure experiment

Run #30 200 Minutes		Pyrrhotite	$1\sigma_{\bar{X}}$	Fe-S-O	$1\sigma_{\bar{X}}$	Glass	$1\sigma_{\bar{X}}$		Glass Oxide wt %	$1\sigma_{\bar{X}}$
Si	ppm	<30	-	1300	*100*			SiO_2	72.0	*0.1*
S	%	37.4	*0.2*	29.4	*0.5*			Al_2O	9.5	*0.1*
Mn	ppm	115	*6*	115	*6*	280	*20*	$FeO_{(t}$	8.5	*0.2*
Fe	%	60.7	*0.1*	60.2	*0.7*	6.6	*0.1*	MnO	0.017	*0.002*
Cu	ppm	960	*50*	1400	*80*			CaO	2.48	*0.07*
Ag	ppm	2000	*100*	2800	*700*	20	*10*	Na_2O	1.88	*0.01*
Au	ppm	690	*40*	1700	*400*			K_2O	0.66	*0.03*
								ASI	1.10	

< indicates that the value is below detection
$FeO_{(t)}$ = Total Fe as FeO
* = $Al_2O_3/(Na_2O+ K_2O+CaO)$ Molar

Appendix C Concentrations from WDS analysis of mt

Table 17 Appendix C Concentrations from WDS analysis of mt

Magnetite		20 Minutes				200 Minutes				2000 Minutes			
		17a	$1\sigma_{\bar{X}}$	17b	$1\sigma_{\bar{X}}$	16a	$1\sigma_{\bar{X}}$	16b	$1\sigma_{\bar{X}}$	18a	$1\sigma_{\bar{X}}$	18a	$1\sigma_{\bar{X}}$
Mn	ppm	630	*40*	690	*30*	650	*8*	750	*30*	767	*4*	932	*8*
Ti	%	0.44	*0.02*	0.45	*0.04*	0.8	*0.1*	0.51	*0.06*	1.1	*0.1*	0.62	*0.04*
Mo	%	-	-	-	-	-	-	-	-	0.190	*0.004*	0.21	*0.03*
W	ppm	-	-	-	-	-	-	-	-	100	*20*	140	*20*

% = Weight %

Appendix D Plots of $D^{sulfide/melt}$ for Ti, V, and Zn

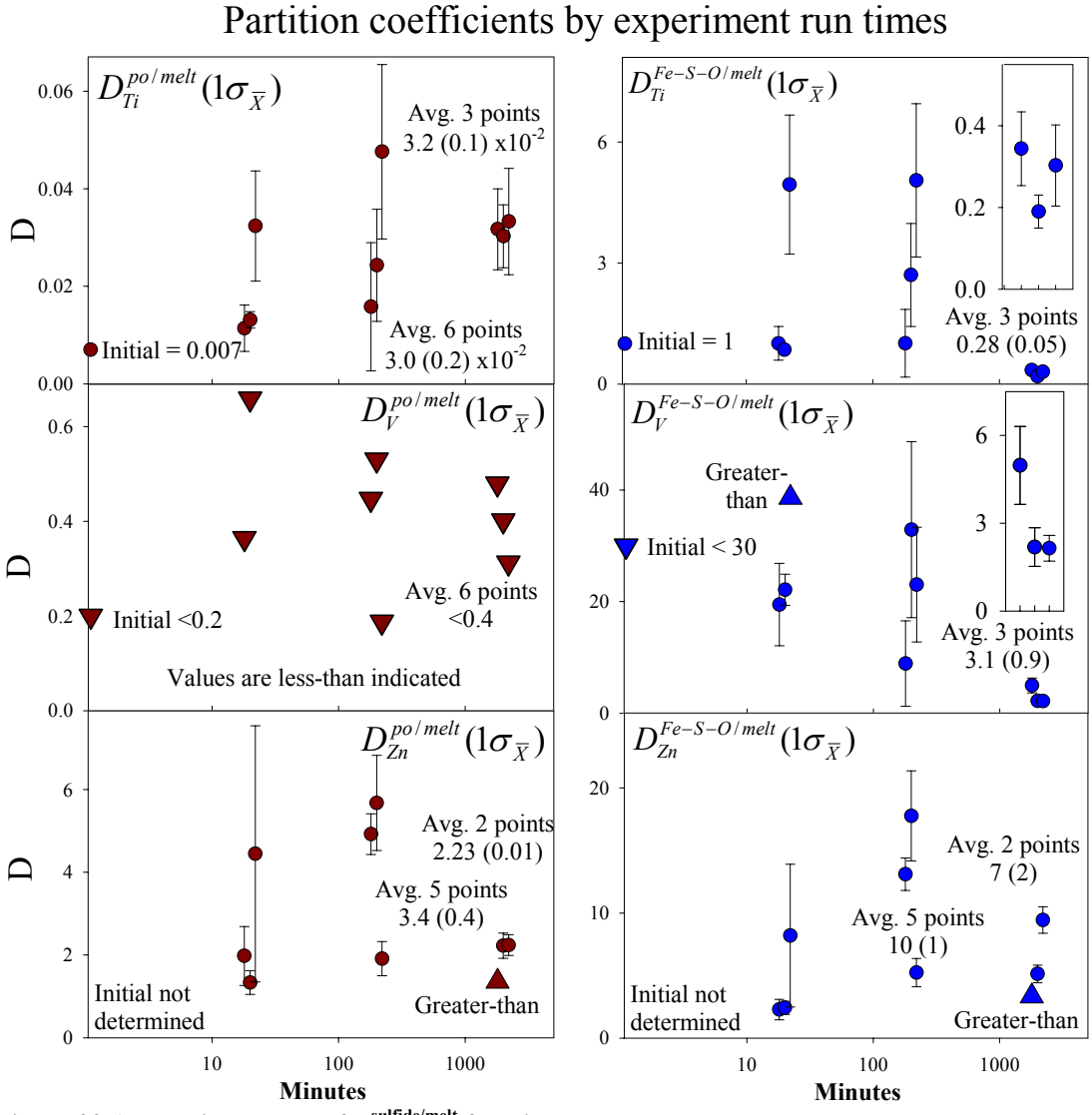

Figure 29 Appendix D Plots of $D^{sulfide/melt}$ for Ti, V, and Zn.

Appendix E Plots of $D^{sulfide/melt}$ for Th and U

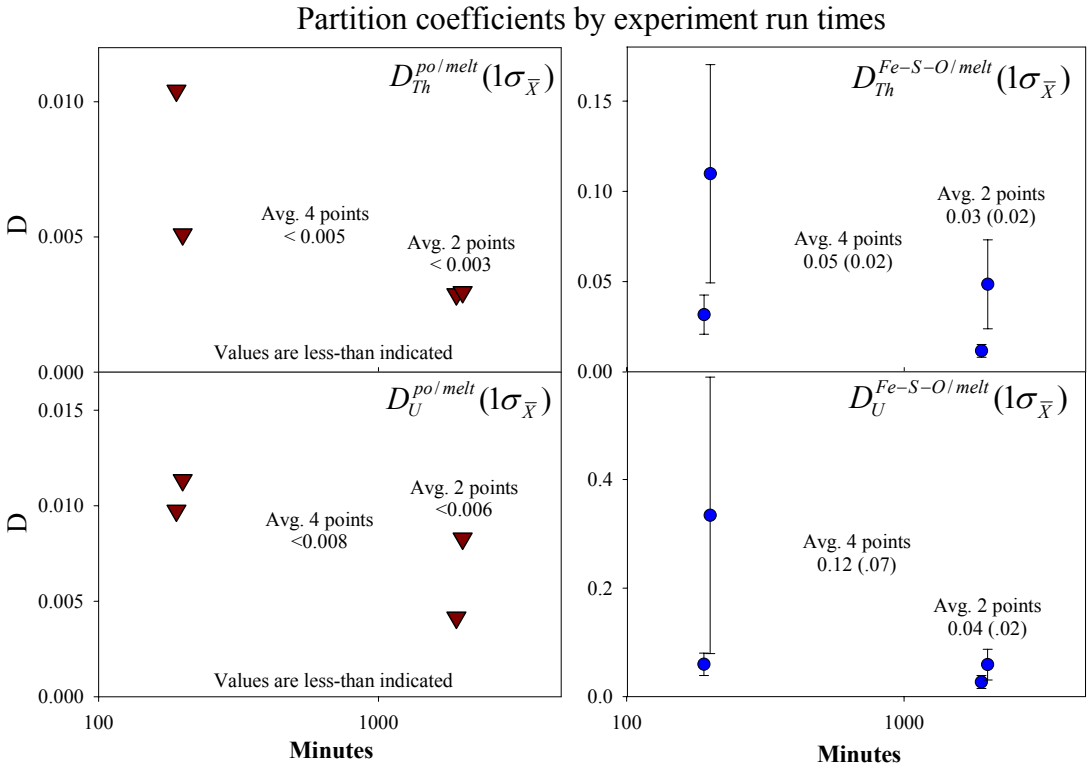

Figure 30 Appendix E Plots of $D^{sulfide/melt}$ for Th and U.

Appendix F Plots of $D^{sulfide/melt}$ for Co and Re

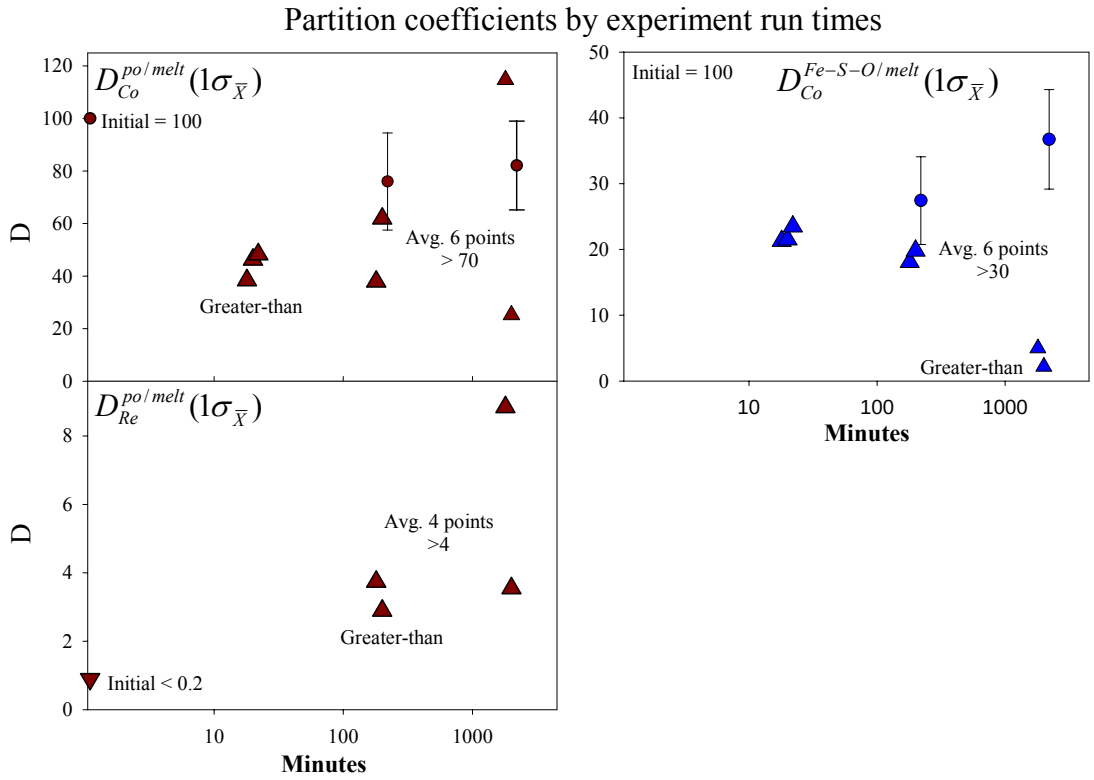

Figure 31 Appendix F Plots of $D^{sulfide/melt}$ for Co and Re.

Optical images of run products

Run 16d

Run 16e

Run 16f

-Group 6 (Mo,W) experiment
-200 minute run time
-Dark lines at left in the images are 1mm marks
-Run products are oriented approximately as they were during the experiment

Optical images of run products

Run 16d

Run 16e

Run 16f

-Additional optical images of run 16.

BSE images of run products

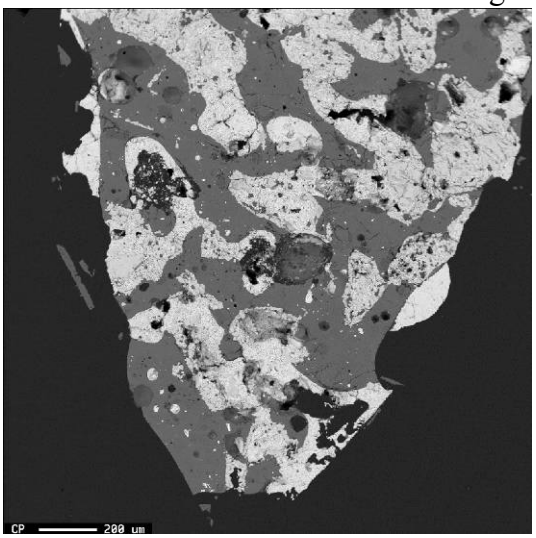

Run 16d

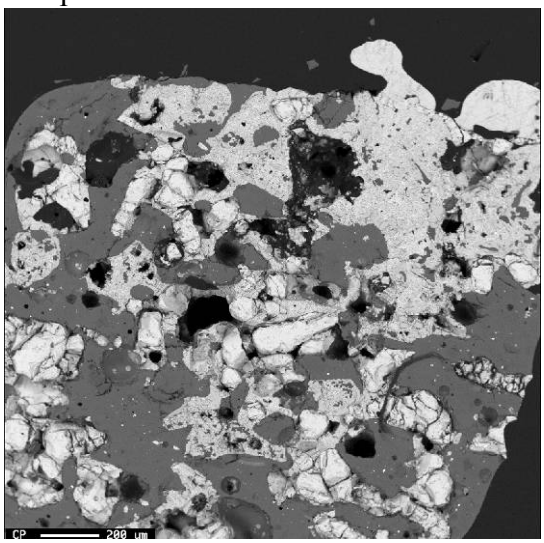

Run 16d

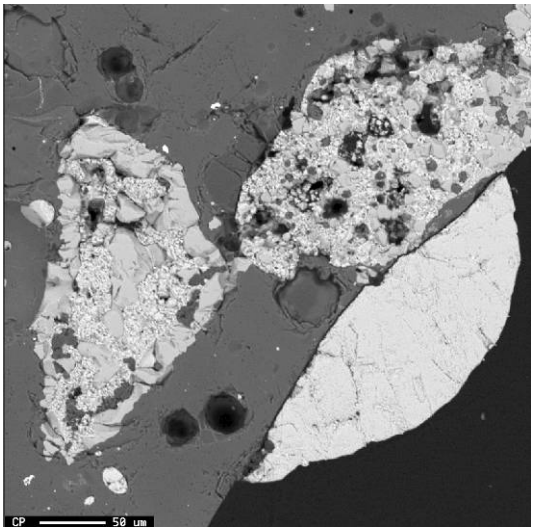

Run 16d

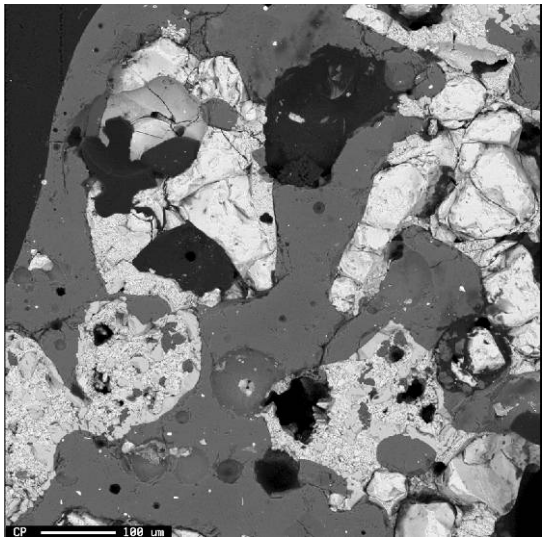

Run 16d

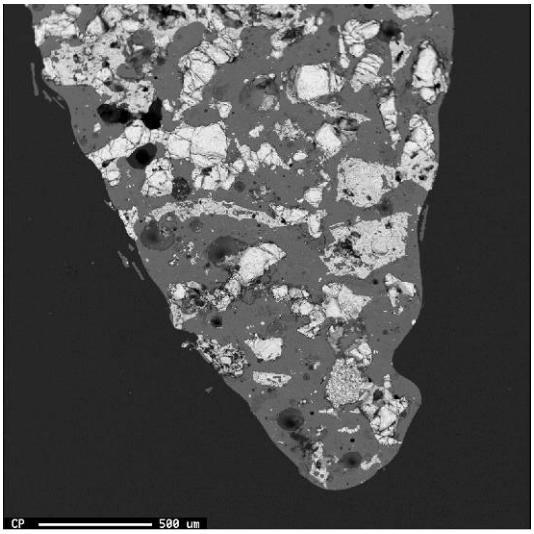

Run 16e

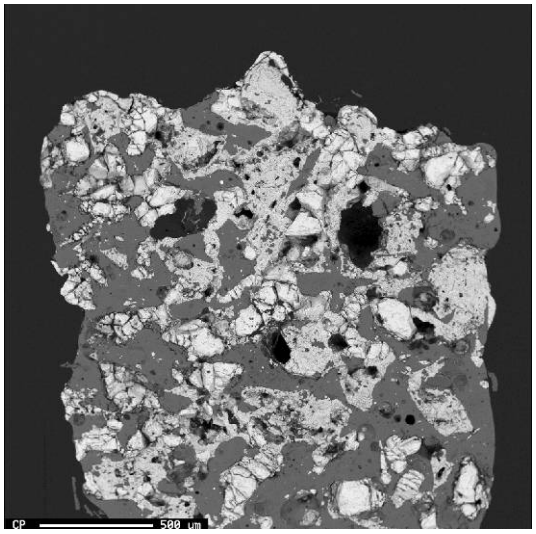

Run 16e

BSE images of run products

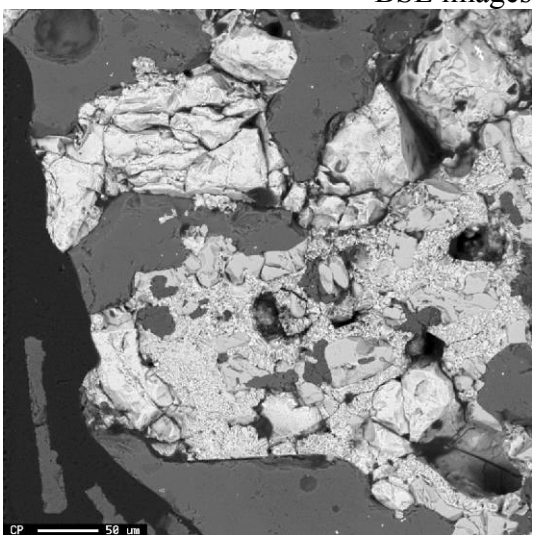

Run 16e

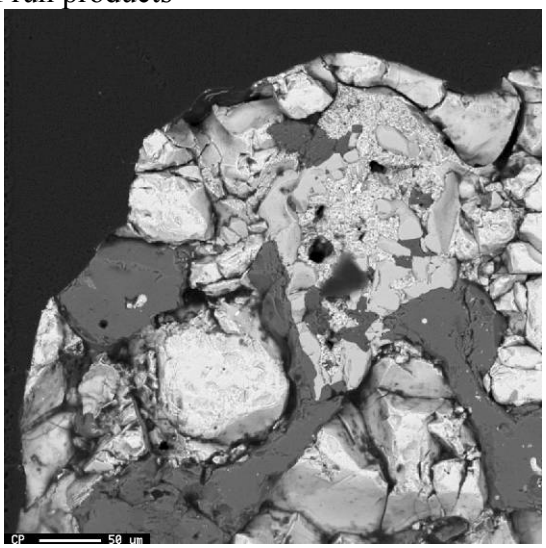

Run 16e

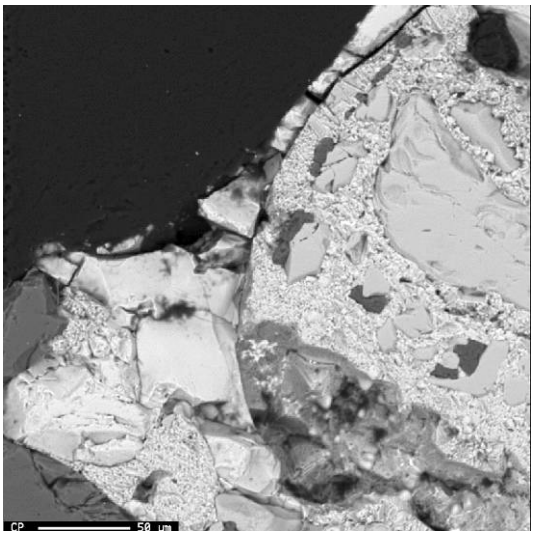

Run 16e

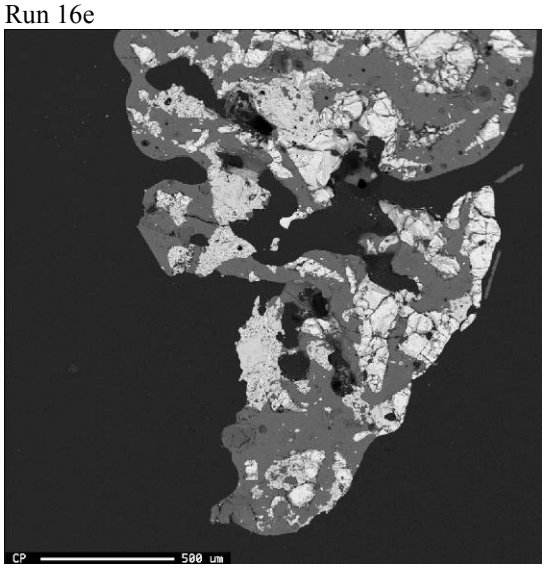

Run 16f

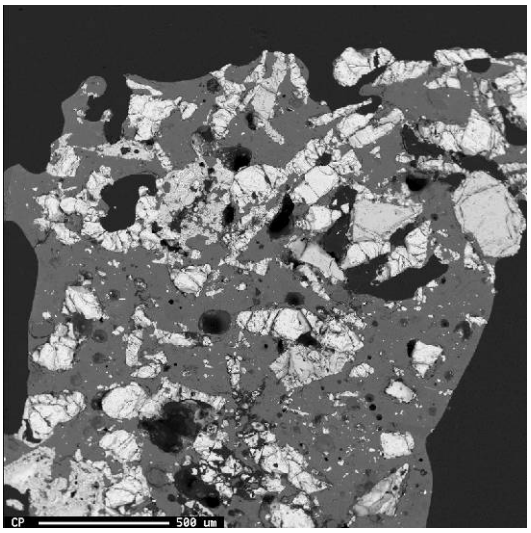

Run 16f

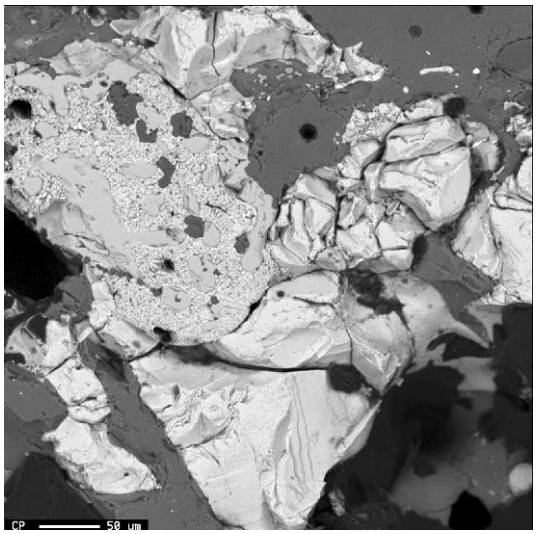

Run 16f

BSE images of run products

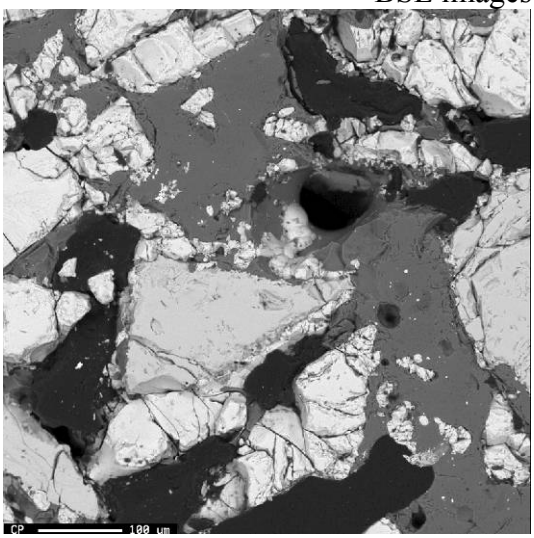

Run 16f

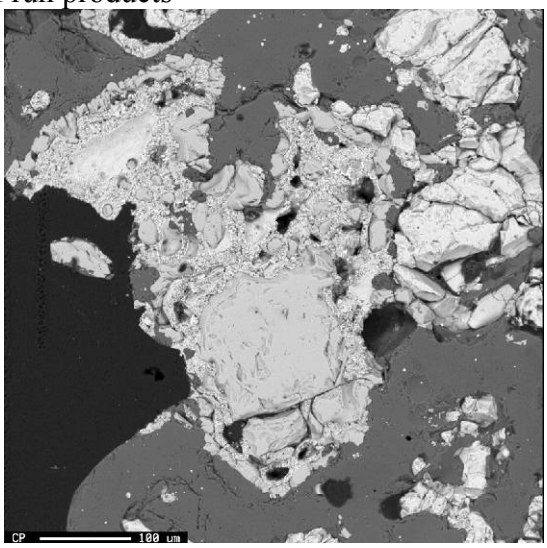

Run 16f

Optical images

Run 17a

Run 17b

Run 17c

-Group 6 (Mo,W) experiment
-20 minute run time
-Dark lines at left in the images are 1mm marks
-Run products are oriented approximately as they were during the experiment

BSE images of run products

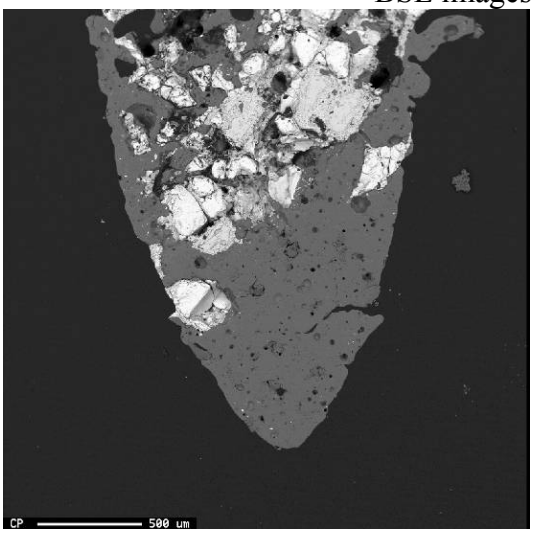

Run 17a

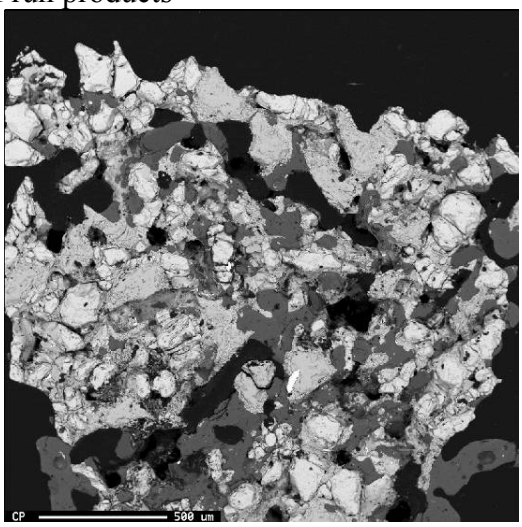

Run 17a

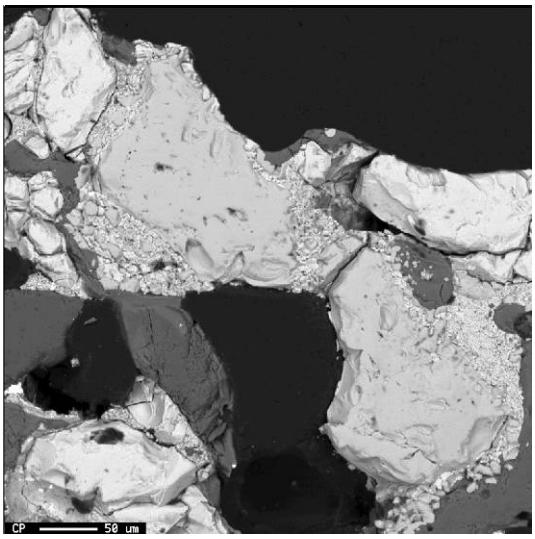

Run 17a

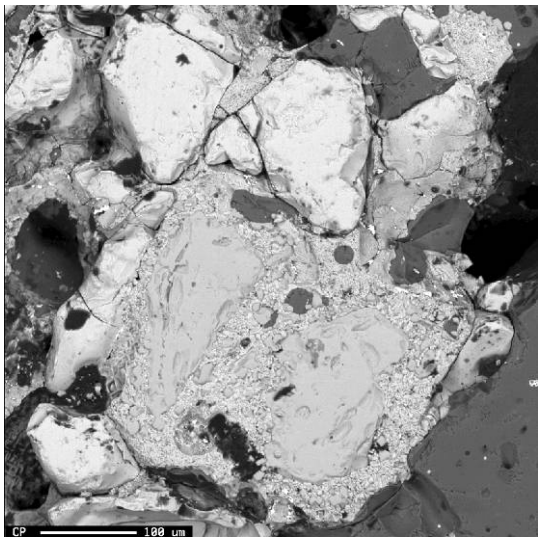

Run 17a

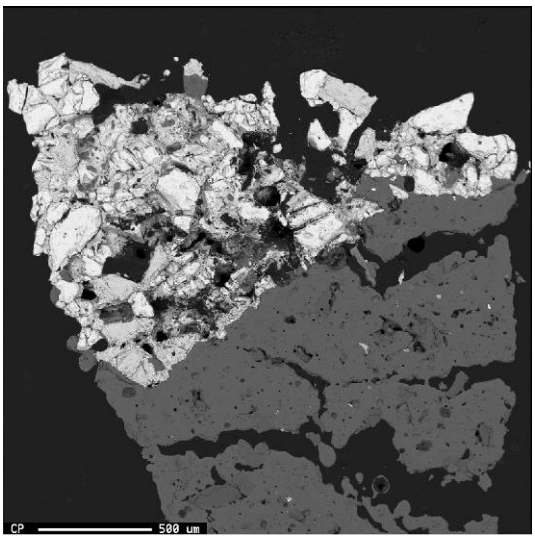

Run 17b

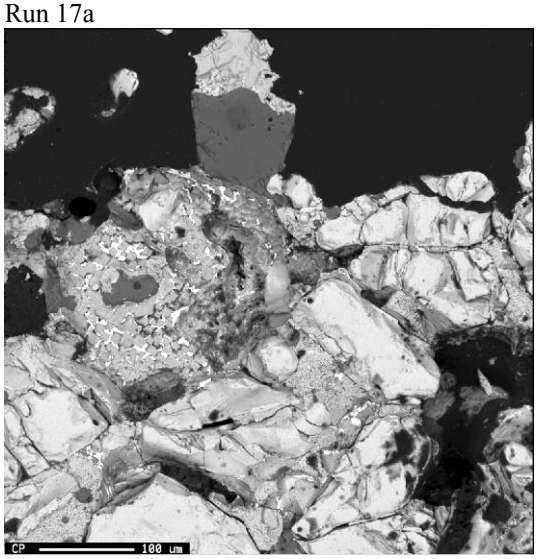

Run 17b

BSE images of run products

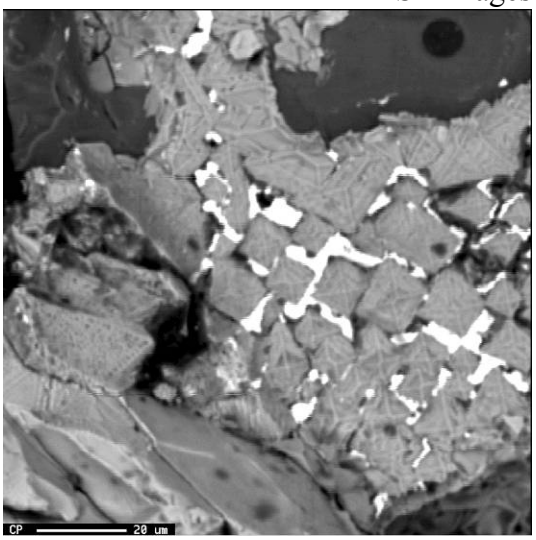

Run 17b

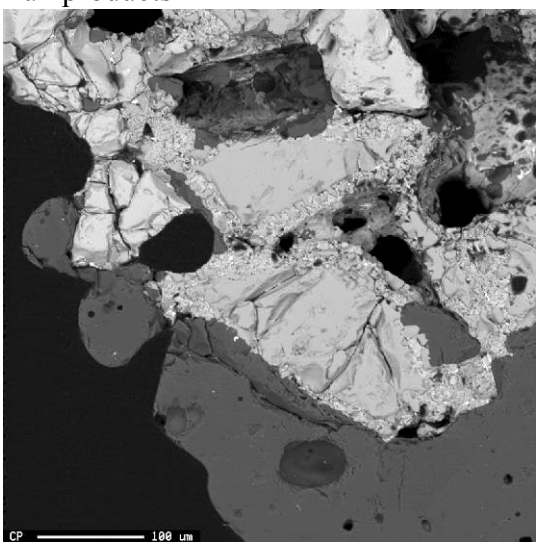

Run 17b

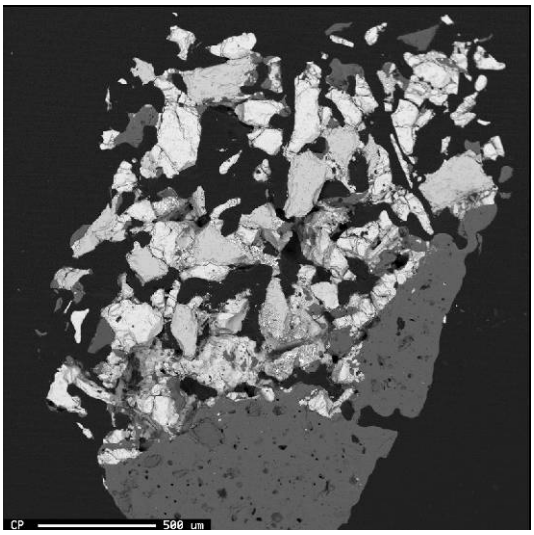

Run 17c

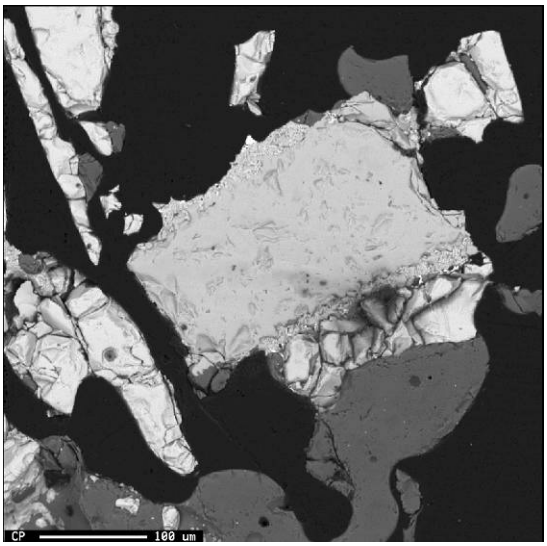

Run 17c

Optical images of run products

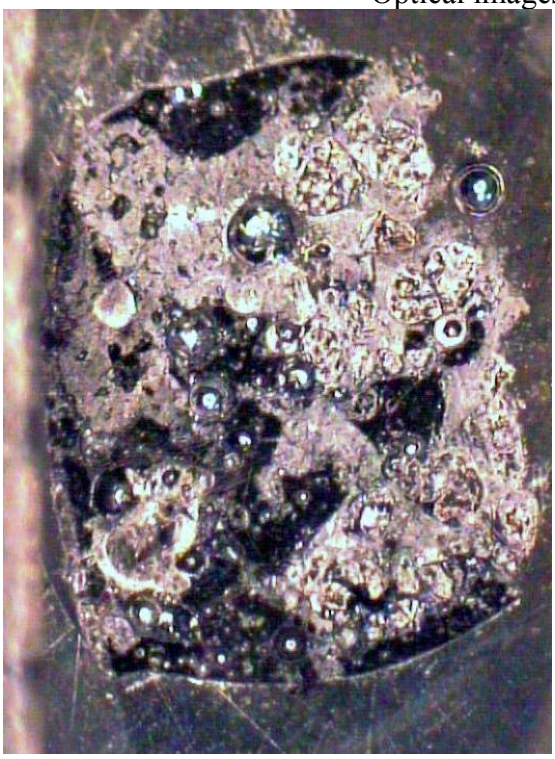

Run 18a

Run 18b

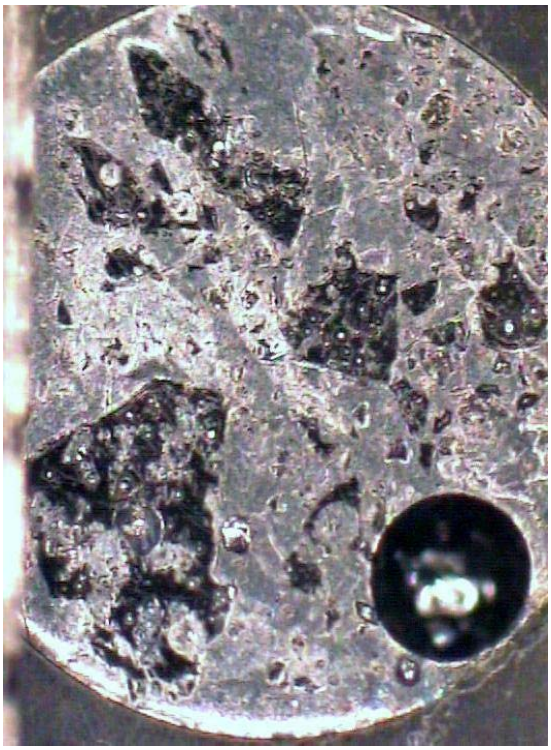

Run 18c

-Group 6 (Mo,W) experiment
-2000 minute run time
-Dark lines at left in the images are 1mm marks
-Run products are oriented approximately as they were during the experiment

BSE images of run products

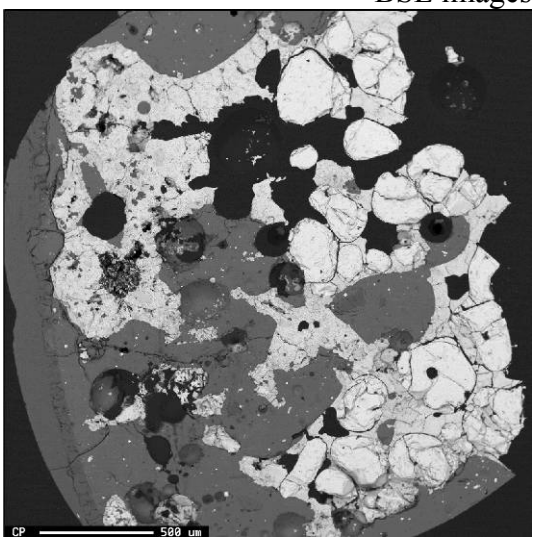

Run 18a

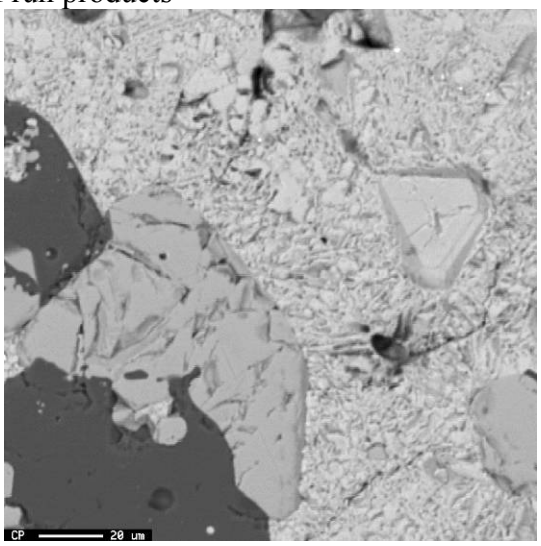

Run 18a

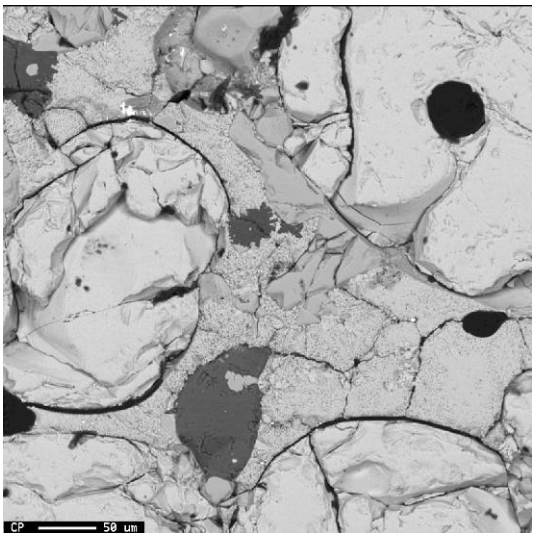

Run 18a

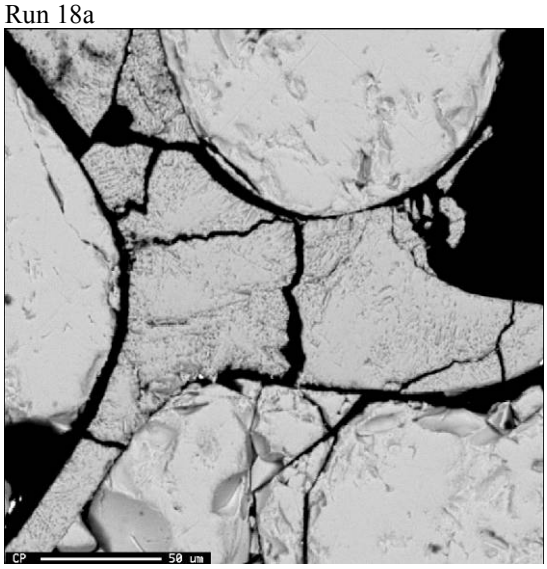

Run 18a

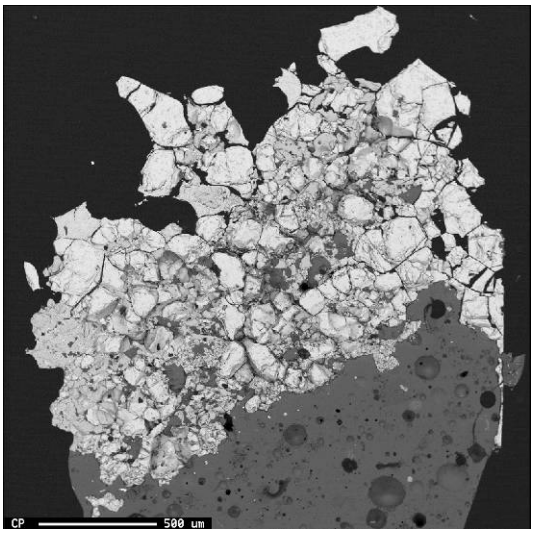

Run 18b

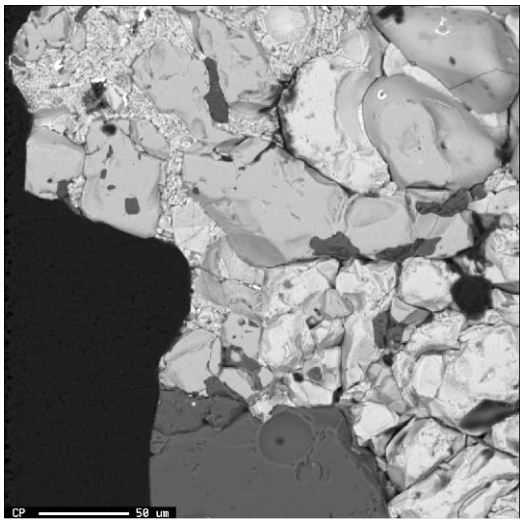

Run 18b

BSE images of run products

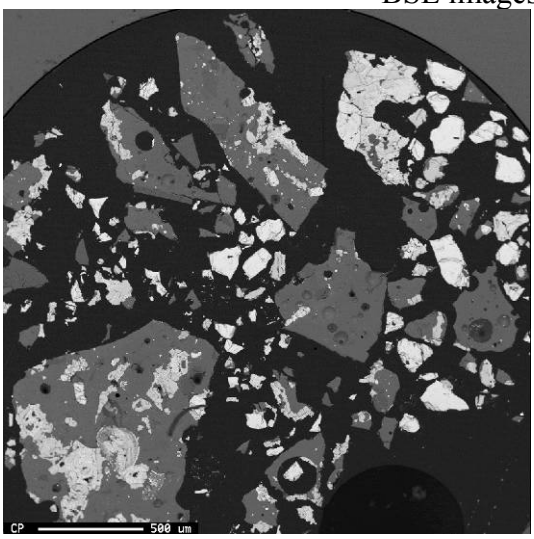

Run 18c

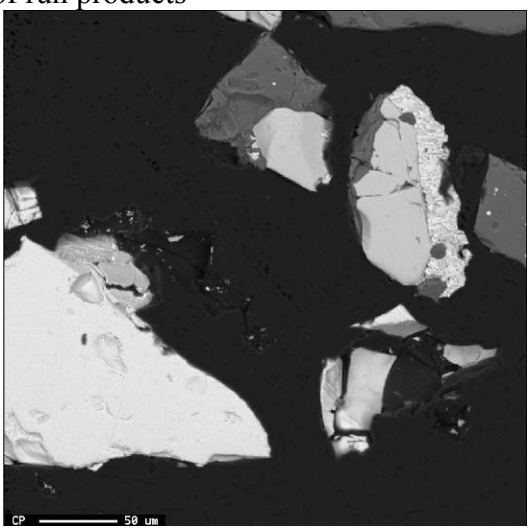

Run 18c

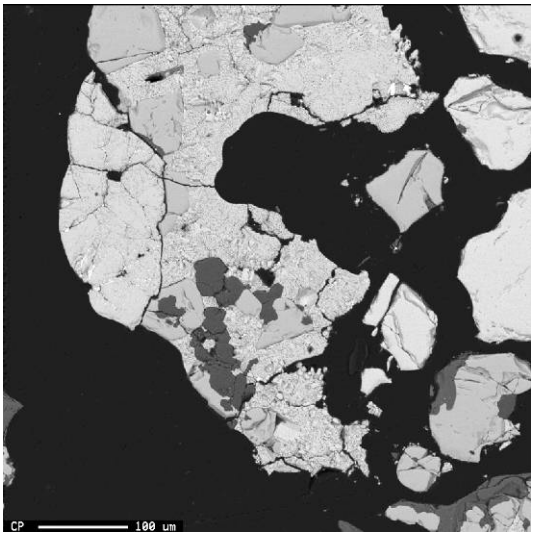

Run 18c

Optical images of run products

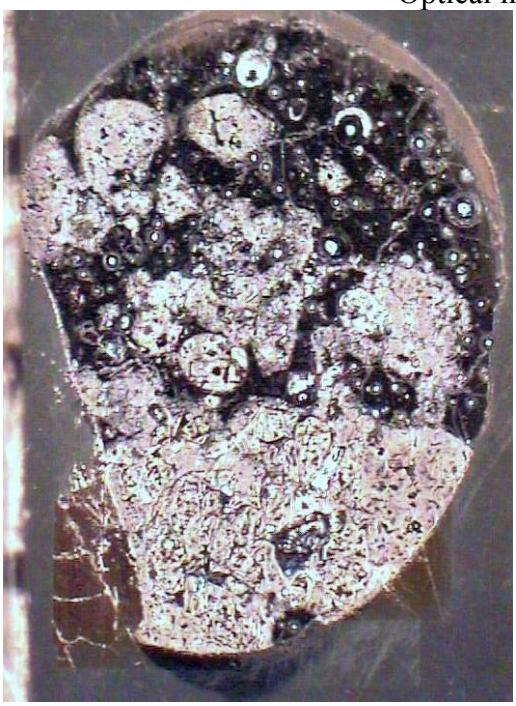

Run 20a

Run 20b

Run 20c

-Group 11 (Cu,Ag,Au) experiment
-2000 minute run time
-Dark lines at left in the images are 1mm marks
-Run products are oriented approximately as they were during the experiment

BSE images of run products

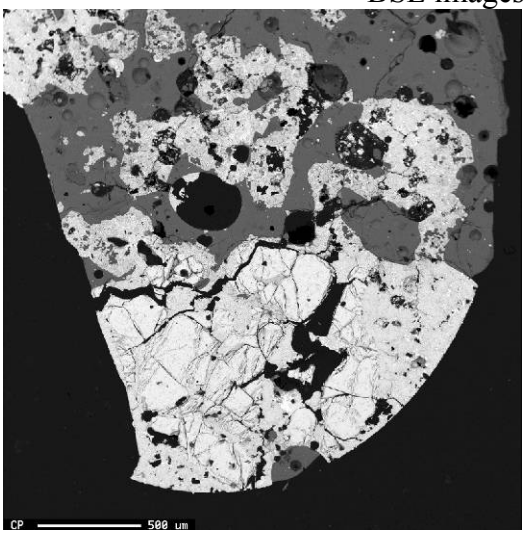

Run 20a

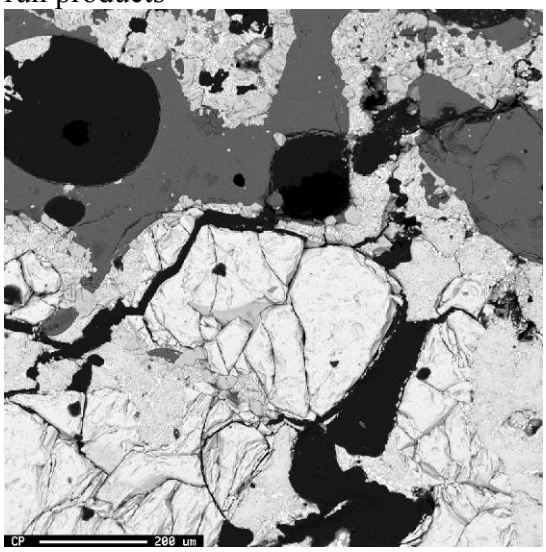

Run 20a

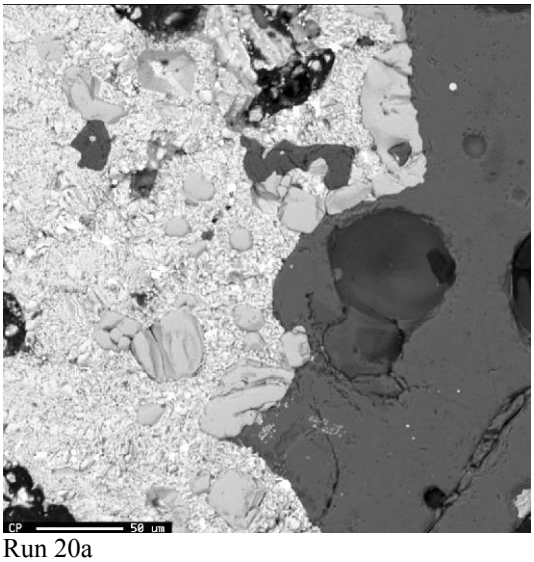

Run 20a

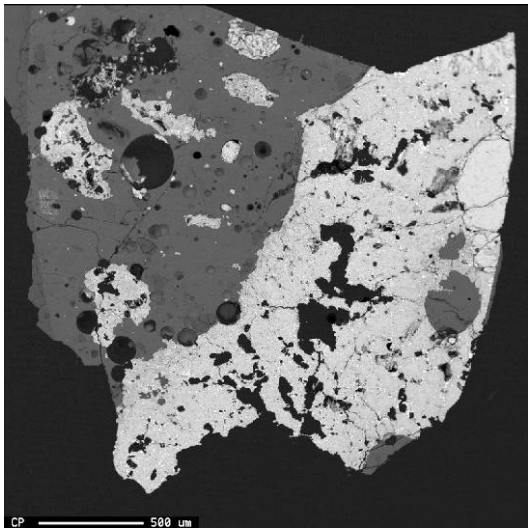

Run 20b

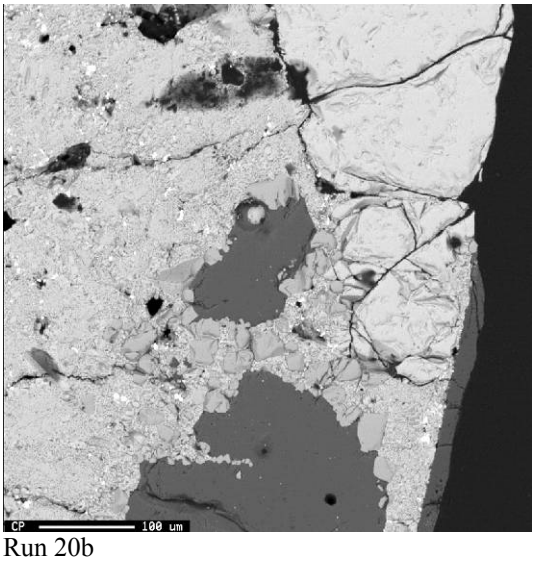

Run 20b

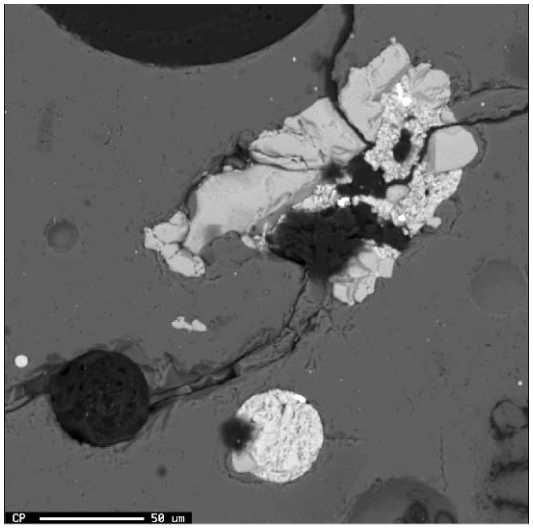

Run 20b

BSE images of run products

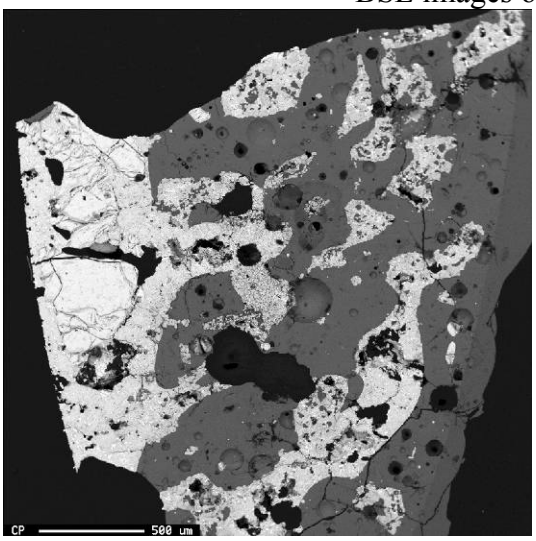

Run 20c

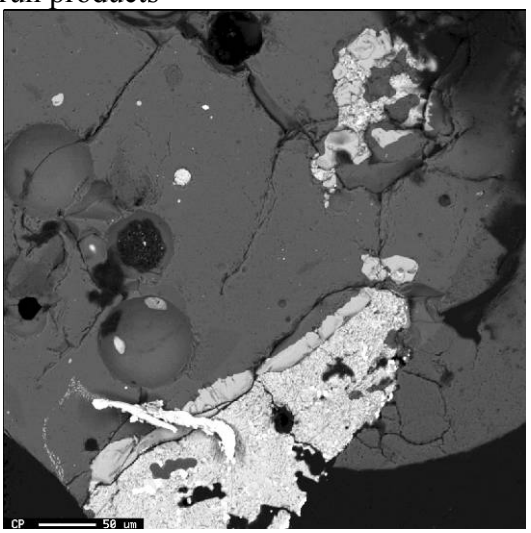

Run 20c

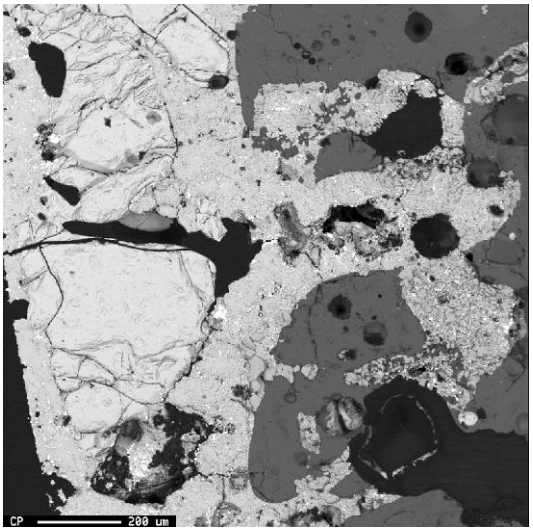

Run 20c

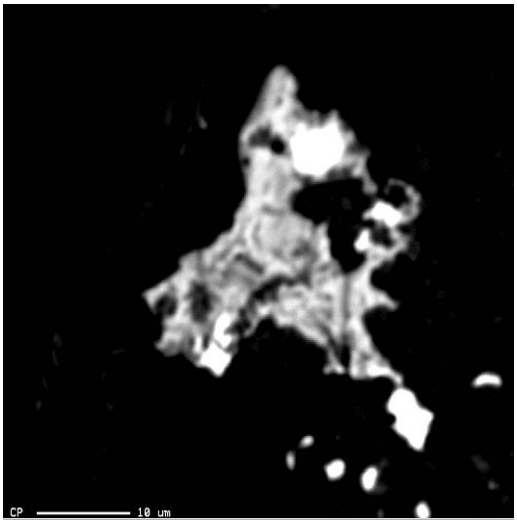

Run 20c Au+Ag (white) and Ag+S (gray) in Fe-S-O (black) by elements identified by EDS

Optical images of run products

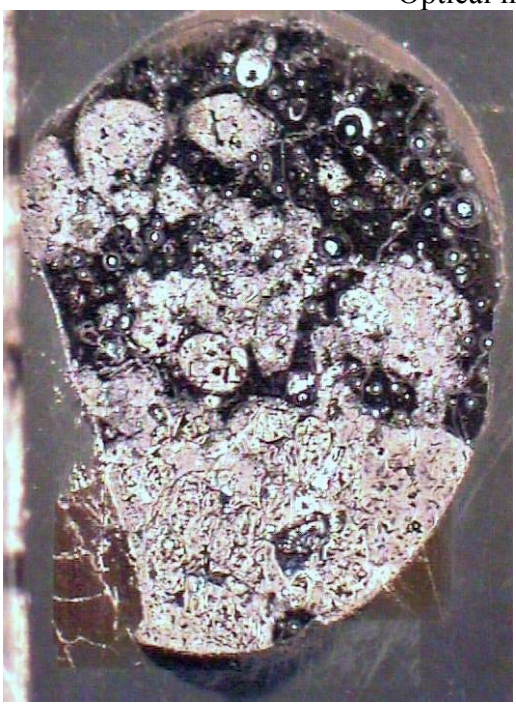

Run 21a

Run 21b

Run 21c

-Group 11 (Cu,Ag,Au) experiment
-200 minute run time
-Dark lines at left in the images are 1mm marks
-Run products are oriented approximately as they were during the experiment

BSE images of run products

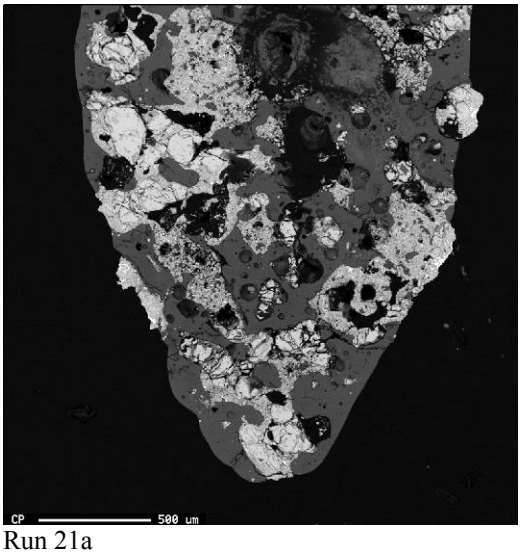

Run 21a

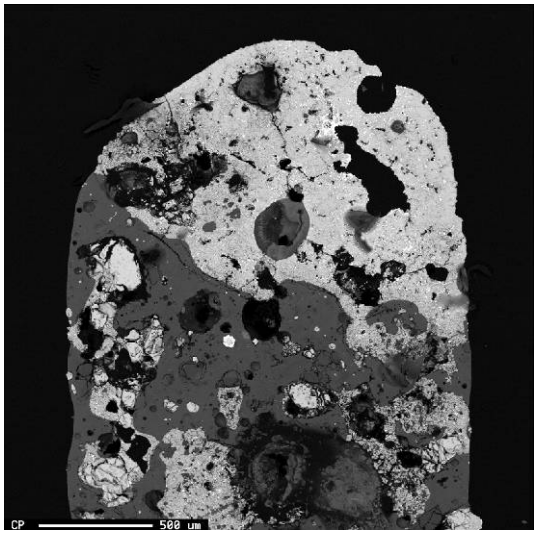

Run 21a

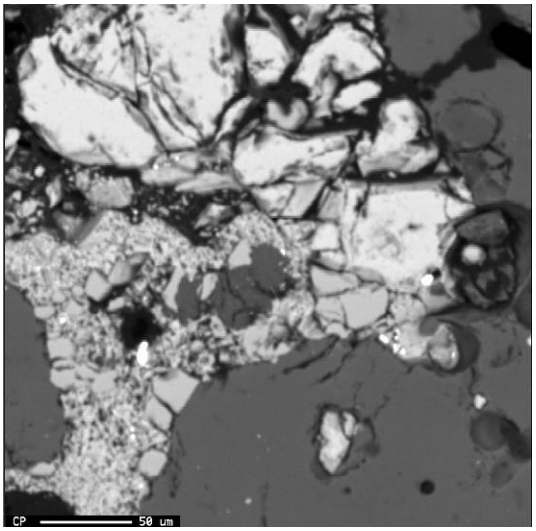

Run 21a

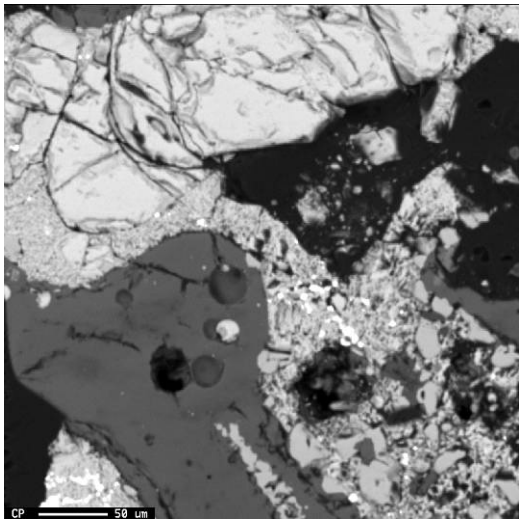

Run 21a

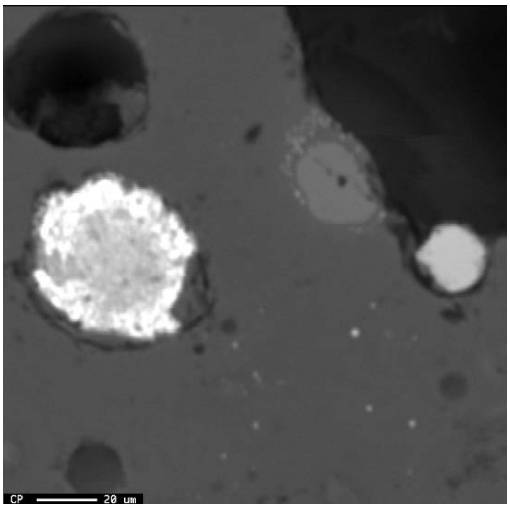

Run 21a White color is Ag+S and Ag+Au by EDS

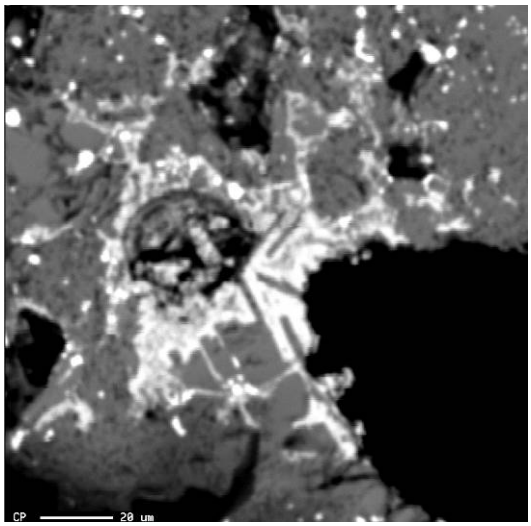

Run 21a Rare dentritic growth (Ag+S) in Fe-S-O

BSE images of run products

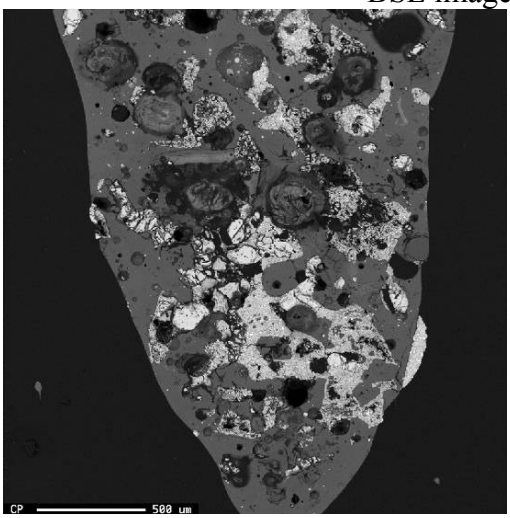

Run 21b

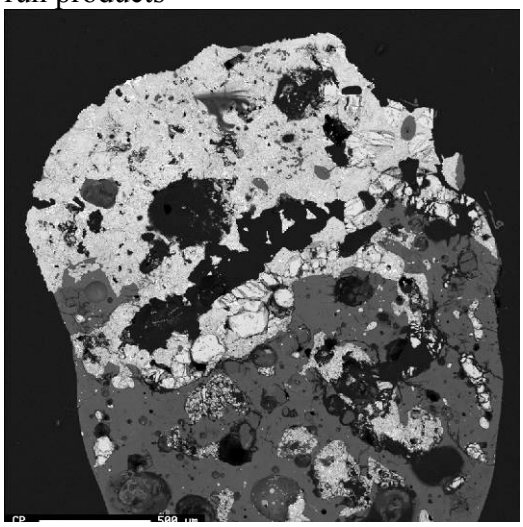

Run 21b

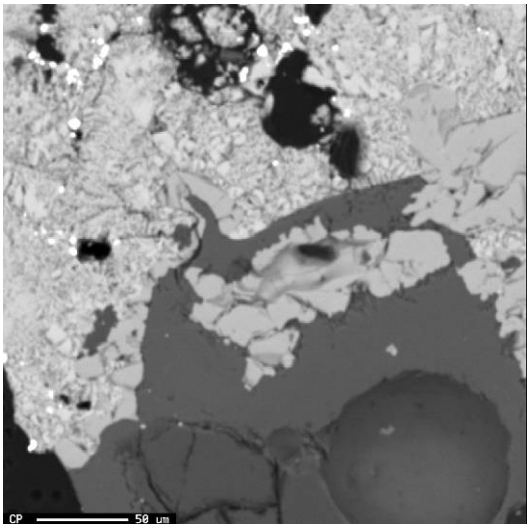

Run 21b

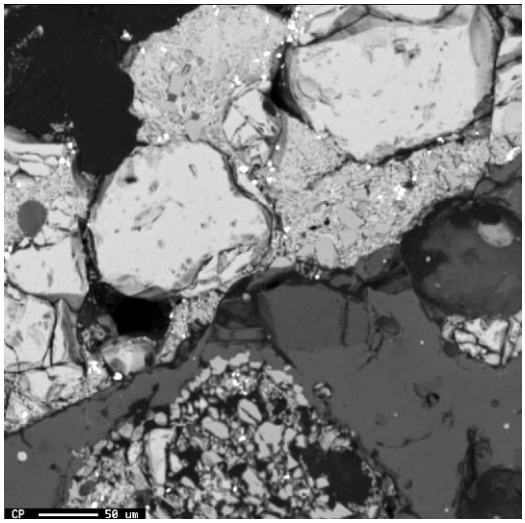

Run 21b

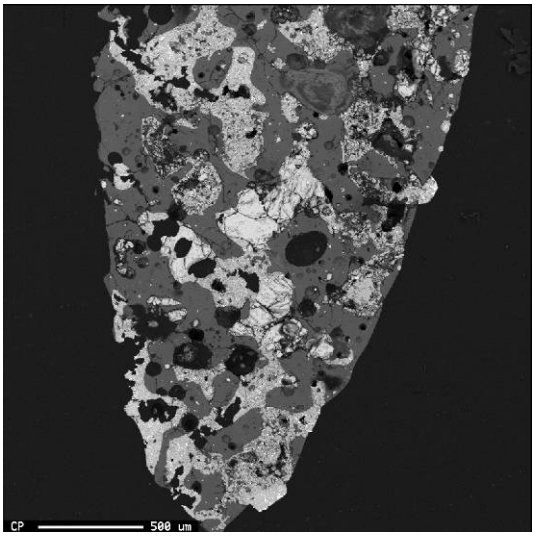

Run 21c

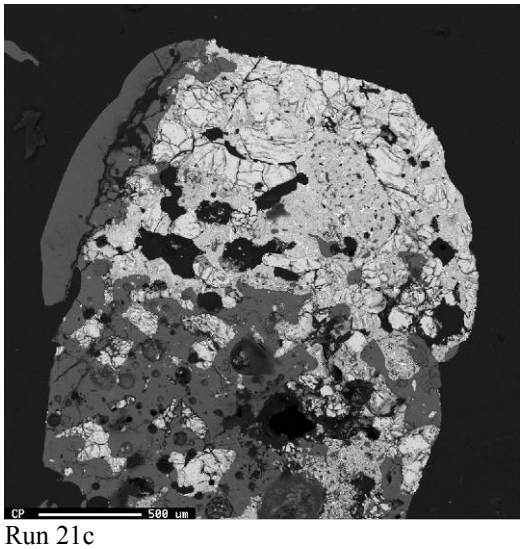

Run 21c

BSE image of run product

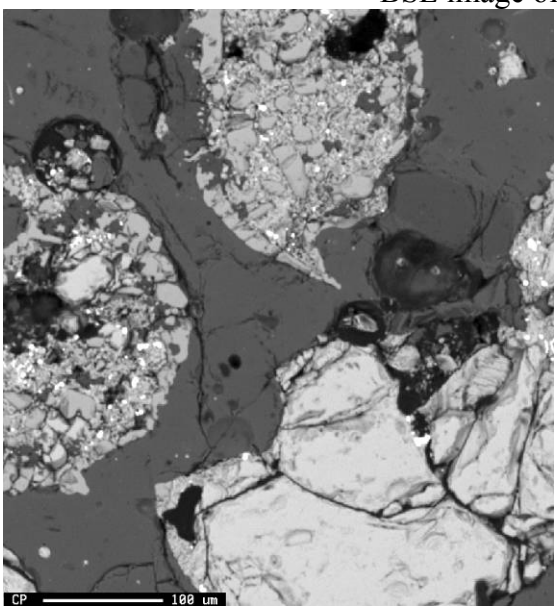

Run 21c

Optical images of run products

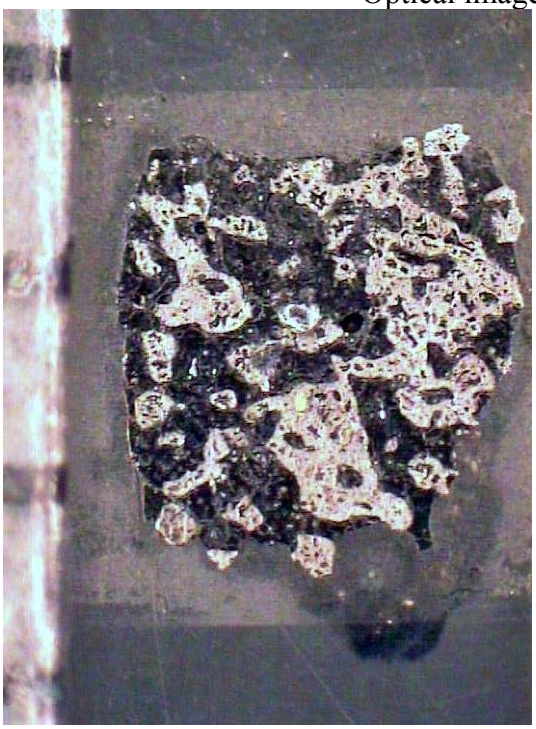

Run 22a

Run 22b

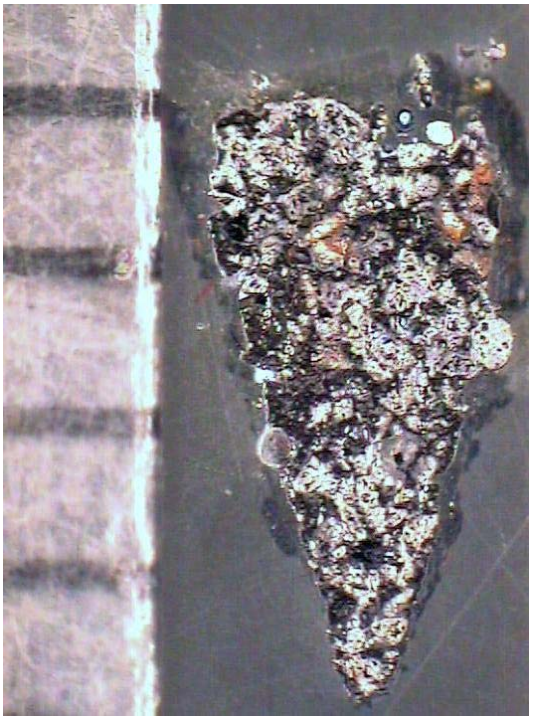

Run 22c

-Group 11 (Cu,Ag,Au) experiment
-20 minute run time
-Dark lines at left in the images are 1mm marks
-Run products are oriented approximately as they were during the experiment

BSE images of run products

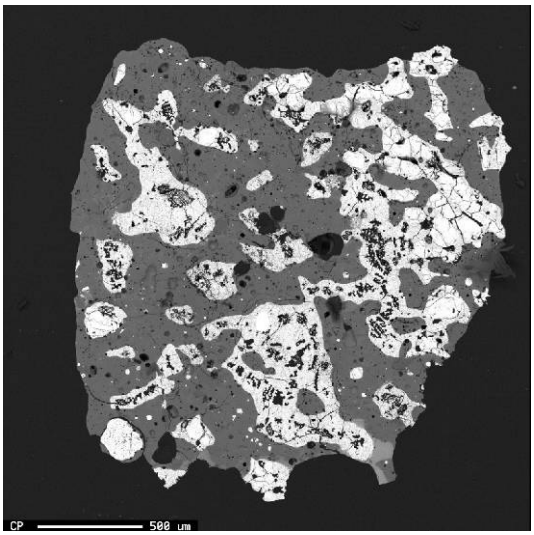

Run 22a

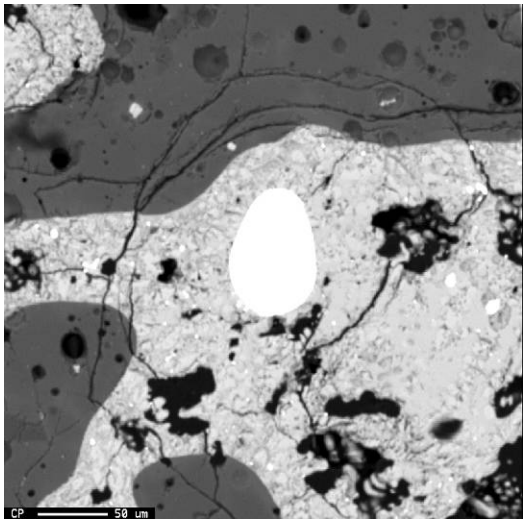

Run 22a Ag+S (white) in Fe-S-O (light gray)

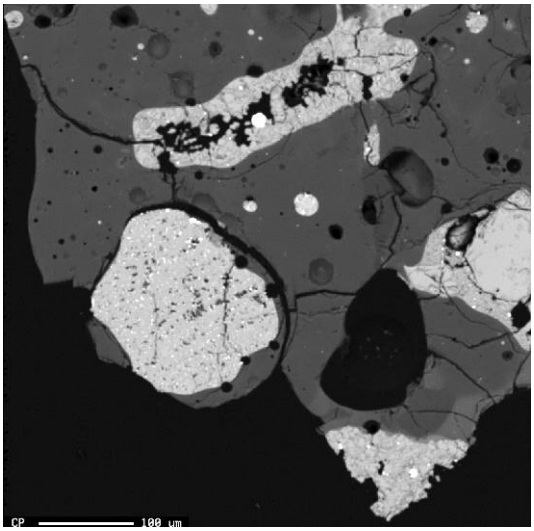

Run 22a

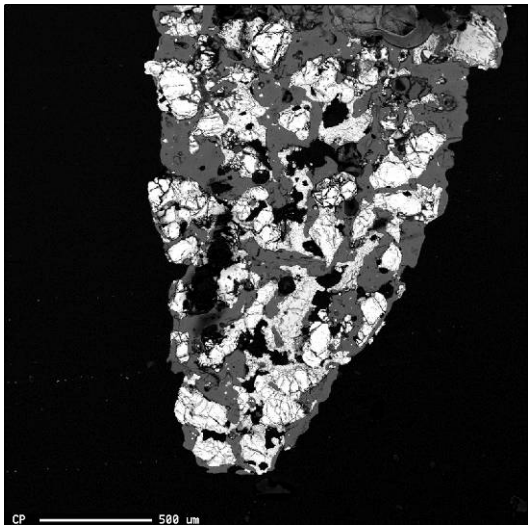

Run 22b

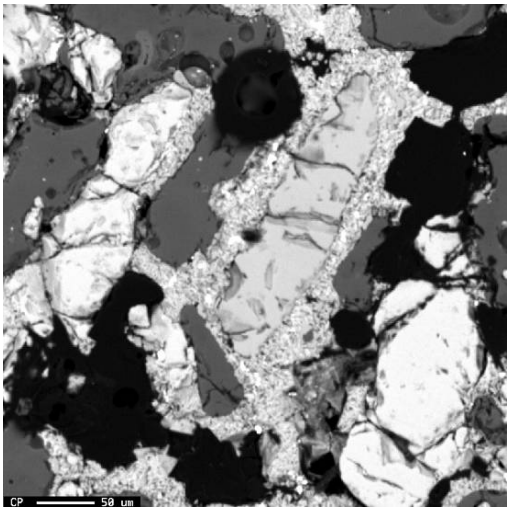

Run 22b

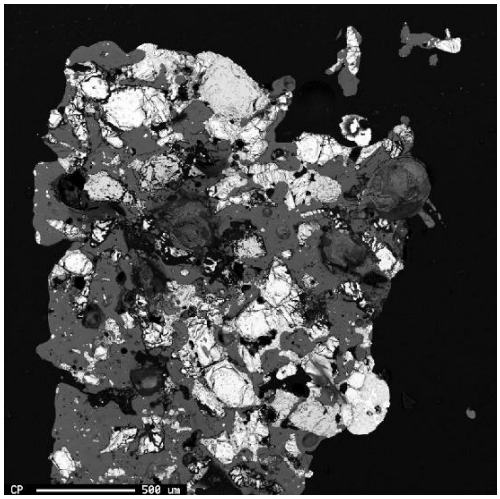

Run 22c

BSE images of run products

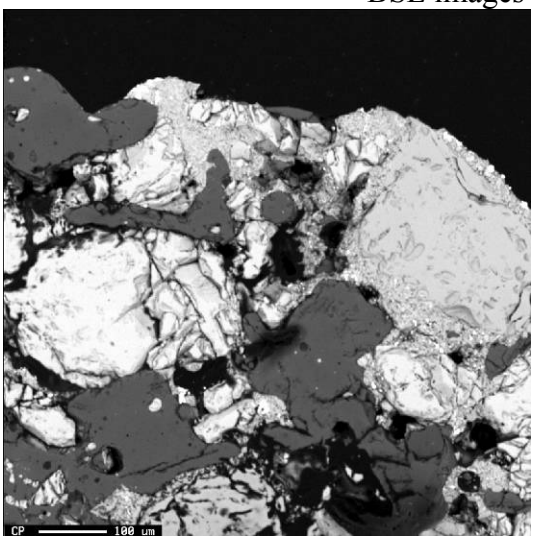

Run 22c

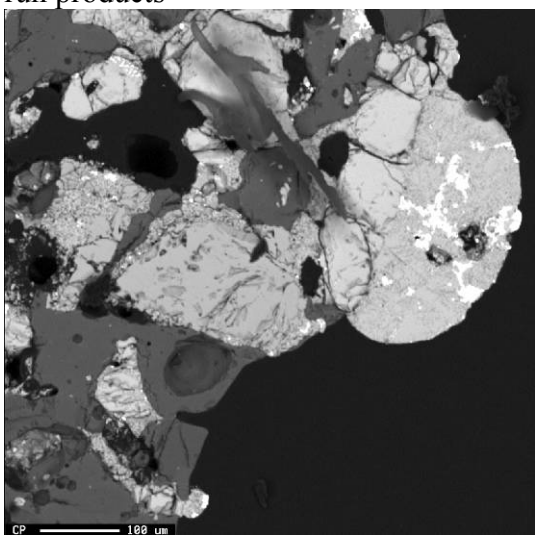

Run 22c

Optical images of run products

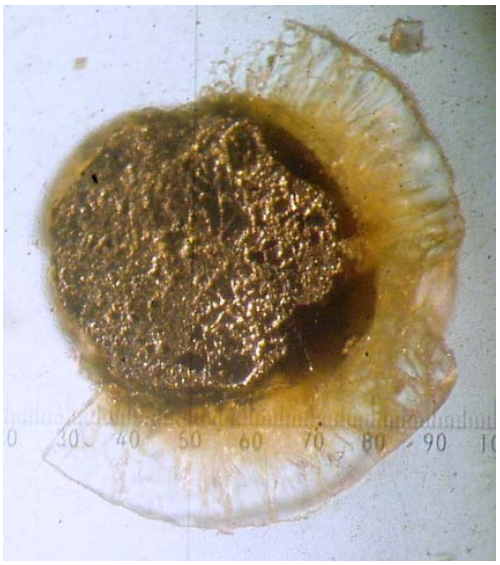

Run 30 Cross section – 100 tick marks ~ 1mm

Run 30 Optical image – 100 tick marks ~ 1mm

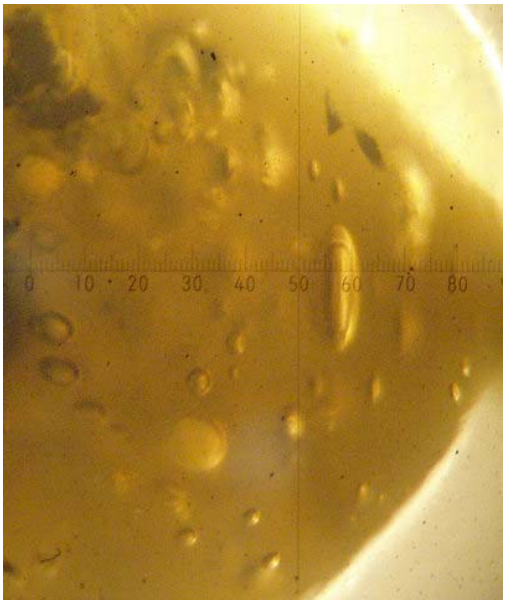

Run 30 Fluid/vapor inclusions in quenched melt
100 tick marks ~ 200μm

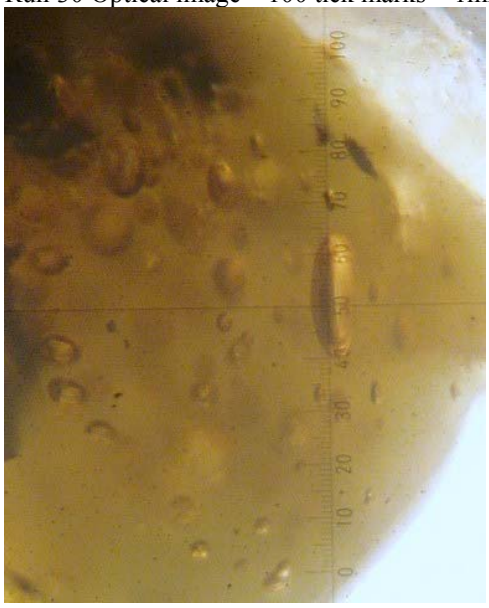

Run 30 Fluid/vapor inclusions in quenched melt
100 tick marks ~ 200μm

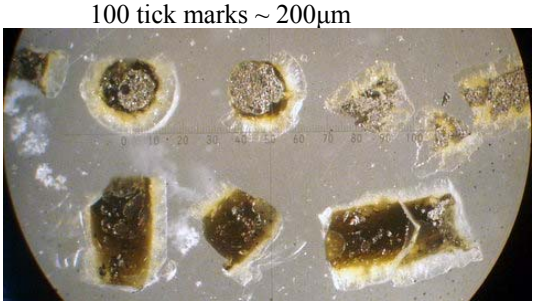

Run 30 Optical image – Field of view ~ 2mm

-High pressure run ~100MPa
-Mt. St. Helens dacite used for silicate melt
-Group 6 (Cu,Ag,Au) experiment
-200 minute run time

BSE Images of run products

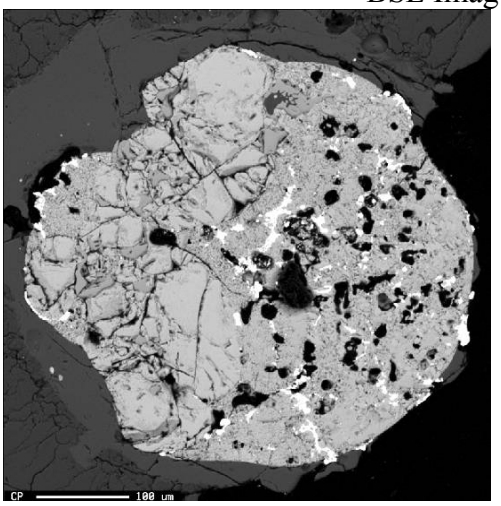

Run 30 – Cross section

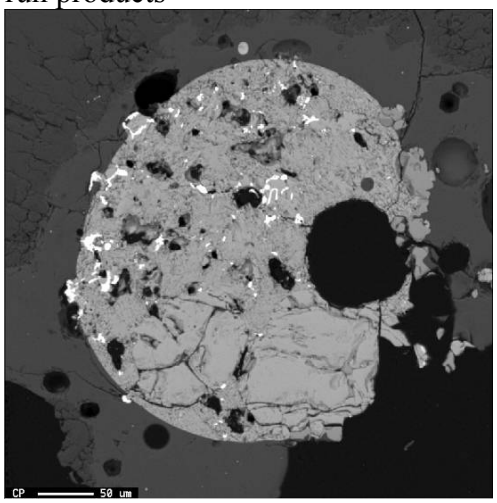

Run 30 – Cross section

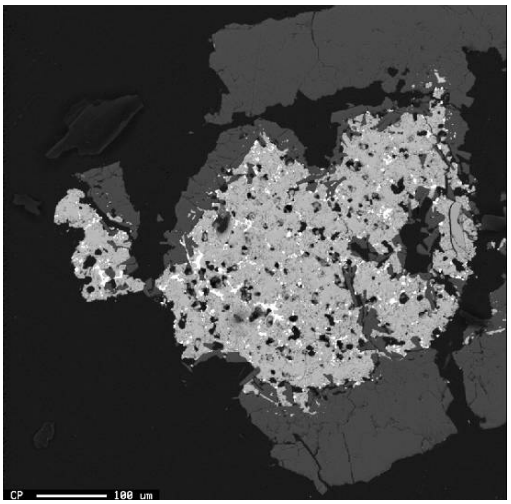

Run 30 – Lengthwise cut

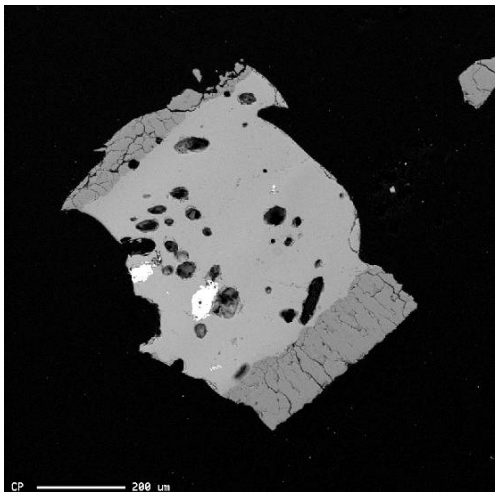

Run 30 – Lengthwise cut

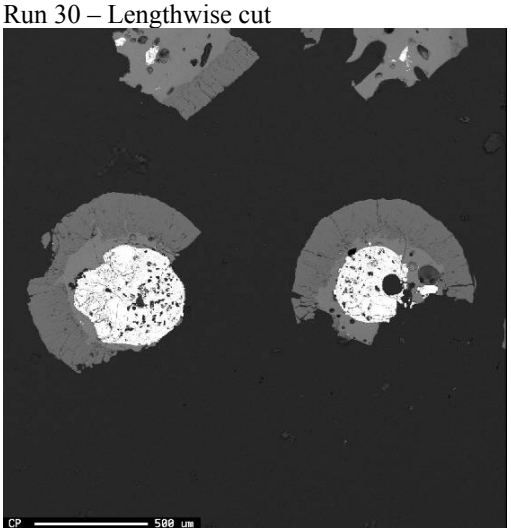

Run 30 – Cross sections

References

Ballhaus, C., Tredoux, M. and Spath, A. (2001). "Phase relations in the Fe-Ni-Cu-PGE-S system at magmatic temperature and application to massive sulphide ores of the Sudbury Igneous Complex." Journal of Petrology **42**(10): 1911-1926.

Barlow, A. E. (1904). "Origin, geological relations and composition of the nickel and copper deposits of the Sudbury mining district, Ontario." Geological Survey of Canada, Annual Report **14**(for 1901): 1-236 (No. 873).

Barnes, S. J., Cox, R. A. and Zientek, M. L. (2006). "Platinum-group element, gold, silver and base metal distribution in compositionally zoned sulfide droplets from the Medvezky Creek Mine, Noril'sk, Russia." Contributions to Mineralogy and Petrology **152**(2): 187-200.

Blundy, J. and Cashman, K. (2001). "Ascent-driven crystallization of dacite magmas at Mount St Helens, 1980-1986." Contributions to Mineralogy and Petrology **140**(6): 631-650.

Blundy, J., Cashman, K. and Humphreys, M. (2006). "Magma heating by decompression-driven crystallization beneath andesite volcanoes." Nature **443**(7107): 76-80.

Brenan, J. M. (2002). "Re-Os fractionation in magmatic sulfide melt by monosulfide solid solution." Earth and Planetary Science Letters **199**(3-4): 257-268.

Buck, W. K. (1968). "Nickel, Canada and the world." Department of Energy, Mines and Resources, Canada, Mineral Resources Division, Mineral Report. **16**.

Calvache, M. L. and Williams, S. N. (1997). "Emplacement and petrological evolution of the andesitic dome of Galeras volcano, 1990-1992." Journal of Volcanology and Geothermal Research **77**(1-4): 57-69.

Candela, P. A. and Bouton, S. L. (1990). "The Influence of Oxygen Fugacity on Tungsten and Molybdenum Partitioning between Silicate Melts and Ilmenite." Economic Geology **85**(3): 633-640.

Candela, P. A. and Holland, H. D. (1984). "The Partitioning of Copper and Molybdenum between Silicate Melts and Aqueous Fluids." Geochimica et Cosmochimica Acta **48**(2): 373-380.

Candela, P. A. and Holland, H. D. (1986). "A Mass-Transfer Model for Copper and Molybdenum in Magmatic Hydrothermal Systems - the Origin of Porphyry-

Type Ore-Deposits." Economic Geology and the Bulletin of the Society of Economic Geologists **81**(1): 1-19.

Candela, P. A. and Piccoli, P. M. (1995). Model ore-metal partitioning from melts into vapor and vapor/melt mixtures, Mineralogical Association of Canada.

DeBari, S. M. and Sleep, N. H. (1991). "High-Mg, Low-Al Bulk Composition of the Talkeetna Island-Arc, Alaska - Implications for Primary Magmas and the Nature of Arc Crust." Geological Society of America Bulletin **103**(1): 37-47.

Englander, L. (2005). An Experimental Study of Silver Partitioning in Sulfide-Oxide-Melt Systems at 800^{o}C. Geology Department. College Park, University of Maryland. M.S. Thesis**:** 134.

Fleet, M. E., Chryssoulis, S. L., Stone, W. E. and Weisener, C. G. (1993). "Partitioning of Platinum-Group Elements and Au in the Fe-Ni-Cu-S System - Experiments on the Fractional Crystallization of Sulfide Melt." Contributions to Mineralogy and Petrology **115**(1): 36-44.

Frank, M. R., Candela, P. A., Piccoli, P. M. and Glascock, M. D. (2002). "Gold solubility, speciation, and partitioning as a function of HCl in the brine-silicate melt-metallic gold system at 800 degrees C and 100 MPa." Geochimica et Cosmochimica Acta **66**(21): 3719-3732.

Goldstein, J. I., Newbury, D. E., Echlin, P., Joy, D. C., Romig, A. D., Lyman, C. E., Fiori, C. and Lifshin, E. (1992). Scanning Electron Microscopy and X-Ray Microanalysis. New York, Plenum Press.

Greene, A. R., DeBari, S. M., Kelemen, P. B., Blusztajn, J. and Clift, P. D. (2006). "A detailed geochemical study of island arc crust: the Talkeetna Arc section, south-central Alaska." Journal of Petrology **47**(6): 1051-1093.

Heming, R. F. and Carmichael, I. S. E. (1973). "High-Temperature Pumice Flows from Rabaul Caldera-Papua, New Guinea." Contributions to Mineralogy and Petrology **38**(1): 1-20.

Hildreth, W. and Wilson, C. J. N. (2007). "Compositional zoning of the Bishop Tuff." Journal of Petrology **48**(5): 951-999.

Hildreth, E. W. (1977). The magma chamber of the Bishop Tuff: gradients in temperature, pressure and composition, University of California, Berkeley. Ph.D. Thesis**:** 328.

Hilty, D. C. and Crafts, W. (1952). "Liquidus Surface of the Fe-S-O System." Journal of Metals **4**(12): 1307-1312.

Holland, H. D. (1972). "Granites, Solutions, and Base Metal Deposits." Economic Geology and the Bulletin of the Society of Economic Geologists **67**(3): 281-&.

Howard-White, F. B. (1963). Nickel, an historical review. Toronto, Ontario, Longmans Canada.

Imai, A. (1994). "Sulfide Globules Associated with a Felsite Intrusion in the Mount Kinabalu Quartz Monzonite, Sabah, East Malaysia - Sulfide Melt Immiscibility in a Highly Silicic Meat." Economic Geology and the Bulletin of the Society of Economic Geologists **89**(1): 181-185.

Ishihara, S. (1977). "The magnetite-series and ilmenite series granitic rocks." Mining Geology **27**: 293-305.

Ishihara, S. (1998). "Granitoid series and mineralization in the Circum-Pacific Phanerozoic granitic belts." Resource Geology **48**(4): 219-224.

Jugo, P. J., Candela, P. A. and Piccoli, P. M. (1999). "Magmatic sulfides and Au : Cu ratios in porphyry deposits: an experimental study of copper and gold partitioning at 850 degrees C, 100 MPa in a haplogranitic melt pyrrhotite intermediate solid solution gold metal assemblage, at gas saturation." Lithos **46**(3): 573-589.

Kress, V. (1997). "Thermochemistry of sulfide liquids .1. The system O-S-Fe at 1 bar." Contributions to Mineralogy and Petrology **127**(1-2): 176-186.

Kress, V. (2000). "Thermochemistry of sulfide liquids. II. Associated solution model for sulfide liquids in the system O-S-Fe." Contributions to Mineralogy and Petrology **139**(3): 316-325.

Larocque, A. C. L., James, A. S. and Siebe, C. (1998). "Metal-residence sites in lavas and tuffs from Volcan Popocatepetl, Mexico: implications for metal mobility in the environment." Environmental-Geology **33**(2/3): 197-208.

Larocque, A. C. L., Stimac, J. A., Keith, J. D. and Huminicki, M. A. E. (2000). "Evidence for Open-System Behaviour in Immiscible Fe-S-O Liquids in Silicate Magmas: Implications for Contributions of Metals and Sulfer to Ore-Forming Fluids." The Canadian Mineralogist **38**: 1233-1249.

Li, C. and Barnes, S. J. (1996). "Partitioning of platinum-group elements and Au in the Fe-Ni-Cu-S system: Experiments on the fractional crystallization of sulfide melt - A discussion." Contributions to Mineralogy and Petrology **123**(4): 435-437.

Li, C., Naldrett, A. J., Coats, C. J. A. and Johannessen, P. (1992). "Platinum, Palladium, Gold, and Copper-Rich Stringers at the Strathcona Mine, Sudbury - Their Enrichment by Fractionation of a Sulfide Liquid." Economic Geology and the Bulletin of the Society of Economic Geologists **87**(6): 1584-1598.

Luhr, J. F. (1990). "Experimental Phase-Relations of Water-Saturated and Sulfur-Saturated Arc Magmas and the 1982 Eruptions of El-Chichon Volcano." Journal of Petrology **31**(5): 1071-1114.

Luhr, J. F. (1992). "Slab-Derived Fluids and Partial Melting in Subduction Zones - Insights from 2 Contrasting Mexican Volcanos (Colima and Ceboruco)." Journal of Volcanology and Geothermal Research **54**(1-2): 1-18.

Luhr, J. F., Carmichael, I. S. E. and Varekamp, J. C. (1984). "The 1982 Eruptions of El-Chichon Volcano, Chiapas, Mexico - Mineralogy and Petrology of the Anhydrite-Bearing Pumices." Journal of Volcanology and Geothermal Research **23**(1-2): 69-108.

Lynton, S. J., Candela, P. A. and Piccoli, P. M. (1993). "An Experimental-Study of the Partitioning of Copper between Pyrrhotite and a High-Silica Rhyolitic Melt." Economic Geology and the Bulletin of the Society of Economic Geologists **88**(4): 901-915.

MacLean, W. H. (1969). "Liquidus Phase Relations in the FeS-FeO-Fe_3O_4-SiO_2 System, and their Application in Geology." Economic Geology and the Bulletin of the Society of Economic Geologists **64**: 865-884.

Metrich, N. and Clocchiatti, R. (1996). "Sulfur abundance and its speciation in oxidized alkaline melts." Geochimica et Cosmochimica Acta **60**(21): 4151-4160.

Mungall, J. E. (2007). "Crystallization of magmatic sulfides: an empirical model and application to Sudbury ores." Geochimica et Cosmochimica Acta **71**: 2809-2819.

Mungall, J. E., Andrews, D. R. A., Cabri, L. J., Sylvester, P. J. and Tubrett, M. (2005). "Partitioning of Cu, Ni, An, and platinum-group elements between monosulfide solid solution and sulfide melt under controlled oxygen and sulfur fugacities." Geochimica Et Cosmochimica Acta **69**(17): 4349-4360.

Naldrett, A. J. (1969). "A Portion of the System Fe-S-O between 900 and 1080^{o}C and its Application to Sulfide Ore Magmas." Journal of Petrology **10**(Part 2): 171-201.

Naldrett, A. J. (2005). "A history of our understanding of magmatic Ni-Cu sulfide deposits." Canadian Mineralogist **43**: 2069-2098.

Naldrett, A. J. and Kullerud, G. (1967). "A Study of Strathcona Mine and Its Bearing on Origin of Nickel-Copper Ores of Sudbury District Ontario." Journal of Petrology **8**(3): 453-&.

Naldrett, A. J. and Richardson, S. W. (1967). "Effect of water on the melting of pyrrhotite-magnetite assemblages." Yearbook Carnegie Institution Washington. **66**(429-31).

Peregoedova, A., Barnes, S. J. and Baker, D. R. (2006). "An experimental study of mass transfer of platinum-group elements, gold, nickel and copper in sulfur-dominated vapor at magmatic temperatures." Chemical Geology **235**(1-2): 59-75.

Prichard, H. M., Hutchinson, D. and Fisher, P. C. (2004). "Petrology and crystallization history of multiphase sulfide droplets in a Mafic Dike from Uruguay: Implications for the origin of Cu-Ni-PGE sulfide deposits." Economic Geology and the Bulletin of the Society of Economic Geologists **99**(2): 365-376.

Reubi, O., Nicholls, I. A. and Kamenetsky, V. S. (2002). "Early mixing and mingling in the evolution of basaltic magmas: Evidence from phenocryst assemblages, Slamet volcano, Java, Indonesia." Journal of Volcanology and Geothermal Research **119**: 255-274.

Richards, J. P. (2003). "Tectono-magmatic precursors for porphyry Cu-(Mo-Au) deposit formation." Economic Geology and the Bulletin of the Society of Economic Geologists **98**(8): 1515-1533.

Richards, J. P., Boyce, A. J. and Pringle, M. S. (2001). "Geologic evolution of the Escondida area, northern Chile: A model for spatial and temporal localization of porphyry Cu mineralization." Economic Geology and the Bulletin of the Society of Economic Geologists **96**(2): 271-305.

Ripley, E. M., Brophy, J. G. and Li, C. S. (2002). "Copper solubility in a basaltic melt and sulfide liquid/silicate melt partition coefficients of Cu and Fe." Geochimica et Cosmochimica Acta **66**(15): 2791-2800.

Rosenqvist, T. and Hynne, P. H. (1953). "On the reaction between iron sulfide and sulfur dioxide." Tidsskrift For Kjemi Bergvesenog Metallurgi **9**: 196-200.

Rowins, S. M. (2000). "Reduced porphyry copper-gold deposits: A new variation on an old theme." Geology **28**(6): 491-494.

Rutherford, M. J. and Devine, J. D. (1991). "Pre-eruption conditions and volatiles in the 1991 Pinatubo magma." EOS Transactions of the American Geophysical Union **72**(44): 62.

Rye, R. O., Luhr, J. F. and Wasserman, M. D. (1984). "Sulfur and Oxygen Isotopic Systematics of the 1982 Eruptions of El-Chichon Volcano, Chiapas, Mexico." Journal of Volcanology and Geothermal Research **23**(1-2): 109-123.

Sasaki, A. and Ishihara, S. (1979). "Sulfur Isotopic Composition of the Magnetite-Series and Ilmenite-Series Granitoids in Japan." Contributions to Mineralogy and Petrology **68**(2): 107-115.

Simon, A. C., Frank, M. R., Pettke, T., Candela, P. A., Piccoli, P. M. and Heinrich, C. A. (2005). "Gold partitioning in melt-vapor-brine systems." Geochimica et Cosmochimica Acta **69**(13): 3321-3335.

Simon, A. C., Pettke, T., Candela, P. A., Piccoli, P. M. and Heinrich, C. A. (2003). "Experimental determination of Au solubility in rhyolite melt and magnetite: Constraints on magmatic Au budgets." American Mineralogist **88**(11-12): 1644-1651.

Simon, A. C., Pettke, T., Candela, P. A., Piccoli, P. M. and Heinrich, C. A. (2007). "The partitioning behavior of As and Au in S-free and S-bearing magmatic assemblages." Geochimica Et Cosmochimica Acta **71**(7): 1764-1782.

Stavast, W. J. A., Keith, J. D., Christiansen, E. H., Dorais, M. J., Tingey, D., Larocque, A. and Evans, N. (2006). "The fate of magmatic sulfides during intrusion or eruption, Bingham and Tintic districts, Utah." Economic Geology and the Bulletin of the Society of Economic Geologists **101**(2): 329-345.

Stimac, J. and Hickmott, D. (1994). "Trace-element partition coefficients for ilmenite, orthopyroxene and pyrrhotite in rhyolite determined by micro-PIXE analysis." Chemical Geology **117**: 313-330.

Stimac, J. and Hickmott, D. (1996). Ore Metal Partitioning in Intermdeiate-to-Silicic Magmas: PIXE Results on Natural Mineral/Melt Assemblages. Second Giant Ore Deposits Workshop, Kingston, Ontario, Canada.

Stuller, B. C. (2001). The partioning behavior of manganese, cobalt, nickel, zinc, molybdenum, tungsten and gold between pyrrhotite and a rhyolitic melt. Geology. College Park, University of Maryland. M.S. Theisis.

Sun, S.-s. and McDonough, W. F. (1989). "Chemical and isotopic systematics of oceanic basalts: Implications for mantle composition and processes." Geological Society of London Special Publication **42**: 313-345.

Toulmin, P. and Barton, P. B. (1964). "The Electrum-Tarnish Method for the Determination of the Fugacity of Sulfur in Laboratory Sulfide Systems." Geochimica et Cosmochimica Acta **28**(MAY): 619-640.

Ueda, A. and Itaya, T. (1981). "Microphenocrystic pyrrhotite from dacite rocks of Satsuma-Iwojima, southwest Kyushu, Japan and the solubility of sulfur in dacite magma." Contributions to Mineralogy and Petrology **78**(1): 21-26.

Vogel, R. and Fulling, W. (1948). "Das System Eisen-Eisensulfid (FeS)-Wustit (FeO)." Festschriftan J. Arvid Hedvall: 597-610.

Warshaw, C. M. and Smith, R. L. (1988). "Proxenes and Fayalites in the Bandelier Tuff, New-Mexico - Temperatures and Comparison with Other Rhyolites." American Mineralogist **73**(9-10): 1025-1037.

Watson, E. B. (1994). "Diffusion in volatile-bearing magmas." Reviews in Mineralogy **30**: 371-411.

Whitney, J. A. (1984). "Fugacities of Sulfurous Gases in Pyrrhotite-Bearing Silicic Magmas." American Mineralogist **69**(1-2): 69-78.

Williams, T. J., Candela, P. A. and Piccoli, P. M. (1995). "The Partitioning of Copper between Silicate Melts and 2-Phase Aqueous Fluids - an Experimental Investigation at 1-kbar, 800^{o}C and 0.5-kbar, 850^{o}C." Contributions to Mineralogy and Petrology **121**(4): 388-399.

Witter, J. B., Kress, V. C. and Newhall, C. G. (2005). "Volcan Popocatepetl, Mexico. Petrology, magma mixing, and immediate sources of volatiles for the 1994 - Present eruption." Journal of Petrology **46**(11): 2337-2366.

Yang, X. M., Lentz, D. R. and Sylvester, P. J. (2006). "Gold contents of sulfide minerals in granitoids from southwestern New Brunswick, Canada." Mineralium Deposita **41**(4): 369-386.